**The Dissertation Committee for Jungdae Kim
certifies that this is the approved version of the following dissertation:**

Low Temperature Scanning Tunneling Microscope Study of Low-dimensional Superconductivity on Metallic Nanostructures

Committee:

Chih-Kang Shih, Supervisor

Alex de Lozanne

John Markert

Zhen Yao

Li Shi

Low Temperature Scanning Tunneling Microscope Study of Low-dimensional Superconductivity on Metallic Nanostructures

by

Jungdae Kim, B.S.; M.S.Phy.

Dissertation

Presented to the Faculty of the Graduate School of

The University of Texas at Austin

in Partial Fulfillment

of the Requirements

for the Degree of

Doctor of Philosophy

The University of Texas at Austin

August 2010

To my parents Minho Kim and Sogun Jung,

To my wife Hyunjung Kim, and

To my daughter Clara Kim

Acknowledgements

First of all, I would like to express the deepest appreciation to my supervisor, Dr. Shih. I would not be able to reach here without his encouragement, guidance, and support from the initial to the final level. With his enthusiasm, his inspiration, and his great efforts to pursue real physics, he helped to make STM experiments fun for me. I'm definitely going to miss his face with eyes full of curiosity/excitement and saying "Did you get it?" I would like to show my gratitude to all my committee members for supervising me. I would like to thank the many people who have taught me physics; especially, my master adviser prof. Taewon Noh, prof. Jonggul Yoon, and my undergraduate adviser prof. Seyoung Jeong.

I wish to thank to all my former and current lab mates for their helps in a number of ways: Dr. Daejin Eom, Dr. Junho Bae, Dr. Niraj Kulkarni, Dr. Andreas Müller, Dr. Pablo Bianucci, Dr. Ned Flagg, Dr. Alex Khajetoorians, Dr. Sebastien Founta, Dr. Sen Yang, Jisun Kim, Hyoundo Nam, Miri Choi, and special thanks to Charlotte Sanders (you're great!), John Robertson, Chris Mann for editing my dissertation. I am really grateful to Dr. Shengyong Qin for helping me tremendously to make our STM up and running. I would not be able to finish this dissertation without his help. I would like to thank all of those in the machine, cryogenic shop, and physics storeroom who supported me in any respect during the completion of the project. I can't miss mentioning my friends in Austin: Jusang and Youngran (needless to say they are just like my family), Jaekwang and Chanjoo (their warm-hearts will be always remembered), Yongsup Ihn,

Woosuk Bang, and Insun Jo (we shared so many good memories, and I believe in their abilities to make a lot of accomplishments).

Lastly, and most importantly, I wish to thank my parents who always believe in me. The way they have been living their life is the most precious lesson I ever had. I would like to say that with all my heart I love my beautiful, thoughtful wife Hyunjung and my daughter Clara.

I dedicate this dissertation to my parents and wife.

Jungdae Kim

The University of Texas at Austin

July 2010

Low Temperature Scanning Tunneling Microscope Study of Low-dimensional Superconductivity on Metallic Nanostructures

Publication No._____

Jungdae Kim, Ph.D.

The University of Texas at Austin, 2010

Supervisor: Chih-Kang Shih

Superconductivity is a remarkable quantum phenomenon in which a macroscopic number of electrons form a condensate of Cooper pairs that can be described by a single quantum wave function.   According to the celebrated Bardeen-Cooper-Schrieffer (BCS) theory of superconductivity, there is a minimum length scale (the coherence length, ξ) below which the condensate has a rigid quantum phase.   The fate of superconductivity in a system with spatial dimensions smaller than ξ has been the subject of intense interest for decades and recent studies of superconductivity in ultra-thin epitaxial metal films have revealed some surprising behaviors in light of BCS theory.   Notably, it was found that superconductivity remains robust in thin lead films with thicknesses orders of magnitude smaller than the coherence length (*i.e.* in the extreme two dimensional limit). Such studies raise the critical question: what happens to superconductivity as all dimensions are reduced toward the zero dimensional limit?   By controlling the lateral size of ultra thin 2D islands, we systematically address this fundamental question with a detailed scanning tunneling microscopy/spectroscopy study.   We show that as the lateral

dimension is reduced, the strength of the superconducting order parameter is also reduced, at first slowly for dimensions larger than the bulk coherence length, and then dramatically at a critical length scale of ~ 40nm.   We find this length scale corresponds to the lateral decay length of the order parameter in an island containing regions of different heights and different superconducting strength.   Overall, our results suggest that fluctuation corrections to the BCS theory are important in our samples and may need to be systematically addressed by theory.

Table of Contents

List of Figures

Chapter 1:   A Scanning Tunneling Microscope - Background

The scanning tunneling microscope (STM) has made a tremendous impact on various fields such as material science, semiconductor physics, superconductivity, and surface chemistry.   Its invention by Gerd Binning and Heinrich Rohrer (at IBM Zürich) [1] provided the first three-dimensional real space images of surfaces at atomic resolution which are capable of representing surface topography, electronic structure, and other local properties.   In this chapter, a general description of the STM will be given as a background.

1.1 INTRODUCTION

A tunneling current can occur between two metallic electrodes with an applied bias when they are very close each other.   In the STM configuration, the two electrodes are a metallic tip and sample.   STM measurement is based on detecting the tunneling current between the two.   A simple schematic showing operation of STM is presented in figure 1.1.
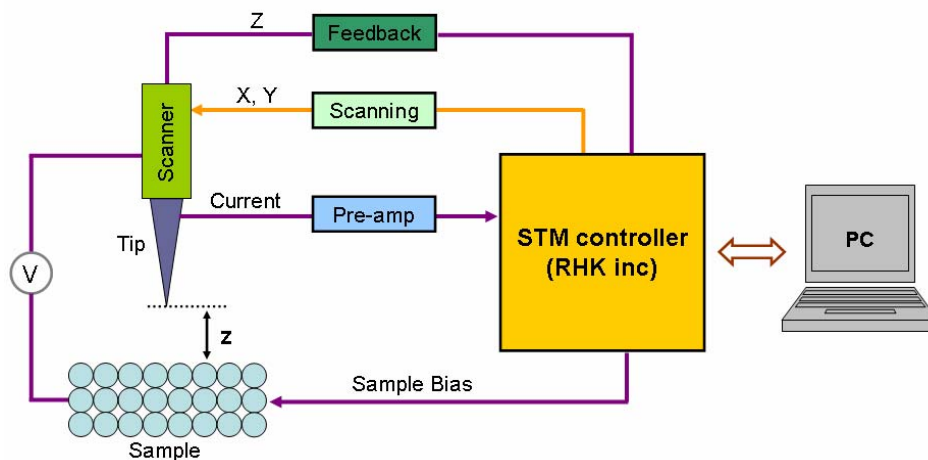
Figure 1.1: A schematic diagram of the scanning tunneling microscope

A metallic tip (usually W or PtIr) is mounted on a piezo scanner which can move with atomic precision along the x, y, and z directions when a controlled bias voltage is applied. The STM tip is brought to within a few angstroms of the sample surface, until a feedback loop detects the required amount of tunneling current between the tip and sample. Once this so-called "coarse approach" is done, the tip is ready to move across the sample surface while maintaining either a constant current or a constant height. Then, depending on the operation mode (see next section), either tip height (z) or tunneling current as a function of tip location will be recorded in real time, and an STM image can be generated.

1.2 TWO OPERATION MODES OF THE SCANNING TUNNELING MICROSCOPE

When the tip scans the sample surface along the x-y direction, surface topography and the local density of states (LDOS) of the sample dramatically influence the tunneling current. In STM operation, there are two modes, called "constant height mode" and "constant current mode", as shown in figure 1.2.
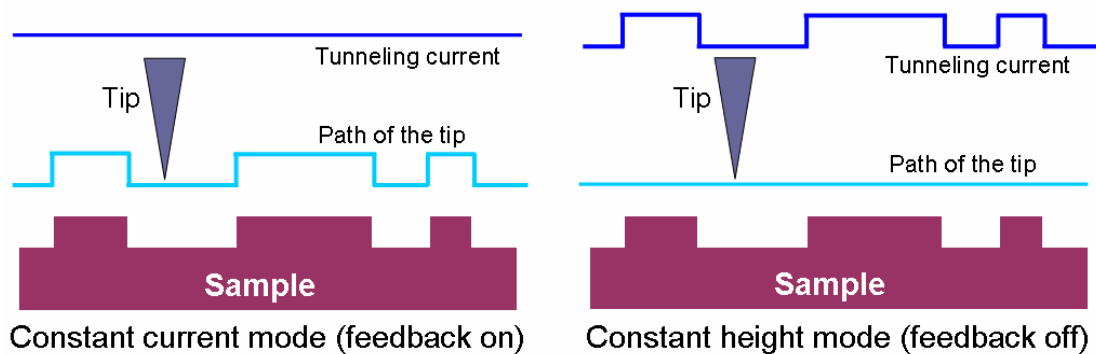
Figure 1.2: An illustration of two STM operation modes: constant current mode and constant height mode.

In constant current mode, a feedback loop maintains the tunneling current at a constant value by adjusting the tip height (z).   Then the path in z directly reflects the combined information of surface topography and LDOS, and will be recorded with tip x-y location in real time.   In the case of constant height mode, on the other hand, the feedback loop is disabled to keep z at a fixed height during scanning.   The computer records the changes of tunneling current with tip coordinates which reflects the same surface information as constant current mode.   Faster scanning is possible in constant height mode than in constant current mode.   This is because feedback needs some time to adjust the height of the tip in constant current mode.   However, unless the surface to be studied is well-known and atomically flat, however, constant current mode is more commonly used to avoid tip crashing.

1.3 A SIMPLE MODEL OF TUNNELING
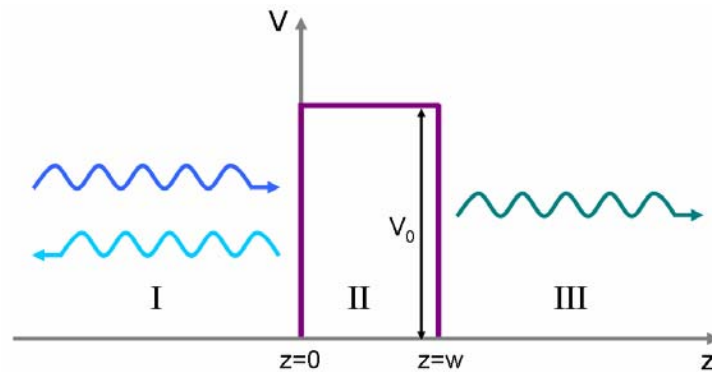
Figure 1.3: A simple one dimensional potential barrier.

In this section, a simple model of a one dimensional tunneling junction will be discussed.   First, let us look at the simple quantum mechanics problem of a one dimensional potential barrier, illustrated in figure 1.3.   We assume that an electron with

3

energy E is moving from the left to right side of the barrier and its energy is lower than the potential barrier height V_0. For regions I and III, the electron state can be described by a wave function $\Psi(z)$ obtained by solving Schrödinger's equation,

$$-\frac{\hbar^2}{2m}\frac{\partial\Psi(z)}{\partial z^2} = E\Psi(z) \tag{1.1}$$

where $\hbar$ is Planck's constant, z is the position, and m is the electron mass. Then the electron wave function can be expressed as a traveling wave equation,

$$\Psi_I(z) = Ae^{+ikz} + Be^{-ikz}$$
$$\Psi_{II}(z) = ce^{+ikz} \quad , \quad k = \frac{\sqrt{2mE}}{\hbar} \quad \text{(wave vector).} \tag{1.2}$$

The probability current density (j) of each region can be written as

$$j_I = \frac{\hbar k}{m}(|A|^2 - |B|^2), \quad j_{II} = \frac{\hbar k}{m}|C|^2 . \tag{1.3}$$

For region II (inside the barrier), which is a classically forbidden area, an electron state has the form of decaying wave,

$$-\frac{\hbar^2}{2m}\frac{\partial\Psi(z)}{\partial z^2} + V_0\Psi(z) = E\Psi(z) \tag{1.4}$$

$$\Psi_{II}(z) = D_1 e^{-\kappa z} + D_2 e^{+\kappa z}, \quad \kappa = \frac{\sqrt{2m(V_0 - E)}}{\hbar} \quad \text{(decay constant).} \tag{1.5}$$

Those coefficients A, B, and C can be found by using the boundary conditions; i.e., the wave function and its derivative should be continuous everywhere.

$$\Psi_I(0) = \Psi_{II}(0), \text{ and } \frac{\partial}{\partial z}\Psi_I(0) = \frac{\partial}{\partial z}\Psi_{II}(0) \quad \text{at } z = 0$$

$$\Psi_{II}(w) = \Psi_{III}(w), \text{ and } \frac{\partial}{\partial z}\Psi_{II}(w) = \frac{\partial}{\partial z}\Psi_{III}(w) \quad \text{at } z = w \tag{1.6}$$

4

The transmission and reflection coefficients can be calculated from the coefficients found in the boundary conditions,

$$t = \left|\frac{C}{A}\right|^2 = \frac{4\kappa^2 k^2}{(\kappa^2 - k^2)\sinh^2 \kappa w + 4\kappa^2 k^2 \cosh^2 \kappa w} \quad \text{(Transmission coefficient)}$$

$$r = \left|\frac{B}{A}\right|^2 = \frac{(\kappa^2 + k^2)\sinh^2 \kappa w}{(\kappa^2 - k^2)\sinh^2 \kappa w + 4\kappa^2 k^2 \cosh^2 \kappa w} \quad \text{(Reflection coefficient)} \qquad (1.7)$$

Now we are ready to apply this simple model to an STM configuration which is basically a metal-vacuum-metal junction. As presented in figure 1.4, the work function (ϕ) is defined as the minimum amount of energy required to bring an electron from the Fermi energy level (E_F) of a metal to the vacuum level. For our purpose, it is convenient to assume that the tip and sample have the same work function, and also that the Fermi energy of the two electrodes (tip and sample) is at the same level. Therefore, there will be no net tunneling current without applying a bias at the junction.
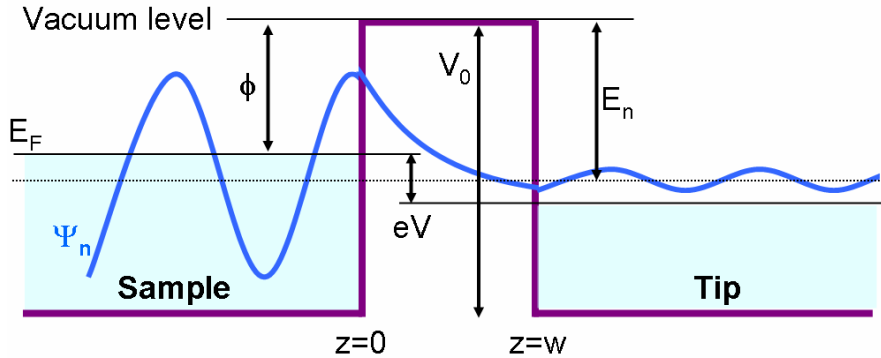
Figure 1.4: A simple model of one dimensional tunneling junction of STM.

The tunneling current flows between the tip and sample with a given by bias voltage eV. An electron state Ψ_n with energy E_n (E_F - eV < E_n < E_F) in the sample has some probability of tunneling into the tip. By assuming eV << ϕ, the energy levels of

all electrons that can be expected to tunnel will be located very close to the Fermi level E_F (i.e. $E_n \sim \phi$) [2].   Since we have already solved a basic barrier problem above, we know that the electron state is decaying, as in eq. (1.5), inside the barrier (see the schematic of inside the barrier, figure 1.4).   Then the probability of finding an electron at z=w is proportional to the wave function squared,

$$p \propto \left| \Psi_n(0) \right|^2 e^{-2\kappa z}, \quad \kappa = \frac{\sqrt{2m\phi}}{\hbar}. \tag{1.8}$$

Since the tunneling current depends on the number of sample electron states between E_F - eV and E_F, it can be expressed by summing all allowed states in a given energy regime [2],

$$I \propto \sum_{E_n = E_F - eV}^{E_F} \left| \Psi_n(0) \right|^2 e^{-2\kappa w} \tag{1.9}$$

Similarly, we can define a sample's local density of states (LDOS) near energy E in an interval ε as

$$\rho_s(z, E) = \frac{1}{\varepsilon} \sum_{E-\varepsilon}^{E} \left| \Psi_n(z) \right|^2 \tag{1.10}$$

and this LDOS expression can be incorporated into the expression for the tunneling current (1.9)[2],

$$I \propto V \rho_s(0, E_F) e^{-2\kappa w} \tag{1.11}$$

where $\rho_s(0, E_F)$ is the LDOS near E_F in the sample.   Therefore, The LDOS near E_F can be measured by the tunneling current with an applied bias V, and this characteristic of the tunneling current makes the STM measurement very meaningful.

1.4 THE BARDEEN APPROACH TO TUNNELING THEORY

In the previous section, the basic concept of electron tunneling was explained with a simple barrier model, and we applied this model to a metal-vacuum-metal (MIM)

6

tunneling junction (a simple STM configuration) so that we could understand some important features of the tunneling current of STM. For a more realistic tunneling model, however, solving Schrödinger's equation by using boundary conditions is a quite complicated problem. Furthermore, the simple approach did not consider the rate at which electrons can pass the barrier, and this rate absolutely influences the tunneling current. A better tunneling model is necessary in order to get a more realistic tunneling current.

John Bardeen developed an approach using time dependent perturbation to understand the MIM tunneling junction, and his approach is one of the most extensively used theoretical methods [3]. He separates the MIM junction into two subsystems (i.e. tip and sample in STM configuration), and asserts that the wave functions ψ and χ for each side of the junction can be found by solving simple stationary Schrödinger's equations. The tunneling current occurs when these two wave functions (ψ and χ) overlap between the subsystems, and this overlap determines the amplitude of electron transfer, or the tunneling matrix M. In STM configuration, M can be calculated by a surface integral on a surface between the tip and sample, $z=z_0$,

$$M = \frac{\hbar}{2m} \int_{z=z_0} \left(\chi^* \frac{\partial \psi}{\partial z} - \psi \frac{\partial \chi^*}{\partial z} \right) ds \qquad (1.12)$$

where ψ and χ are the wave functions of the tip and sample [2]. Then Fermi's Golden Rule provides the rate of electron transfer across the barrier,

$$w = \frac{2\pi}{\hbar} |M|^2 \delta(E_\psi - E_\chi) \qquad (1.13)$$

where $\delta(E_\psi - E_\chi)$ restricts the tunneling to occur only between electron levels of the same energy. Summing over all relevant states gives the tunneling current, and the

electrons in both electrodes follow the Fermi distribution, $f(E) = \dfrac{1}{1 + e^{(E-E_F)/k_B T}}$. With

an applied bias V, the tunneling current is

$$I = \frac{4\pi e}{\hbar} \int_{-\infty}^{+\infty} \left[f(E_f - eV + \varepsilon) - f(E_f + \varepsilon) \right] \rho_s(E_f - eV + \varepsilon) \rho_T(E_f + \varepsilon) |M|^2 \, d\varepsilon \qquad (1.14)$$

where ρ_s and ρ_T are the densities of states (DOS) in the sample and tip, respectively.   It

is reasonable to use the Fermi distribution in eq. (1.14) at any finite temperature because

the states near the Fermi energy significantly alter the tunneling current.   If the

temperature is sufficiently low that $k_B T$ is smaller than the energy resolution required in

the experiment, the Fermi distribution function can be replaced by a step function as

shown below [2]:

$$I = \frac{4\pi e}{\hbar} \int_0^{eV} \rho_s(E_f - eV + \varepsilon) \rho_T(E_f + \varepsilon) |M|^2 \, d\varepsilon \qquad (1.15)$$

Eq. (1.15) tells us that the DOS of the sample and tip equally contribute to the tunneling

current.   With a reasonable assumption that for the energy range of interest, the DOS of

metallic tip and tunneling matrix M do not show observable changes, the tunneling

current becomes

$$I \propto \int_0^{eV} \rho_s(E_F - eV + \varepsilon) \, d\varepsilon . \qquad (1.16)$$

Therefore, in scanning tunneling spectroscopy (STS) measurements, the differential

tunneling conductance dI/dV reflects the DOS of the sample as shown in eq. (1.17):

$$\frac{dI}{dV} \propto \rho_s(E_F - eV) . \qquad (1.17)$$

The experimental details and operating principles for various methods of STS will be discussed in chapter 3.

Chapter 2:   Building Up an Ultra High Vacuum Low Temperature Scanning Tunneling Microscope

Thanks to the development of software and electronics in the last few decades along with advanced HUV technology, STM becomes one of the most powerful tools in surface science.   In order to build up an STM system and make it perform as expected, every component of STM needs to serve the others well.   In this chapter, a few key components of an ultra high vacuum low temperature STM (UHV LT-STM) will be briefly described, as well as related technical issues.

2.1 INTRODUCTION

The typical resolution of STM is considered to be 0.1 nm for the lateral dimension and 0.01 nm along the z (tip-sample distance) direction. With this resolution, STM is capable of showing individual atoms on the surface of materials.   However, taking clear atomic images in STM is not always trivial.   To achieve atomic resolution, even for commercial STMs, one will confront technical issues such as external noise from the environment, internal noise due to signal couplings, and vibration isolation.

Although few scanning probe techniques can obtain images with resolution as high as STM, the greatest power of STM might be its capability for scanning tunneling spectroscopy (STS).   Reliable STS became possible only after people had succeeded in incorporating low temperature environments into STM systems.   At low temperature, STM was able to explore many low temperature physical phenomena such as superconductivity, charge density waves, and magnetic orderings.   In addition to the technical concerns inherent in all STM systems, the design and construction of a low temperature STM (LT-STM) requires extra care.

10

2.2 INSTRUMENT DESIGN

Dr. Daejin Eom, a former student of Dr. Shih's laboratory, constructed the prototype LT-STM in our lab. This first generation LT-STM was very carefully designed to achieve maximum thermal contact between STM head and a liquid helium bath, as well as operational convenience and minimum operational cost. So far, many intriguing experiments have been successfully done in this home-built STM. To investigate more challenging projects, however, a few improvements over the original design were necessary:

(1) The sample temperature can go down to ~ 5K under liquid helium cooling in our original system, but this is not low enough to study two-dimensional superconductivity whose transition temperature (T_c) often falls below 5K.

(2) The liquid nitrogen dewar in our original system needs to be refilled every 24 hours (although liquid helium can last more than 30 hours), which limits the time in which data can be taken without disturbance.

(3) Reducing radio (RF) frequency noises is essential to achieve good STS energy resolution.

In order to address points (1) and (2) in our 2nd generation LT-STM, we have improved the design of all thermal shielding, to prevent the STM head from heating up due to the outside radiation; we have also enlarged the liquid capacity of the cryogenic dewar for both liquid helium and liquid nitrogen to last at least 52 hours. For the purpose of (3), I made all signal wires running into the STM head pass through RF filters (sold by Spectrum) with proper grounding.

2.2.1 Pan type STM head

A few different designs of STM head have been developed since the STM was invented in 1981. The Pan type head [4] is one of the most widely used designs, especially in LT-STM, due to unique advantages that will be discussed below. We adopted this famous design into our LT-STM system because it satisfied our demand, very well.
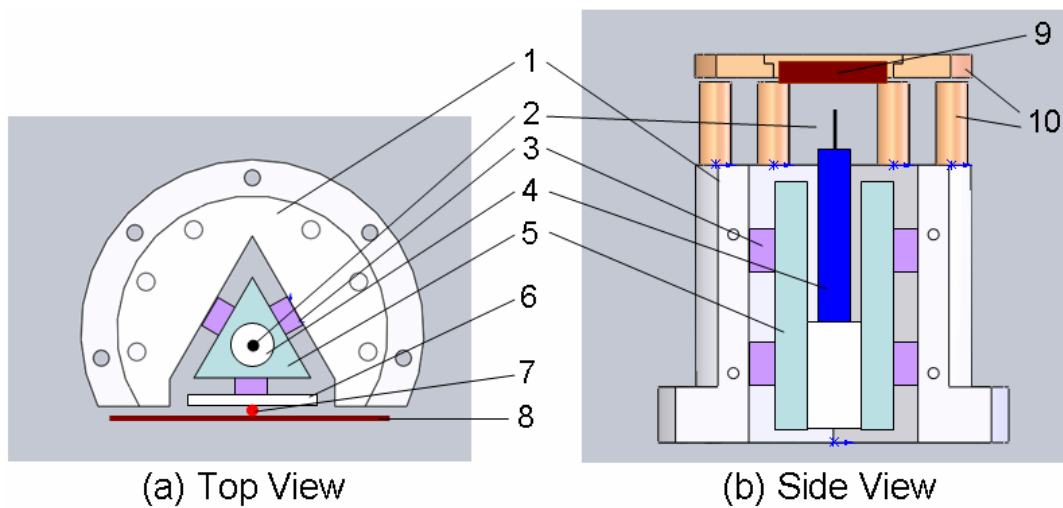
Figure 2.1: Schematic of Pan type STM head: (a) top view and (b) side view. 1. Macor body, 2. STM tip, 3. Shear piezo stacks glued on the macor body, 4. Piezo tube scanner, 5. Sapphire prism which holds the scanner and tip, 6. Stainless steel spring plate, 7. Sapphire (or ruby) ball, 8. Macor plate, 9. Sample, 10. Sample stage

A schematic illustration of the Pan type STM head is shown in figure 2.1. The first thing to which one should pay attention, in making a LT-STM head is choosing proper materials. For the head's main body structure (1), a machineable glass-ceramic called Macor, developed and sold by Corning Incorporated, is used. It is worth mentioning its unique characteristics: (a) Macor has a high resonance frequency, which is essential for STM to reduce vibrational noise; (b) it is a very good UHV compatible insulator with excellent tolerance, and its low thermal expansion (9.3 μm/mK for 300K)

ensures that its shape changes very little under temperature change. (c) although machining Macor requires care, its machineability is an important advantage over other ceramics. The top part of the STM head is the sample stage (10), where a sample is placed. Molybdenum can be used for the sample stage because it has reasonably good thermal conductivity (138 W/mK at 300K, as compared to 81 W/mK for bras or 12.3 W/mK for stainless steel) which is critical to achieve low sample temperature. It also has one of the lowest thermal expansion coefficients (4.8 μm/mK at 300K) among commonly used metals. Matching thermal expansion coefficients of all materials used in LT-STM head is very important to minimize structural stress and thermal drift due to thermal cycles. Six stacks of shear piezos (3) are mounted on the inner wall of the macor body (1), and well polished ceramic shoes are glued on top of those piezo stacks. A sapphire shaft (5) which includes a tube scanner (4) and an STM tip (2) is safely held by the six piezo stacks and this holding (or pressing) force can be precisely controlled by a stainless steel spring plate (6). By inserting a sapphire ball (7) between the spring plate (6) and macor plate (8) one ensures that the friction between the sapphire prism and piezo stacks is evenly distributed, and this is critical for reliable coarse approach. By applying a sequence of high voltage bias pulses with appropriate wave form to the piezo stacks, the sapphire prism can move either upward or downward, depending on the bias polarity.

The Pan type head has several benefits for LT-STM. As shown in figure 2.1, the Macor body, sapphire prism, and sample stage are very connected, so that the whole STM head works as one body with excellent mechanical stability, and without any of springs required in typical STM designs for vibration isolation. In addition, the Pan type design allows us to mount the STM head directly onto the cryogenic bath, which guarantees optimum thermal contact.
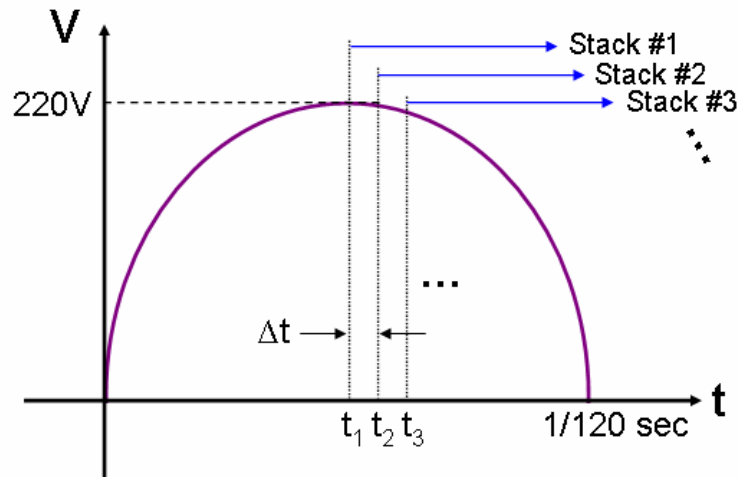
Figure 2.2: An illustration of a sequence of biases applied to the piezo stacks. From standard power outlet 60Hz 110V_{ac}, 60Hz 220V_{ac} power is generated with a step-up transformer. Then it is chopped into six bias signals with time interval Δt and they are sent into each of 6 piezo stacks. In each time interval, only one stack at a time creates shear motion while the other 5 stacks are holding the prism.

Four plates of EBL #4 shear piezo are used for one stack. A sequence of applied high voltage biases to each piezo stack is described in figure 2.2. A given input bias of 60Hz 220V_{ac} is chopped into a sequence of high voltage pulses with time interval Δt ~ 0.1 msec (determined by a time constant in the flip-flop circuit of Dr. Pan's patent document [5]). These chopped signals are sent into the piezo stacks, resulting in shear motion. In each time interval only one stack moves at a time upward or downward, while the other 5 stacks are stationary, holding the sapphire prism (i.e. STM scanner and tip). The prism will not move because the friction from the five stationary stacks is five times as strong as the friction force due to the single moving stack. The applied biases are all in phase each other. Finally, all the shear piezo stacks move simultaneously, so that the friction is strong enough to move the prism by one step. Each step motion is very reliable and reproducible (one step size of our STM head is 200 ~ 250 nm at room

14

temperature) so that it is possible for a STM tip to relocate to a particular spot on a sample without big displacement (see figure 2.3).

Figure 2.3: A photo of Pan-type STM head

2.2.2 Cryostat design
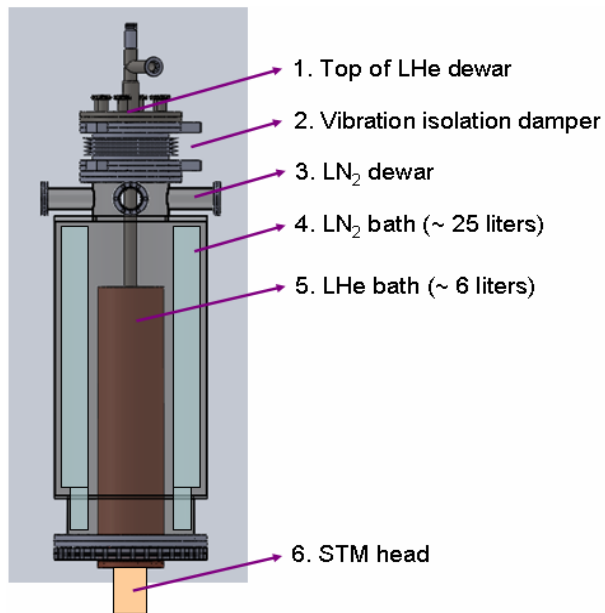
Figure 2.4: A schematic drawing of our home-built LHe and LN$_2$ dewar systems.   Since the STM head is mounted directly on the bottom of the LHe bath, we ensure good thermal contact between STM head and LHe bath.

Regardless of its purpose, there is one common rule in designing a cryostat: one should minimize unwanted thermal leaks which result in the waste of valuable cryogenic liquid and also limit the minimum achievable base temperature. A schematic drawing of our home-built liquid helium (LHe) and liquid nitrogen (LN$_2$) cryostats is shown in figure 2.4. This cryostat system is designed to satisfy the goal of low operating cost and convenient operation. The LHe dewar is placed inside the LN$_2$ dewar so that the surrounding LN$_2$ jacket prevents LHe from heating due to outside radiation. The LHe consumption rate with 4.3K normal operation is less than 3 liters per day. The boiling of LN$_2$ often introduces vibration noises into STM measurement, and so isolating the LN$_2$ dewar from the STM head is one of the main concerns in LT-STM. We put a metal bellow damper (see 2 in figure 2.4) between LHe dewar and LN$_2$ dewar. Even though this is a very simple solution, it turns out to work surprisingly well. The STM head is directly connected to the bottom of the LHe bath, but the Pan-type head is barely affected by LHe boiling due to its great rigidity. In our 2nd generation LT-STM, in fact, we have found that even if we use LN$_2$ for both inner and the outer dewars we can still get beautiful atomic images, as shown figure 2.5.

21nm × 21nm
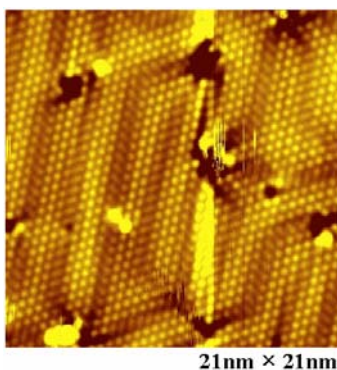
Figure 2.5: An atomic image of Pb-Si $\sqrt{3} \times \sqrt{3}$ taken under LN$_2$ cooling. Our STM head is sufficiently rigid to deliver atomic resolution even with LN$_2$ boiling ($V_{sample} = 0.3$ V and I = 100 pA)

16
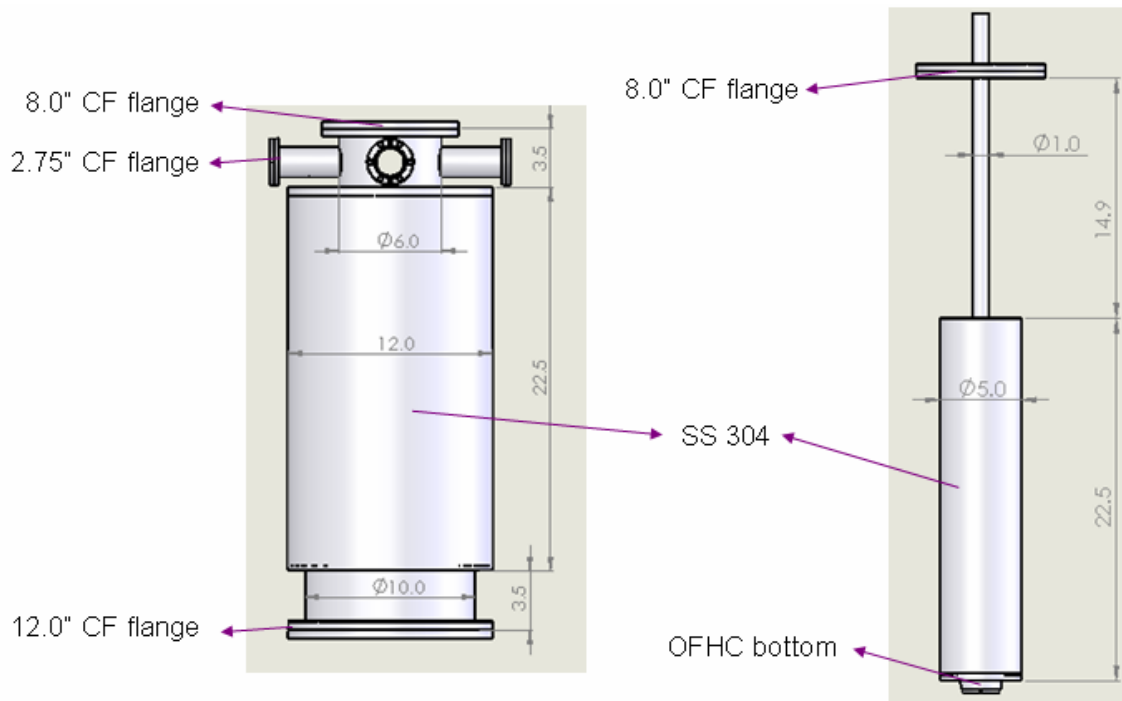
Figure 2.6: Detail drawing of LN$_2$ and LHe dewars

A detailed engineering drawing of our LN$_2$ and LHe dewars is given in figure 2.6. All chamber walls of the LN$_2$ dewar are made of stainless steel (SS) 304 with 1/32 inch wall thickness. For the LHe dewar, a thinner wall (1/64 inch) of SS 304 is used, mainly to make the channel of thermal leak as small as possible. The bottom plate of the LHe bath is made of oxygen-free high conductivity (OFHC) copper for better thermal contact with the STM head.

2.2.3 Radiation shielding

Even if one attaches the STM head directly to the bottom of the LHe bath, it does not guarantee that the sample temperature will cool down to 4.2K. This is inevitable for the sample to be heated up due to external radiation. Therefore, designing proper

radiation shielding is very important in a low temperature system. Our radiation shielding consists of three layers of concentric OFHC copper cans completely surrounding the STM head. The two inner cans are connected directly to the bottom of LHe bath, while the outer one is mounted directly onto the bottom of the LN_2 bath, as illustrated in figure 2.7. Each shielding is designed with a big enough opening that one can access the STM head through a sliding door, so that *in-situ* exchange of tip, and sample is possible when all three shielding doors are fully opened (see the right photo of figure 2.7). The sliding doors can be easily operated by a wobble stick. Moreover, by adjusting the opening of the sliding doors, sample temperature can be controlled. OFHC copper of thickness 1/32 inch or thicker is used for these three layers of shielding, and we are able to reach around 4.3K at the STM sample stage when all of the shielding doors are completely closed.
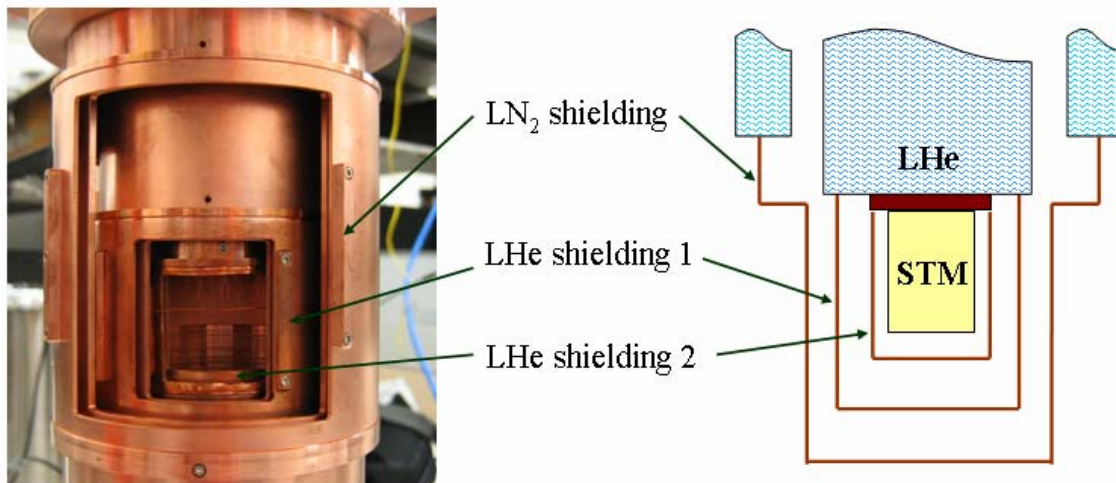
Figure 2.7: A photo and schematic of OFHC radiation shielding. Each shielding has an opening with a sliding door and *in-situ* tip and sample exchange is possible when all of shielding doors are fully opened.

2.2.4 UHV STM chamber

A UHV STM chamber accommodates all necessary components of the whole STM system.   User friendly design of this main chamber is important not only to reduce any chance of unexpected accidents during operation, but also to improve the efficiency of operation.   A typical STM system has a separate sample preparation chamber which is connected to the STM chamber only when a sample is ready for STM study.   This is because preparing a sample must not disturb the operation of the STM or vise versa. The separate chamber can conveniently accommodate various sample preparation and characterization techniques requiring a lot of space, such as molecular beam epitaxy (MBE), X-ray photoelectron spectroscopy (XPS), low-energy electron diffraction (LEED), and reflection high-energy electron diffraction (RHEED).   In some material systems such as metals on semiconductors, however, having an independent chamber for sample preparation is not ideal because of their unique growth properties.   For example, maintaining a low sample temperature ($100 \sim 150K$) is indispensable for preparation of ultra-thin Pb films on Si(111), not only during the growth of Pb, but also during transfer of a sample into STM.   Quick transfer of a prepared sample into the STM head is required to prevent heating and retain the desired sample structures, and this is not an easy task with a separate growth chamber.

We designed the main chamber of our system to address all the issues described above.   As shown in figure 2.8, the main chamber consists of two partitions: (a) the STM section contains LHe/LN$_2$ cryostats including the STM head, a tip-sample carousel, and a wobble stick; and (b) the sample preparation area comprise up to two MBE cells, a sample stage with heater and cold finger, an E-beam cleaning stage for STM tip, and LEED, all in a very compact design.   The cold sample can be transferred from the preparation area to the STM head within 3 minutes after low temperature deposition.   If

19

deposition occurs at 100K, then during transfer the sample temperature goes up to ~ 150K, which is low enough for our purposes.
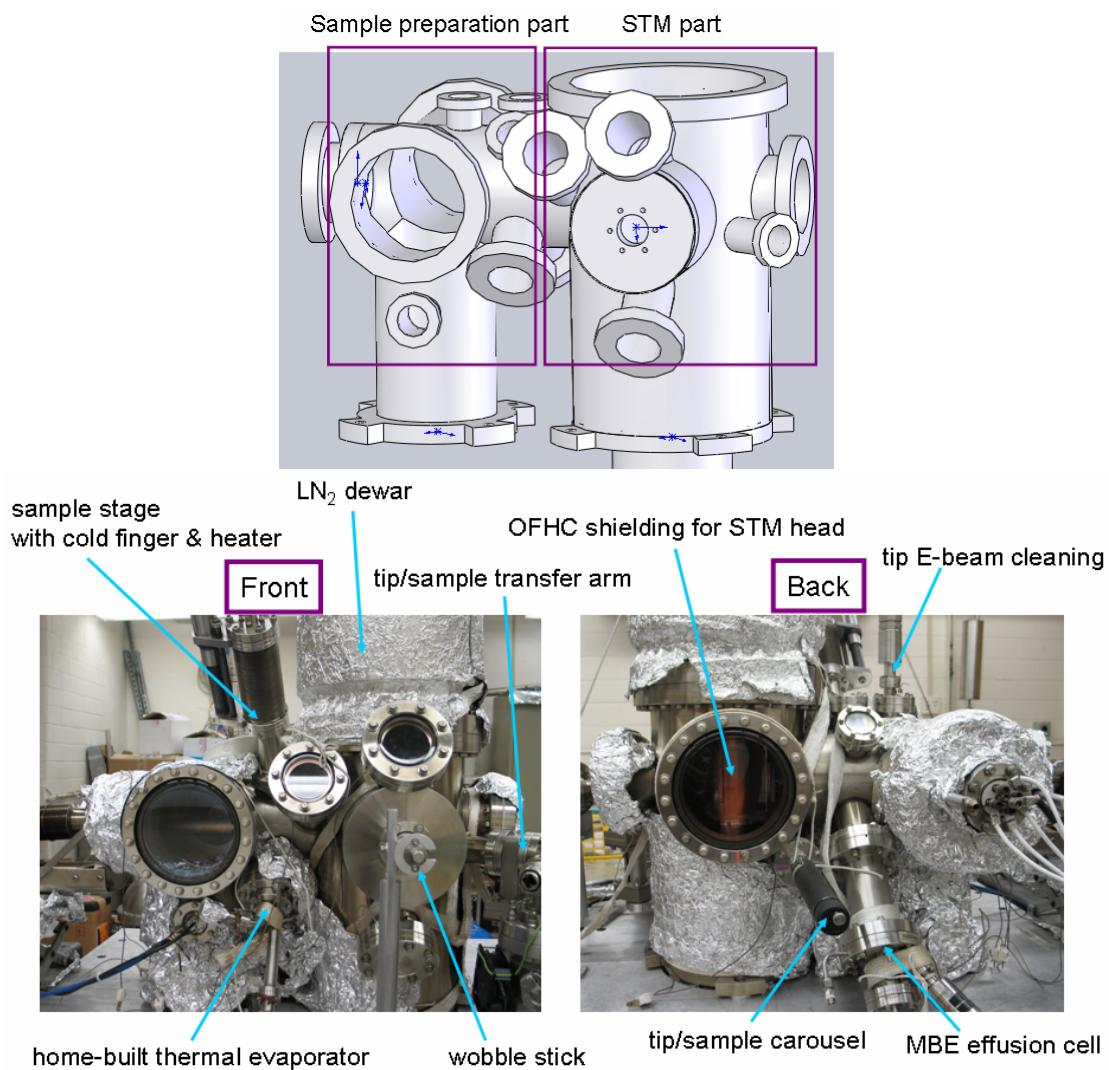
Figure 2.8: UHV main chamber for LT-STM system. Although it is a compact chamber, it can be equipped with various sample preparation instruments.

2.2.5 Radio frequency interference

Radio frequency interference (RFI, also called electromagnetic interference, EMI) is a disturbance that affects STM measurements – especially STS – due to electromagnetic radiation emitted from an external source. The disturbance often degrades significantly the energy resolution of tunneling spectra and it is one of the most common issues in tunneling spectroscopy measurements. However, finding the source of RFI is not a trivial mission because usually it does not show any features in the noise spectrum of tunneling current even if it exists there. Some STM groups have solved the RFI problem by constructing an RF shielded room with built-in RF filtered power outlets. This is the optimum solution to free one's STM experiment from many RF related troubles, but in reality not many groups can afford to have such a kind of environment.

We have spent a lot of time to re-solve this issue. With Prof. Shuheng Pan's advice, we have found a very economic yet effective solution. Figure 2.9(a) shows a home-built RF filter box where low pass filters (sold by Spectrum, Inc) are used. All signal wires running to the STM head should pass through the filter box and its ground should be connected to the most stable point, possibly on the main chamber. To test the RF filter, the superconducting gap of 7ML Pb films is measured with and without RF filtering and the result is dramatic, as shown in figure 2.9(b). The *dI/dV* data with RF filter shows a much deeper and narrower gap than one obtained without an RF filter. It is clear that RF noise affects the tunneling spectra as a broadening factor, resulting in tremendously degradation of the energy resolution.
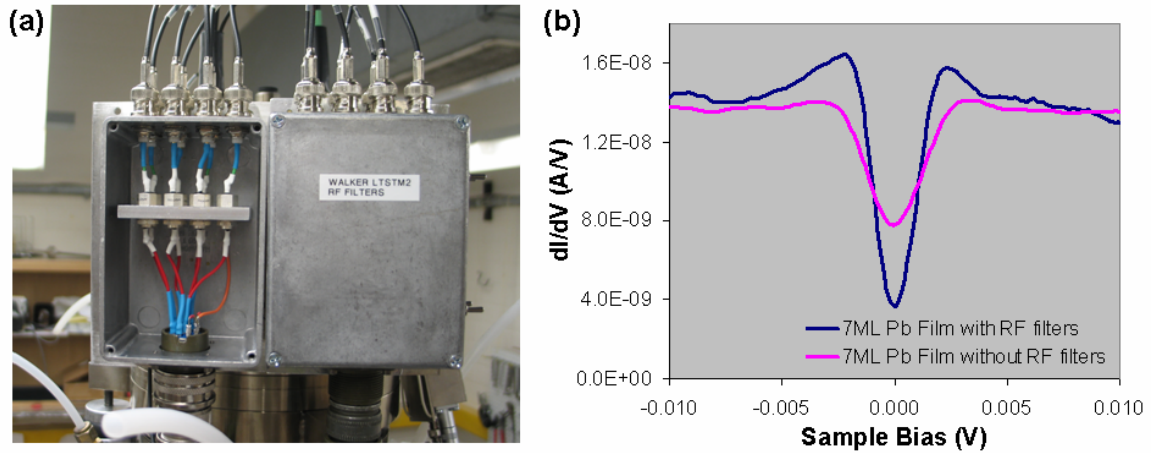
Figure 2.9 (a) A photo of home-built RF filter box.   (b) 7ML Pb superconducting gap with and without RF filters

2.2.6 Combined sample stage with cold finger and heater

As briefly mentioned in section 2.2.4, low temperature growth is a key ingredient in the so-called "quantum growth" of ultra-thin flat films for metal on semiconductor systems.   Metal on semiconductor systems have been widely studied due to their intriguing quantum size effects, ever since the quantum growth behavior was first found by Smith *et al.* [6].   I have designed a combined sample stage with heater and cold finger, specially made to study these material systems.   As presented in figure 2.10, it consists of two stages.   The cooling stage (stage #1) is made mainly of OFHC copper, and is welded to SS tubing.   By filling the tubing with cryogenic liquid, the stage can be quickly cooled (to ~ 100K in 30 min under LN_2 cooling).   The heating stage (stage #2) is designed to flash silicon substrates to remove their native oxide layer, and it is made of molybdenum.   It should be noticed that the two stages are designed to be thermally isolated by ceramic washers, so other parts will not outgas too much during flashing in the heating stage.   Thanks to this two-stage design, the chamber can hold a base pressure below 5×10^{-10} torr during flashing.

22
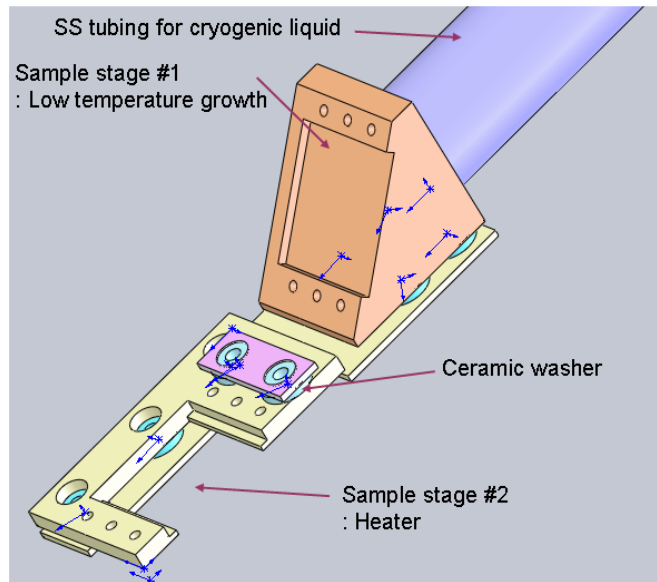
Figure 2.10: A combined sample stage with cold finger and heater.

2.3 OBTAINING TEMPERATURES BELOW 4.2K

One simple way to achieve temperatures below 4.2K is to lower the vapor pressure of LHe over a LHe bath by pumping. It is possible to reach temperatures as low as 0.75K theoretically. Although temperatures in a range of 4.2K ~ 1K are technically achievable when a powerful enough pump is used, temperatures below the λ-point (2.17K) of helium are challenging to obtain. The λ-point is the temperature where the phase transition of helium from normal fluid to superfluid happens. This superfluid can climb quickly through the surface of the LHe bath until it reaches a warmer area and then evaporates, giving additional load to the pump.

The cooling power ($\dot{Q}(T)$) of LHe pumping can be expressed in terms of the molar latent heat ($L(T)$) of vaporization, and the molar evaporation rate ($\dot{n}$ in moles per time).

23

$$\dot{Q}(T) = L(T)\dot{n}\ ;\ L(T) = 96 \text{ J/mol at } 1.2 \sim 4K \text{ for LHe vaporization}$$

On the other hand, reducing the total heat capacity of the system including the sample, cryostat, and LHe is important in order to reach below 4.2K effectively.   It is often the case that the component occupying most of the total heat capacity turns out to be the LHe itself: l liter of LHe at 4.2K has a heat capacity of 400 J/K, which is huge compared with 0.2 J/K for 1 Kg of copper.   Then, roughly 40% of LHe must be evaporated to cool down the remaining LHe from 4.2K to 1.5K.
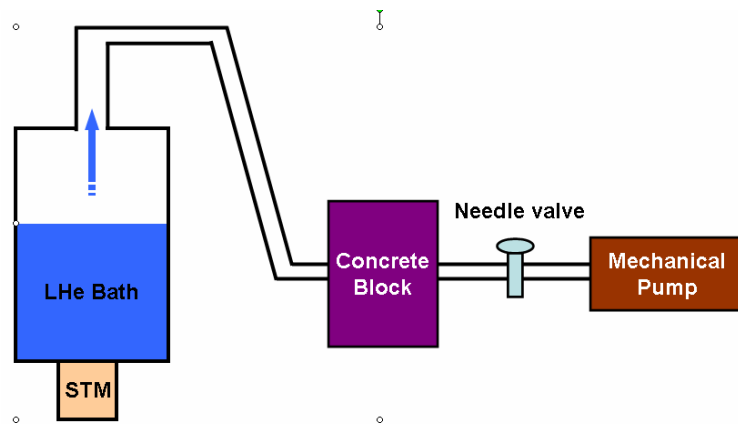
Figure 2.11: A schematic of LHe bath pumping configuration with vibration isolation

For STM measurement, it is also critical to protect the STM system against any vibrational noise caused by pumping, especially when a mechanical pump is used. Figure 2.11 illustrates an easy solution to isolate vibrational noise from an STM system. The pumping line from a LHe dewar passes through a heavy concrete block and then goes to the mechanical pump.   By putting a needle valve between the block and pump, the pumping speed can be manually controlled to obtain desired temperatures.

Chapter 3:   Scanning Tunneling Spectroscopy

3.1 CURRENT VS. BIAS (*I-V*) SPECTROSCOPY

Current vs. Bias (*I-V*) spectroscopy is one of the most commonly used spectroscopies in STM.   In order to measure an *I-V* spectrum, the feedback loop should be disabled to fix the tip-sample distance, and then the tunneling current is recorded with respect to the sweeping sample bias.   The local density of states (LDOS) of a sample can be extracted from the differential conductance (*dI/dV*) spectrum which is obtained either by taking the numerical derivative of an *I-V* spectrum, or by lock-in amplifier techniques (a sort of direct measurement of the derivative of the *I-V* spectrum). Actually, a lock-in amplifier often makes STM spectroscopy even more powerful; mapping LDOS in real space for a given bias can be done simultaneously while taking a topography image.

3.1.1 Theoretical background
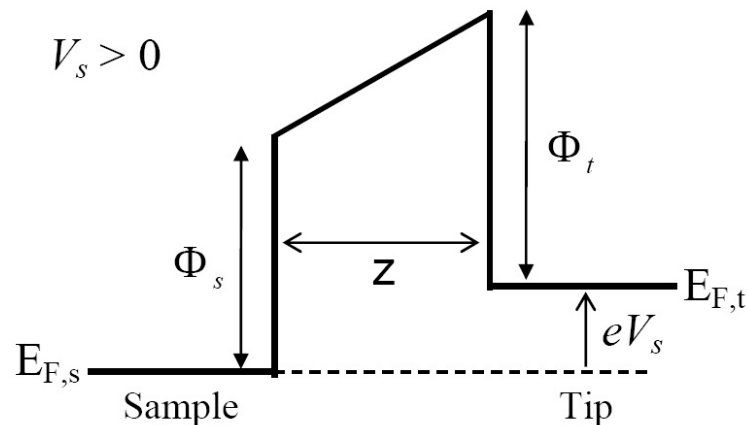
Figure 3.1: An illustration of the STM tunneling process for positive sample bias

A schematic illustration of the STM tunneling process when probing the empty states of the sample (i. e. when V_s is positive) is shown in figure 3.1. Ignoring the position dependence, the WKB result for the tunneling current is

$$I(V_s, z) = \int_0^{eV_s} \rho_s(E_F + eV_s - \varepsilon)\rho_t(E_F - \varepsilon)\exp\left[-2z\sqrt{\frac{2m}{\hbar^2}\left(\frac{\phi_s + \phi_t - eV_s}{2} + \varepsilon\right)}\right]d\varepsilon \quad (3.1)$$

Assuming a flat density of states for the tip,

$$I(V_s, z) \propto \int_0^{eV_s} \rho_s(E_F + eV_s - \varepsilon)\exp\left[-2z\sqrt{\frac{2m}{\hbar^2}\left(\frac{\phi_s + \phi_t - eV_s}{2} + \varepsilon\right)}\right]d\varepsilon \quad (3.2)$$

If ρ_s is more rapidly varying than the exponential function, then the leading term is

$$dI/dV_s \propto \rho_s(E_F + eV_s)\exp\left[-2z\sqrt{\frac{2m}{\hbar^2}\left(\frac{\phi_s + \phi_t - eV_s}{2}\right)}\right] \quad (3.3)$$

Therefore, the differential conductance is proportional to the local density of states of a sample.

3.1.2 Instrument set up and data example

A *dI/dV* spectrum (or *dI/dV* image) of a sample can be measured by applying a small sinusoidal modulation signal to the sample bias. A lock-in amplifier allows easy control of the modulated signal's amplitude, frequency, etc. An illustration of STM equipped with a Lock-in amplifier is given in figure 3.2.
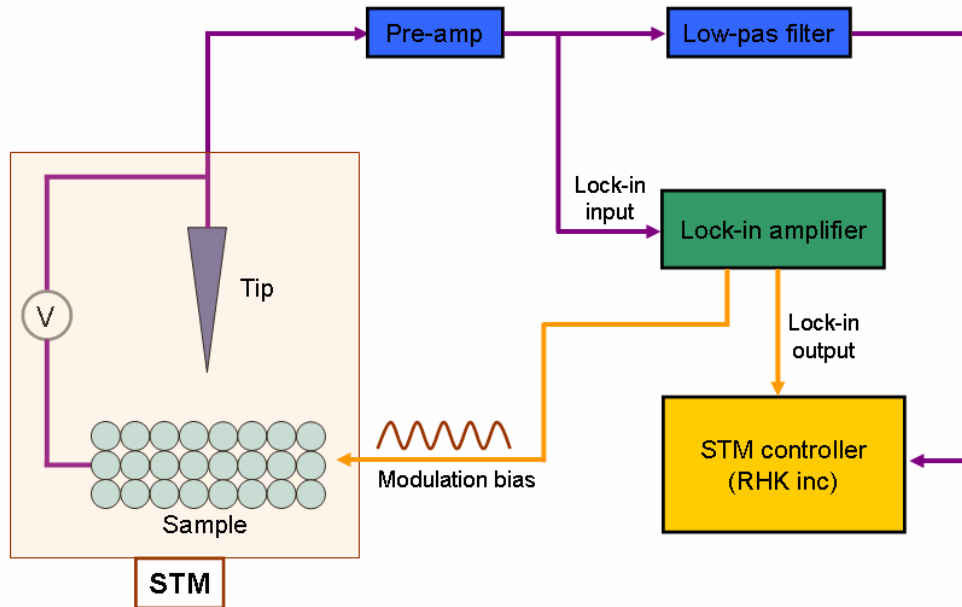
Figure 3.2: A schematic of a lock-in amplifier connected to an STM system for *dI/dV* image measurement.

It is important to set the modulation frequency high enough so that the STM's feedback does not pick up any part of the modulation and try to compensate it; therefore, the lock-in modulation frequency should be much lower than the bandwidth of the feedback loop. The Lock-in amplifier only detects the portion of input signal which contains the same frequency as the modulation. Therefore, it is always better to set the modulation frequency far away from any existing noises so that its output will not be affected by noises. For a *dI/dV* spectrum measurement, the pre-sample delay (a waiting time before starting to take a spectrum) should be long enough for the Lock-in amplifier to reach a stable value. Typically, this delay can be 2~3 times the time constant setting of the lock-in amplifier. Similarly, for a *dI/dV* image measurement, scanning speed can not be too fast as the Lock-in amplifier needs time to reach its equilibrium value at each pixel. The time allowed for each pixel can be 2~3 times the value of the time constant setting of the lock-in amplifier.

27
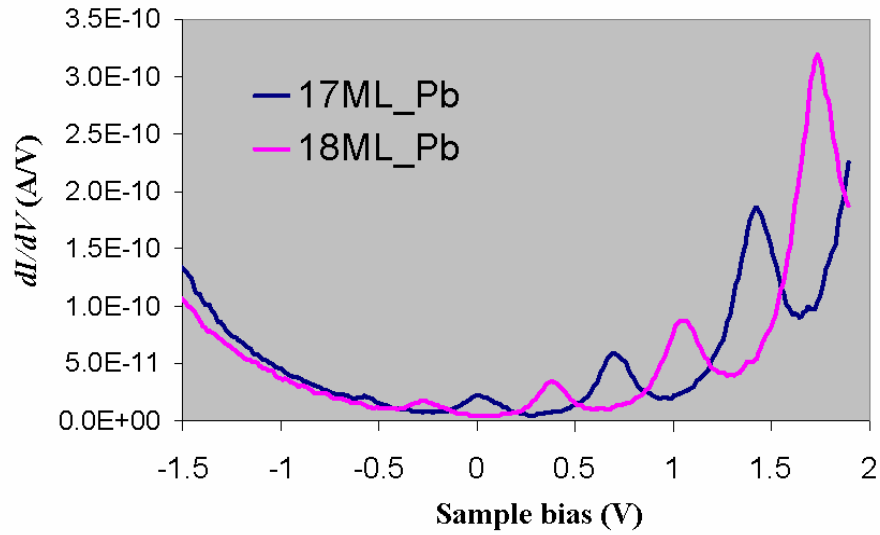
Figure 3.3: An example of a *dI/dV* spectrum taken on two Pb films of different thicknesses

An example of a *dI/dV* spectrum taken by a Lock-in amplifier is shown in figure 3.3. The spectra are taken from two Pb films of different thickness on Si(111). Recalling that the differential conductance reflects the local density of states (LDOS), the peaks in the spectra represent quantum well states formed by electron confinement perpendicular to the substrate. Although the same *dI/dV* spectrum can be obtained by using numerical differentiation of an *I-V* curve, the lock-in technique has a cleaner, spectrum especially when the tunneling current is a bit noisy.
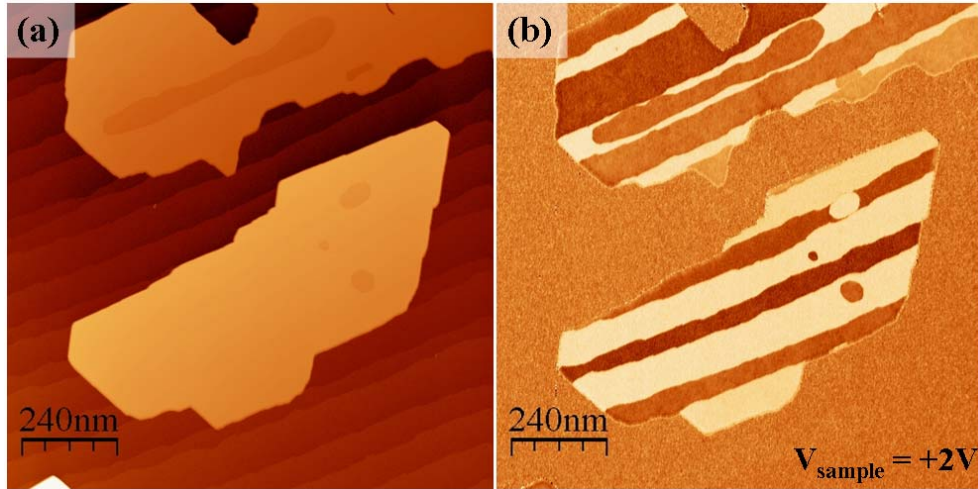
Figure 3.4: An example of *dI/dV* image by using a Lock-in amplifier. (a) An STM topography image of Pb/Si(111). The Pb 2D flat-top mesas contain regions of different thicknesses due to the stepped structures of the Si(111) substrate (V_{sample} = 2 V and I_0 = 100pA). (b) A conductance image taken simultaneously by a lock-in amplifier with the topography image (a).

Figure 3.4 presents an example of a conductance (*dI/dV*) image for Pb islands on Si(111) taken by a Lock-in amplifier. A 10 mV modulation signal of 2 kHz is applied to the sample bias for the conductance image (b). The color contrast in (b) indicates a relative strength of LDOS at the given sample bias of 2 V, and the different contrast of each thickness of Pb is clearly observed because of the different energy locations of quantum well states.

3.2 CURRENT VS. TIP-SAMPLE DISTANCE (*I-Z*) SPECTROSCOPY

The tunneling current in STM can be expressed as $I \propto e^{-2\kappa z}$, where κ is the tunneling decay constant and z is the tip-sample distance. If the tunneling current is recorded with feedback disabled while the tip moves away from the sample surface, this current vs. tip-sample distance (*I-z*) spectrum typically exhibits exponential behavior. Therefore, when the *I-z* spectrum is plotted on a linear (z) - logarithmic (I) scale, it should

show linear behavior.   Then, the tunneling decay constant (κ) can be extracted by a linear fitting routine of the slope of *I-z* spectrum as $\ln I = -2\kappa z$.   One can further define an effective tunneling barrier height simply as $\Phi_{eff} = (\hbar\kappa)^2/2m$.   Many surface features such as absorbates and defects can modify the surface electronic states, resulting in a local variation of the barrier height, and this can be observed by acquiring *I-z* curves. By a similar method as explained in section 3.2, it is possible to measure a *dI/dz* image simultaneously while taking a topography image by using a Lock-in amplifier.

3.2.1 *I-z* spectroscopy using a Lock-in amplifier

As explained briefly in the previous section, obtaining a tunneling decay constant (κ) is the first step of *I-z* spectroscopy because it is related to various physical properties such as tunneling barrier height, work function, and surface reactivity.   In this section, I will explain the details of how κ can be measured using a Lock-in amplifier in an STM.

We starts with the simple expression of a tunneling current, $I \propto e^{-2\kappa z}$.   Using a Lock-in amplifier, we can modulate the tip-sample distance (z) with a sinusoidal wave form of a tiny amplitude, δz.   Then, *z* and *I* can be written as

$$z = z_0 + \delta z \cos(wt) \quad \text{and} \quad I \propto e^{-2\kappa z_0} e^{-2\kappa \delta z \cos(wt)} \tag{3.4}$$

where z_0 is an initial tip-sample distance with a set-current $I_0 \propto e^{-2\kappa z_0}$ (assuming that the feedback does not "feel" the existence of *z* modulation; i.e. the modulation frequency is sufficiently higher than the feedback bandwidth).   Then, in order to simplify the expression, Taylor's expansion can be applied to the exponential:

$$I \propto I_0[1 - 2\kappa \delta z \cos(wt)] \tag{3.5}$$

A Lock-in amplifier detects only the portion of the input signal which contains the same frequency as the modulation.   In our case, the input signal is a sinusoidal wave form of I due to the z modulation.   Then, the lock-in output sent into an STM controller is usually the rms value of the $\cos(\omega t)$ term.   Lock-in output (I_{lock}) is

$$I_0 \times 2\kappa \delta z \xrightarrow{\quad rms \quad} I_{lock} = I_0 \times 2\kappa \delta z \times \frac{1}{\sqrt{2}} = I_0 \times 2\kappa \delta z_{rms} \qquad (3.6)$$

Therefore, the final form of κ can be written as

$$\kappa = \frac{I_{lock}}{2I_0 \delta z_{rms}} \qquad (3.7)$$

It should be mentioned that on most Lock-in amplifiers the modulation voltage selected is also the rms value when the modulation amplitude is set.

3.2.2 Instrument set up and data example

A tunneling decay constant mapping (dI/dz image) of the sample surface can be measured by applying a small modulation signal of a sinusoidal wave to the tip-sample distance (z).   The easiest way to get it is to use a Lock-in amplifier.   An illustration of dI/dz spectroscopy is shown in figure 3.5.
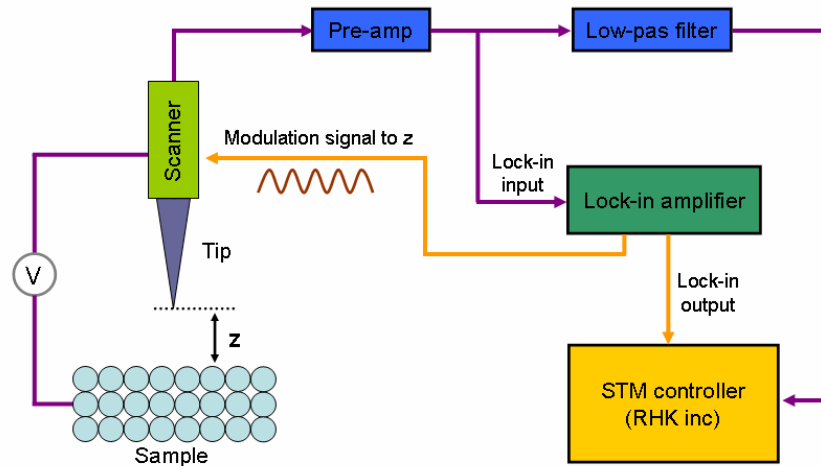
Figure 3.5: A schematic illustration of a Lock-in amplifier connected to an STM system for *dI/dz* image measurement.

The Lock-in measurement rules explained in *dI/dV* spectroscopy (section 3.2) are still valid here to determine the proper settings of modulation frequency, scanning speed, and pre-sample delay. Figure 3.6 shows an example of a *dI/dz* image taken of a Pb island on Si(111). A 4 mV modulation signal with 2 kHz is applied to the z piezo of scanner by the Lock-in amplifier. The color contrast in the images represents a relative value of the tunneling decay constant. Furthermore, with the right conditions, the work function information of the sample can be extracted from *dI/dz* images (see chapter 4 for details).
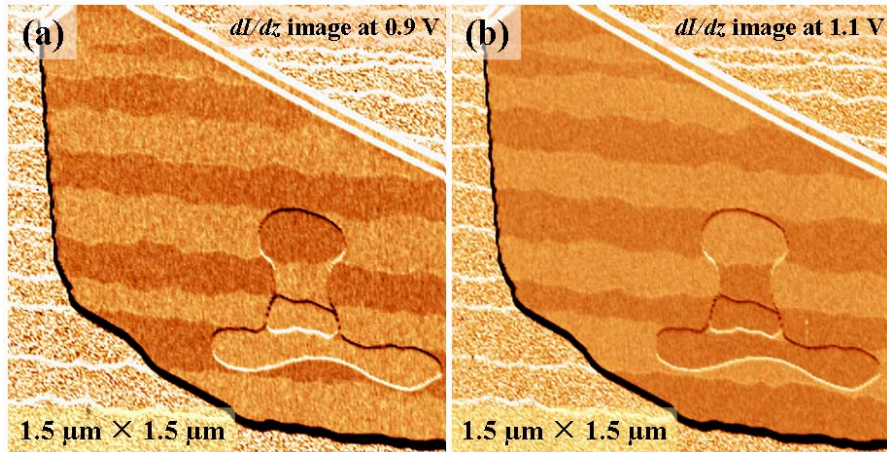
Figure 3.6: *dI/dz* images taken by a lock-in amplifier. A flat top Pb mesa is sitting on Si(111) substrate.

3.3 CURRENT IMAGING TUNNELING SPECTROSCOPY (CITS)

Current imaging tunneling spectroscopy (CITS) is a powerful STS technique where a tunneling spectrum is measured for every pixel of the STM topography, providing a map of the spectrum in real space as a function of bias. The spatial resolution cannot be as high as a typical topography image because it will amplify the measurement time tremendously. The conductance (*dI/dV*) mapping can be obtained by taking a numerical derivative of the *I-V* spectrum or using lock-in amplifier techniques, as described in section 3.1.

3.3.1 Instrument setup and data examples

In order to get reliable CITS data, there are two conditions that a LT-STM system needs to satisfy: (a) cryogenic liquids should last long enough to finish a required CITS measurement[1], and (b) during the measurement, very low thermal drift and piezo creep

---

[1] A 64 by 64 pixel lateral resolution of *dI/dV* CITS can take easily 12 hours or more.

are absolutely required, otherwise the spatial mapping of LDOS will be distorted. Thermal drift can be minimized by matching the thermal expansion coefficients of all materials used in the STM head (also see section 2.2.1).
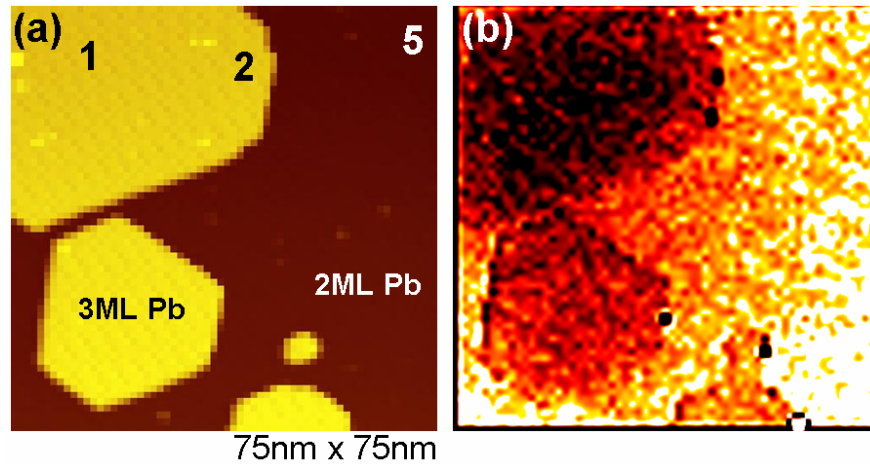
Figure 3.7: An example of a CITS image taken simultaneously with a topography image. (a) A topography image of 3ML Pb islands sitting on a 2ML Pb island. (b) A CITS image shows a *dI/dV* mapping at zero bias which reflects the local superconductivity.

The general setup for CITS measurement can be referred to previous sections (3.2 and 3.3). Figure 3.7 shows an example of differential conductance CITS data taken from 3ML Pb islands on a 2ML Pb island. Both images of figure 3.7(a) and (b) are taken at 64 by 64 pixel resolution which needs around 16 hours to complete. The CITS image of figure 3.7(b) presents the conductance mapping at zero sample bias (called zero bias conductance) which directly reveals the depth of the superconducting gap. Therefore, its color contrast reflects the variation of local superconductivity (darker color means lower superconducting transition temperature) due to lateral proximity effects. More details of this intriguing result will be discussed in chapter 6.

3.4 FIELD EMISSION RESONANCE (*Z-V*) SPECTROSCOPY

By applying a bias voltage higher than the local barrier height (or the local work function), an STM can be operated in the field emission regime. Spectroscopic investigations in the field emission regime reveal the existence of field emission resonances, as predicted by Gundlach [7]. Gundlach oscillation, which can be observed in STS, is a phenomenon in which field emission resonance with standing wave states in the tip-sample tunneling barrier, and it is used to study the dynamics of surface electrons [8,9].

3.4.1 Field emission resonances

In a one dimensional tunneling model, when a sample bias voltage is higher than the work function, the tunneling barrier becomes triangular in shape, rather than its typical trapezoidal shape (see figure 4.3(c)) as illustrated in figure 3.8. With a strong enough bias, the electron can tunnel through a reduced barrier width rather than the entire gap s between the tip and sample surface [10].

$$s'(V) = s \cdot (\phi / eV) \tag{3.8}$$

In figure 3.8, the boundary conditions at the potential barrier of sample surface (*z=s*) and the electron's classical turning point (*z=s'*) give rise to the formation of standing waves. The detailed shape of the tunneling barrier and the electron energy determine the allowed modes for the standing wave. When there is an overlap of tip and sample wave functions, the field emission current occurs. The electron wave function in the sample has resonantly-enhanced amplitudes outside the sample surface when one of the allowed standing wave modes in the vacuum is fulfilled. Eventually this gives rise to field emission resonances in tunneling current. Here, for simplicity, we assume that

the DOS of the tip and sample changes very smoothly so that it does not influence the transmission probability.
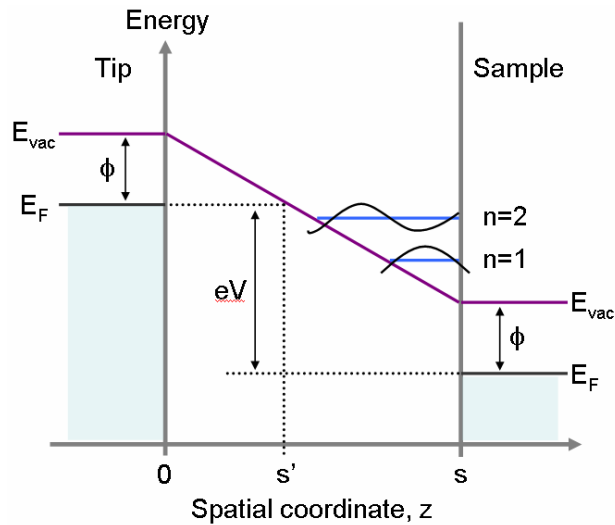
Figure 3.8: A schematic energy diagram of field emission resonance.

3.4.2 An example of *z-V* spectroscopy

Among various methods of STS, *z-V* (or *dz/dV*) spectroscopy is one way to observe the field emission resonances associated with the standing wave states in the vacuum barrier explained in previous section. The basic operating principle of *z-V* spectroscopy is very similar to *I-V* spectroscopy except a few differences: (a) the sample bias voltage should be high enough for electrons to overcome the work function of either the tip or the sample, and (b) unlike conventional *I-V* spectroscopy, the feedback loop needs to be turned on while ramping the bias in *z-V* spectroscopy. Then, to keep the tunneling current at a constant value, the feedback will adjust the tip height, *z*, to compensate for the change of sample bias. When the bias matches the energy of a possible standing wave formed between tip and sample, there is a sharp increase in the

36

tunneling current and hence a sharp rise in the tip-sample distance. Figure 3.9(c) shows

an example of *z-V* spectroscopic data, taken from various thicknesses of Pb islands on

Si(111). The features of field emission resonance become obvious in the *dz/dV* spectra

(figure 3.9(d)), obtained by a numerical differentiation of the *z-V* spectra, and the peaks

in the *dz/dV* spectra directly reflect the sharp resonances of field emission. A detail

study of field emission resonance for Pb/Si(111) system is done by Liu *et al.* [11]. They

found that the resonance energies show a bilayer oscillation as a function of film

thickness and this oscillation results from the confinement of the highly excited scattering

states by the quantum well. Actually, the bilayer oscillation nature of field emission

resonance in Pb/Si(111) system can be observed in figure 3.9(d).
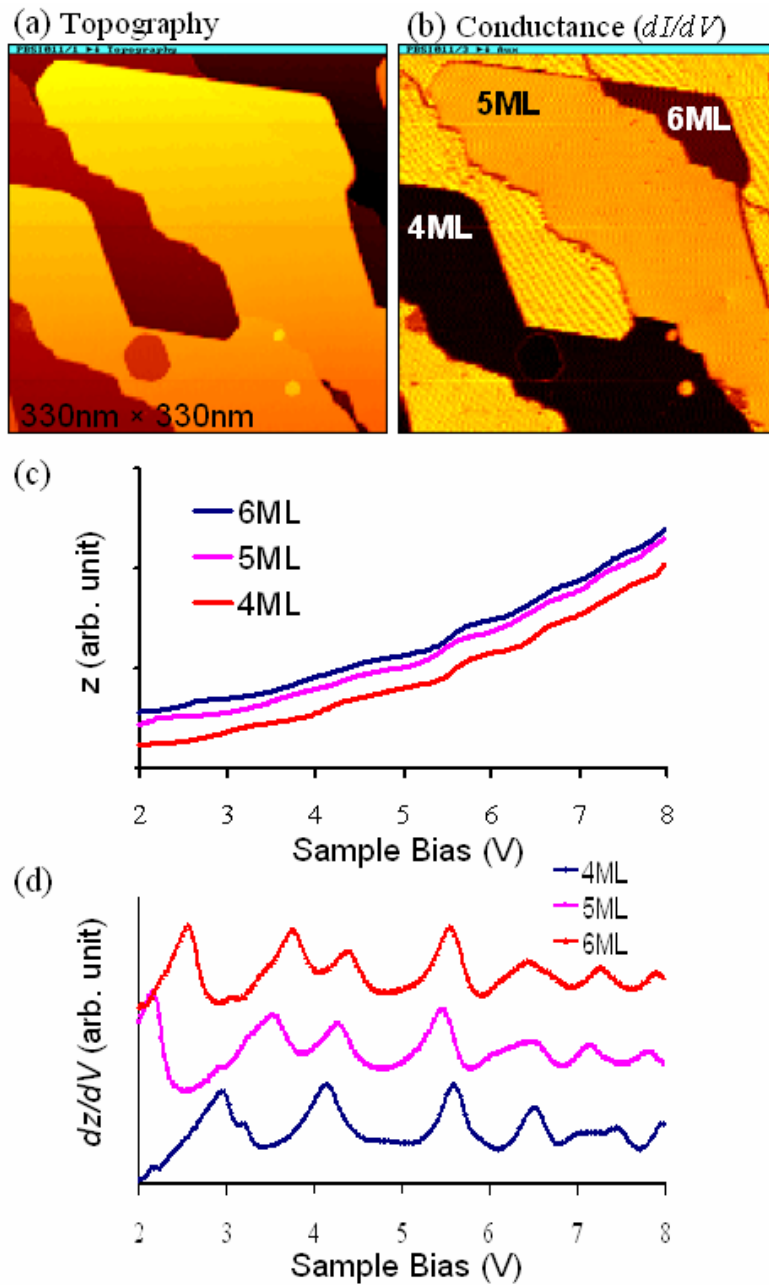
Figure 3.9: An example of *z-V* and *dz/dV* spectra taken from Pb islands on Si(111).   (a) STM topography image where (c) and (d) spectra are taken (V_{sample} = 2V, I_0 = 0.1nA). (b) A simultaneously measured *dI/dV* image by using a lock-in amplifier.   (c) *z-V* spectra of Pb islands.   (d) *dz/dV* spectra obtained by the numerical differentiation of *z-V* spectra (c).

Chapter 4:   Quantum Size Effects on The Work Function of Metallic Thin Film Nanostructures

The work function, the minimum energy required to move an electron from a solid into the vacuum, is the most fundamental material parameter in surface science. It plays a key role, for example, in the photo-electric effect, one of the first phenomena through which quantum mechanics unveiled itself. The work function is the result of a complex interplay between quantum mechanics and forces on the atomic scale. Recent studies suggest the exciting possibility of controlling the work function through quantum engineering of electronic structures at the nanoscale [12-16]. Such efforts are, however, still in their infancy, and there are many puzzles and contradictions in the observations so far that hinder further progress [12-16]. We have found direct evidences for quantum size effects on the work function in ultra-thin Pb films. We further establish the direct correlation of this quantity with the behavior of quantum well states. With the known techniques to control the growth of metallic thin films with atomic layer precision, this new work will bring reality to the ultimate goal of "quantum engineered" metallic thin films for desirable chemical and physical processes on solid surfaces.

4.1 QUANTUM SIZE EFFECTS

For classical metallic systems, the free electron approximation is one of the simplest ways to understand many of its physical properties. However, when the thickness of a metal is thin enough to be comparable with the Fermi wavelength, this system can not be treated as a classical free electron system. In an ultra-thin metal (free-standing) system, each boundary between metal surface and vacuum creates a

potential well, and then it can be treated as a simple quantum mechanics problem of electrons trapped in a potential well as shown in figure 4.1.
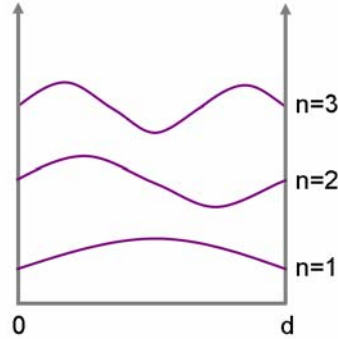
Figure 4.1: One dimensional quantum well with infinite potential barriers. The size of the potential well, *d*, is determined by the thickness of the metal.

By solving the Schrödinger equation, the wave function of electrons can be expressed as

$$\Psi_n(x,t) = \sqrt{\frac{2}{d}}\sin(k_n x)e^{-i\omega_n t}, \, k_n = n\pi/d \, (n = 1, 2, 3, \ldots) \quad \text{for } 0 < x < d \qquad (4.1)$$

where k_n is the allowed wave number. These allowed wave functions are also called quantum well states (QWS). The energies which correspond with each wave function in (4.1) is

$$E_n = \frac{n^2\hbar^2\pi^2}{2md^2}. \qquad (4.2)$$

As shown above, the electron energy bands are discretized and form QWS due to the quantum confinement of the potential well. The discretization can lead to the quantum size effects on various physical properties of ultra-thin metallic systems. One example is the oscillatory dependence of the metal's total energy on its thickness, implying that certain thicknesses may be more energetically favored than other thicknesses. This so called "quantum growth" behavior was first observed in Ag/GaAs [6]. In fact, theoretical study of the quantum size effects was already done several decades ago by Shulte [17]. He

showed that theoretically many physical properties of thin metal films, such as electron densities, potentials and work functions, show oscillations with a period of one half the Fermi wavelength as a function of film thickness.

4.1.1 Pb on Si(111) system

When low temperature growth (at ~100K) is performed, certain thicknesses are favored to be formed when there is a phase matching between the layer thicknesses, d, and Fermi wave vector k_F:

$$2k_F d + \Phi_s + \Phi_i = 2\pi n \tag{4.3}$$

where Φ_s and Φ_i are the phase shifts in the wave function scattered at the film surface and interface, respectively [18]. This phase matching condition is exactly the same as the allowed wave vector $k_n = n\pi/d$ ($\lambda_F = 2d/n$) in previous section, except for two phase shift factors introduced for a more realistic model. It is clear that the relationship between d and λ_F plays an important role in the phase matching condition. In the case of Pb, interestingly, λ_F and monolayer thickness t_0 have a unique relation which is almost half-integer matching of $1.5\lambda_F \sim 2t_0$. For this reason, the Pb on Si(111) system has been widely studied because the half-integer matching condition causes profound quantum size effects exhibiting an intriguing bi-layer oscillation on various physical properties of Pb films [11,18-26].

Figure 4.2 presents the experimental result of QWS energy locations as a function of Pb thicknesses taken by STM. Those dots in the figure indicate the energy for each thickness, which can be found from the peak location in dI/dV spectrum (see figure 3.3). If we look at the QWS near the Fermi energy level (E_F), they exhibit a bi-layer oscillation behavior of film stability; i.e. those thicknesses which have QWS relatively closer to E_F

than neighboring thicknesses are energetically favored (or stable) to form a flat film.   In the half-integer matching of $1.5\lambda_F \sim 2t_0$, there is a tiny error and the accumulation of this error as the Pb film gets thicker eventually gives rise to a cross-over of the phase matching.
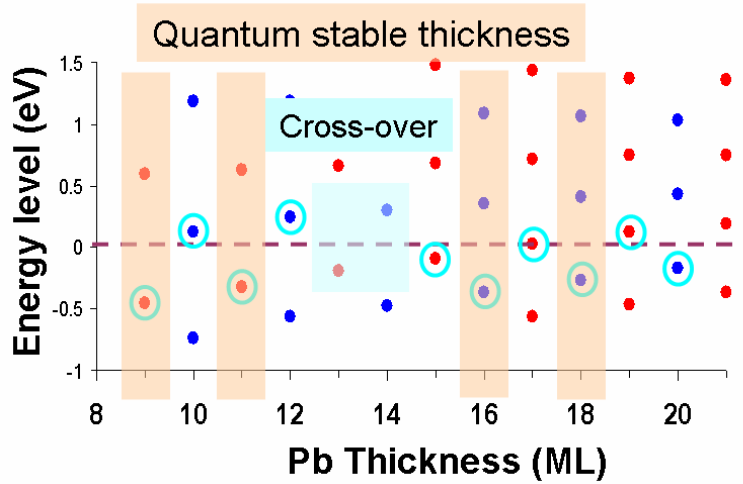
Figure 4.2: The quantum well states energy locations as a function of Pb thickness. These dots represent the energy location of QWS for each thickness.   The Fermi energy level is marked by a horizontal dashed line and those QWS near the Fermi level are marked by circles.

4.2 INTRODUCTION TO QUANTUM SIZE EFFECTS ON WORK FUNCTION

It should be noted that theoretical investigations of quantum size effects (QSE) on the work function (Φ) were carried out several decades ago [17].   By using a Jellium Model and continuously varying the film thickness as a parameter, Schulte showed that the QSE leads to work function oscillations as a function of layer thickness.   Moreover, it was found that the Φ oscillations are directly related to the locations of the quantum well states (QWS).   In particular, whenever a QWS channel crosses the Fermi level

(E_F), there is a negative cusp in Φ as a function of film thickness (L). Subsequent theoretical investigations using more sophisticated methods, while allowing more realistic electronic structure calculations, did not call into question this basic tenet regarding the correlation of Φ and QWS [18,21].

Experimental investigations of this effect remained dormant for almost 30 years. The situation, however, changed dramatically with recent advancements in the quantum control of thin metal film growth[6,19,20,24-30], by which epitaxial metallic thin films can be grown on semiconductor substrates with atomic layer precision. One example is shown in Fig. 4.3(a), where an epitaxial Pb film was grown on a Si(111) substrate. The scanning tunneling microscopy (STM) image reveals the smoothness and the thickness uniformity of the Pb film where the steps on the over-layer directly reflect the substrate steps. This sample system, epitaxial Pb thin film on Si(111), is the most widely studied system for the investigation of QSE, and many of its physical quantities have been shown to exhibit so-called "quantum oscillations" as a function of layer thickness[22-24]. While such atomically smooth, uniform thickness metal films can be grown with near perfection, it is more convenient for direct investigation of QSE to use a different growth process which leads to the formation of large 2D flat-top mesas on the stepped region. These mesas contain regions of different thicknesses in one mesa[20]. An example is shown in Fig. 4.3(b), spanning thicknesses ranging from 9 to 19 monolayers (ML). The lateral extent for each film thickness ranges from 50 to 100 nm, about two orders of magnitude larger than the thickness. Moreover, the experimental measurements using STM are performed at ~1 nm above the surface. One thus can safely assume that the measurements performed in the local region can be used to represent an extended film of the same thickness. On such flat-top mesas, the variation of work function as a function of thickness can be probed by measuring the tunneling decay constant (κ).
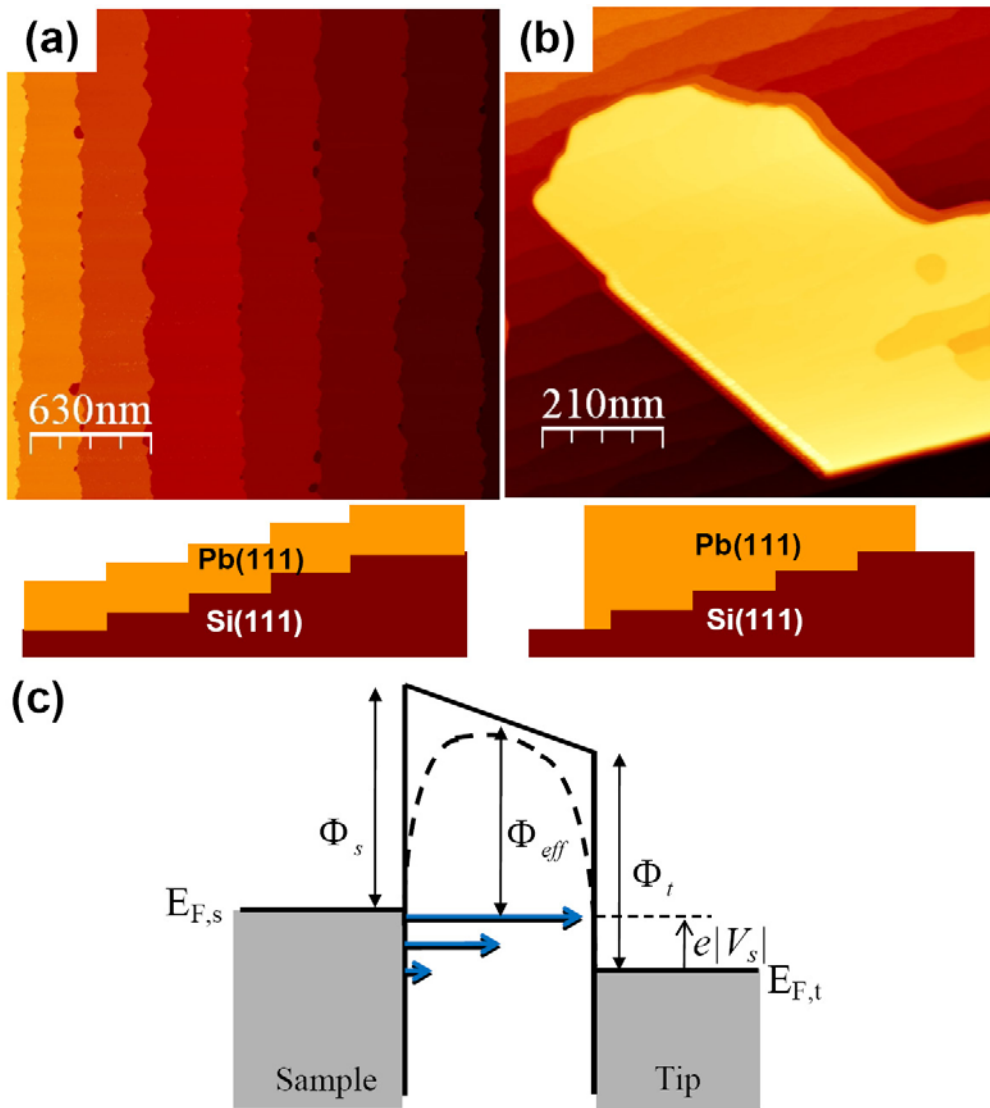
Figure 4.3:   STM topography images of a globally flat Pb film and a flat top Pb mesa. (a) A globally flat 2ML Pb film on Si(111).   (b) A flat top Pb mesa on Si(111).   Both images were taken with sample bias $V_s = 2$ V, and tunneling set current $I_0 = 100$ pA.   (c) An illustration of a one-dimensional tunneling junction for the STM configuration.   The effect of the image potential is shown as a dashed curve between the sample and tip. Φ_s and Φ_t are the work functions for the sample and tip, respectively. Φ_{eff} is the effective tunneling barrier height with an applied bias V_s across the junction.

In an STM configuration the tunneling current between the two metallic electrodes (tip and sample) decays exponentially with respect to the tip-to-sample

44

distance, z, and can be expressed as $I \propto e^{-2\kappa z}$. From this general expression, the tunneling decay constant κ can be defined operationally as $\kappa \equiv -d \ln I / 2dz$ which is an experimentally measured quantity. One can further define an effective barrier height simply as $\Phi_{eff} = (\hbar^2 \kappa^2)/2m$. Often, the tunnel junction is approximated with a one dimensional trapezoidal tunneling barrier (see Fig. 4.3(c)). Within this approximation, if the density of states (DOS) is smoothly varying in energy, then the effective barrier can be expressed as

$$\Phi_{eff} = (\Phi_s + \Phi_t - e|V_s|)/2 \tag{4.4}$$

where Φ_s and Φ_t are the work functions of the sample and tip respectively and $|V_s|$ is the bias applied across the tunnel junction. Shown in Fig 4.3(c) is the configuration with a negative sample bias V_s (relative to the tip electrode), where the tunneling current would be dominated by the tunneling channel between the highest occupied states of the sample, namely $E_{F,s}$, and the unoccupied states of the tip electrode at $E_{F,t} + e|V_s|$ (labeled by the largest horizontal arrows). Note that the same expression (4.4) applies for the case with a positive sample bias, where the dominating tunneling channel occurs between the highest occupied states of the tip electrode, namely $E_{F,t}$ and the unoccupied states of the sample electrode at $E_{F,s} + eV_s$. Thus, when the approximation (4.4) is valid, the sample work function can be extracted if the tip work function is known. This is the basic principle behind work function measurements using STM.

While this approximation ignores the effect of the image potential, which can lower the effective barrier (as shown by the dashed curve in Fig. 4.3(c)), it is expected that the correction should be relatively minor. The method just described has been routinely applied ever since the invention of STM and has largely yielded good information about the sample work function, although it was also recognized early that the effective barrier height is often influenced by detailed band structures [31].

45

Furthermore, if one focuses primarily on the work function difference on different surfaces, the correction is cancelled.

4.3 EXPERIMENTS

The experiments were conducted in a home-built low temperature STM system with *in-situ* sample preparation chamber. Pb was deposited onto atomically clean Si(111) 7×7 surfaces at room temperature with a flux rate of 0.5 ML/min by using a thermal evaporation technique. The room temperature growth of Pb leads to the formation of (111)-oriented 2D flat-top mesas on the stepped region, which is convenient for STM investigation since one mesa contains regions of different thicknesses. Moreover, the local thickness referenced to the wetting layer can be unambiguously determined. The base pressure of the system was maintained at better than 1.0×10^{-10} torr during the sample preparation. All STM measurements were done at 78 K with liquid nitrogen cooling.

At a constant current I_o, the value of $\kappa \equiv -d \ln I / 2dz$ is directly related to *dI/dz* as $\kappa = -(dI/dz)/2I_o$. Spatial mapping of κ was acquired simultaneously with the topography image by simply using a lock-in amplifier to measure the *dI/dz* signal. Throughout the measurement, we used a z-modulation amplitude of 0.01 nm and a modulation frequency of 2 kHz.

4.4 RESULTS AND DISCUSSION

Presumably, to unravel the QSE on the work function of ultra-thin films, one can simply measure the tunneling decay constant, κ, as a function of the layer thickness. Earlier works by Qi *et al.* [16] and Ma *et al.* [13] used precisely this approach and claimed to

have observed QSE on the work function of ultra-thin films. However, as we show in this paper, the very existence of QWS in these ultra-thin films has a profound effect on the measurements of κ itself, resulting in a very rich phenomenon of "quantum oscillations" in κ as a function of thickness, L, and also as a function of sample bias voltage, V_s. The phenomenon is rooted in the sharp resonances of QWS in these thin films, which renders approximation (1) inapplicable for most of the bias range except for the limit where V_s approaches zero. As a result, $\kappa(V_s; L)$ shows markedly different behaviors in three different regimes: (i) empty states ($V_s > 0.2$ V), (ii) filled states ($V_s < -0.2$ V), and (iii) the very small bias regime ($|V_s| < 0.03$ V). We further show that indeed in regime (iii) the measurements yield correct information about work function, thus allowing us to unravel the QSE on the work function of this prototypical materials system.

4.4.1 Empty state regime ($V_s > 0.2$ V)

The in-applicability of approximation (4.4) in the presence of sharp QWS resonances can be understood by looking at the schematic diagram shown in Fig. 4.4(a). Considering first a positive sample bias which lines up the tip Fermi level ($E_{F,t,1}$) with the lowest unoccupied QWS (LUQWS) above the sample Fermi level ($E_{F,s}$), the effective tunneling barrier height is marked by a vertical arrow and labeled as $\Phi_{eff,1}$. When the bias is raised so that $E_{F,t,2}$ is above the first QWS, from approximation (4.4), one would expect a lowering of the effective barrier height. However, the effective barrier height actually increases (as shown by the dashed vertical arrow, labeled $\Phi_{eff,2}$), since the tunneling is still dominated by the LUQWS. This trend would continue until the tip Fermi level reaches the next unoccupied QWS. The tunneling will then be dominated by the second QWS, and one expects a sudden drop in effective barrier height. As a

result, the decay constant (κ) should show oscillatory behavior as a function of bias, and the valleys in κ oscillation should coincide with the QWS peaks. Shown in Fig. 4.4(b) and 4.4(c) are spectra of *dI/dV* and κ *vs.* V_s respectively for 9 and 10 ML films. Indeed, the oscillations in κ *vs.* V_s are correlated with the QWS positions with the valleys in κ *vs.* V_s coinciding with the peaks in *dI/dV* (labeled by the arrows with different colors for different thicknesses).

This correlation leads to very interesting behaviors of bias-dependent mapping of the decay constant κ. Shown in Fig. 4.5(a) and 4.5(b) are images of κ of an island, containing local regions with thicknesses ranging from 9 to 19 MLs, at two different bias voltages, V_s = +1.2 V and +0.7 V, respectively. One obvious feature in the κ-image is the contrast between different thicknesses. For example, in Fig. 4.5(a) all odd layers have higher κ values than the neighboring even layers. On the other hand, in Fig. 4.5(b), the contrast is exactly reversed: all even layers have higher κ values than the odd layers. The odd-even bi-layer oscillations, often referred to as quantum oscillations in the literatures, are the consequence of nearly half integer phase matching between the Fermi wave-length and the interlayer spacing for Pb (111) ultra-thin films[18,21]. The *contrast reversal* in κ, on the other hand, is a consequence of the onset of different QWS at the imaging bias: at V_s = +0.7 V, the bias is close to the peak positions of the QWS for the odd layers (thus depressions in κ for odd layers), while at V_s = +1.2 V it is close to the QWS peaks for even layers. Although this phenomenon itself is interesting, such a bias-dependent behavior of κ *vs.* L and its correlation with the QWS locations (see also the top panel of Fig. 4.7(a)) raise serious questions about using measurements of effective barrier heights to extract the work function because the contrast in work functions at different thicknesses should be a fixed quantity. This effect is explored further using theoretical simulations.

Consider that the sample DOS, $D(E)$, is largely reflected in the dI/dV spectra through the relation $\frac{dI}{dV_s} \propto D(eV_s) \exp\left[-2z\sqrt{\frac{2m}{\hbar^2}\left(\frac{\Phi_s - eV_s + \Phi_t}{2}\right)}\right]$. This relationship allows us to extract $D(E)$ from the experimental dI/dV spectra in Fig. 4.4(b). Using the extracted $D(E)$, the tunneling current versus a small change in barrier width z is calculated to obtain κ. Shown in Fig. 4.4(d) are theoretical simulation curves of κ vs. V_s for 9 and 10 MLs, respectively. Note that all calculations are done for infinite flat surfaces. The solid lines are the theoretical results with a fixed work function $\Phi \equiv \frac{\Phi_s + \Phi_t}{2} = 4$ eV for both 9 and 10 MLs. One can see that the oscillatory behavior of κ vs. V_s is well reproduced and the phases of oscillations for 9 and 10 MLs are complimentary, as we have observed, except at very low sample bias. We notice, that, if the value of Φ is lowered by 0.08 eV for 10 ML in the simulation, then the low bias behavior is also well reproduced (dashed line), suggesting the existence of a true work function difference between 9 and 10 MLs. Nevertheless, such an inference is not a direct experimental measurement.
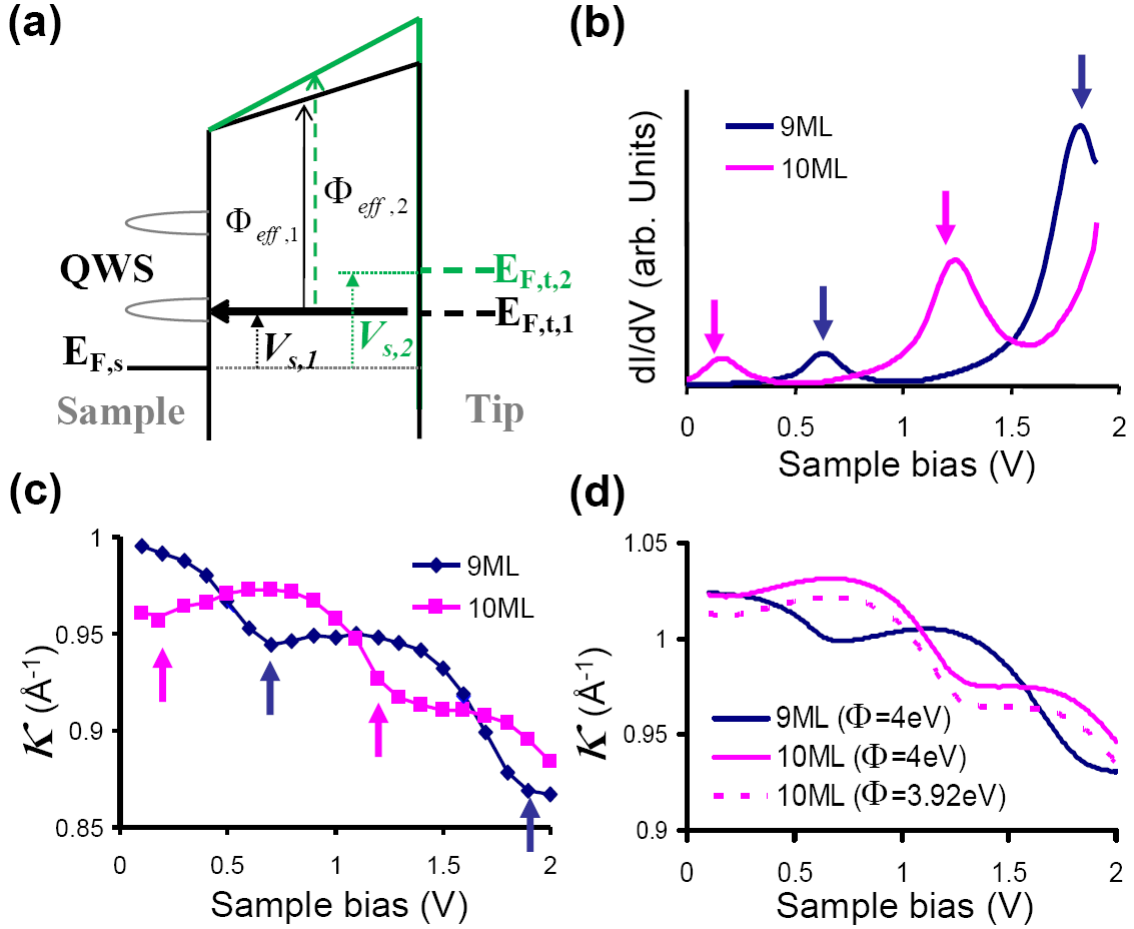
Figure 4.4: (a) A schematic illustration of the STM tunneling process when probing the empty states of the sample (i. e. when V_s is positive). The Fermi levels of the sample and tip are labeled by $E_{F,s}$ and $E_{F,t}$ respectively. $E_{F,t,1}$ and $E_{F,t,2}$ show the energy level of $E_{F,t}$ at two different applied biases $V_{s,1}$ and $V_{s,2}$. The unoccupied QWS are represented by the curved lines in the sample side. The vertical arrows represent the effective barrier height, κ_{eff} at different bias conditions. (b) Differential conductance spectra (dI/dV) for 9 and 10 MLs. The peak positions in the dI/dV spectra correspond to the locations of QWS in the empty states for each thickness. (c) Measured κ vs. V_s for 9 and 10 MLs. All κ images used to extract κ vs. V_s were taken under same tunneling set current $I_0 = 100$ pA without changing the tip or sample. (d) Theoretical simulation of the bias dependence of κ for 9 and 10 ML with an assumption of $\Phi = (\Phi_s + \Phi_t)/2 = 4$ eV for the solid lines and 3.92 eV for the dashed line of 10 ML.
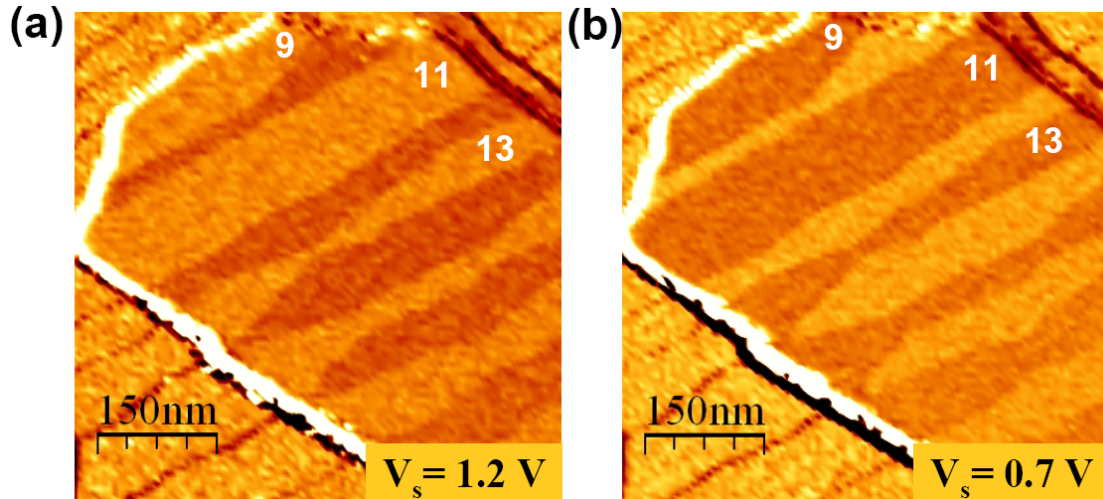
Figure 4.5:   (a), (b)   images taken at V_s = 1.2 V and 0.7 V respectively for the same island shown in Fig. 1(b).   Odd numbers labeled on the images indicate the number of underlying ML.   The apparent contrast of each layer clearly exhibits a bilayer oscillation behavior and the contrast of (e) is completely reversed in (f).Filled state regime ($V_s <$ −0.2 V)

4.4.2 Filled state regime ($V_s <$ −0.2 V)

The behavior of κ vs. V_s and κ vs. L in the *filled states* (i.e., negative sample biases), on the other hand, is very different from the behavior in the empty states.   As illustrated by the schematic shown in Fig. 4.6(a), at a negative sample bias, whenever the tip Fermi level is below the highest occupied QWS (HOQWS), the tunneling process is dominated by this HOQWS (labeled by the black arrow), regardless of the presence of other occupied QWS.   Thus, the effective barrier height will be primarily determined by this tunneling channel.   Indeed, this is observed experimentally.   Shown in Fig. 4.6(b) are *dI/dV* and κ vs. V_s for 9 ML film probed at negative sample biases.   While the *dI/dV* spectrum reveals the clear signature of QWS at −0.45 V (albeit with smaller contrast), the oscillation in κ vs. V_s is now absent.   Instead, a monotonic decrease of κ is observed as the negative sample bias varies from low to high.   Nevertheless, above the location of

51

the highest occupied QWS (HOQWS), one observes a tapering of slope in the κ vs. V_s curve.
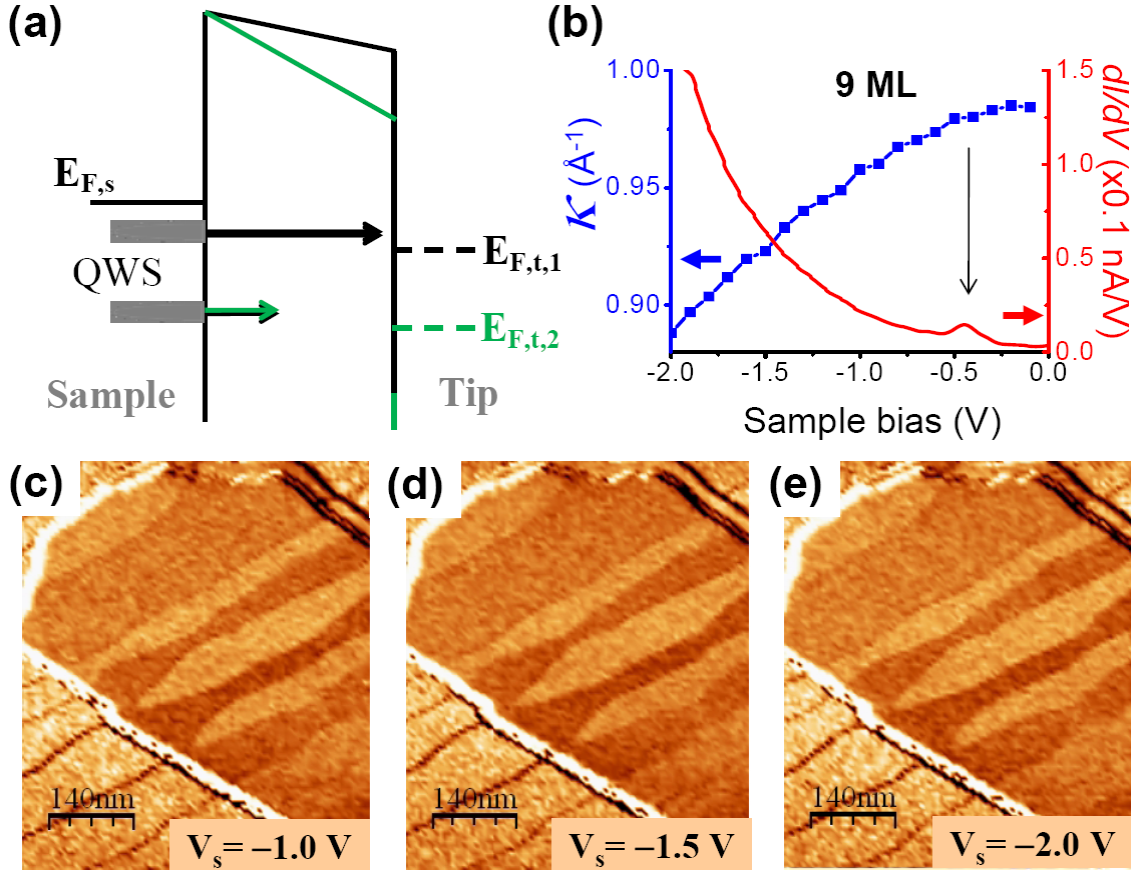
Figure 4.6: (a) A schematic illustration of the STM tunneling process when probing the sample filled states. $E_{F,s}$ and $E_{F,t}$ represent Fermi levels of the sample and tip, respectively. $E_{F,t,1}$ and $E_{F,t,2}$ show different energy levels of $E_{F,t}$ at two different applied biases. (b) Differential conductance spectra (red) and κ (blue) for 9ML. (c), (d), (e) Special mappings of κ taken at large negative biases: $V_s = -1.0$ V, -1.5 V, and -2.0 V respectively for the same island shown in Fig. 1(b).

The thickness-dependence of the tunneling decay constant (κ vs. L) continues to exhibit quantum oscillations. This can be seen in the spatial imaging of the tunneling decay constant, κ, shown in Fig. 4.6(c)-(e). Most interestingly, here the contrast of

spatial imaging of κ remains *identical*, as long as $V_s < -0.5$ V (namely, the tip Fermi level is below the HOQWS). This can be seen in the middle panel of Fig. 4.7(a), in contrast to empty state κ *vs.* L behavior where the phase of the oscillation changes drastically at different biases (upper panel of Fig. 4.7(a)). In fact, for $V_s < -0.5$ V, κ *vs.* L is *anti-correlated* with the location of the HOQWS (red dots in Fig. 4.7(b)): that is to say, the closer the HOQWS is to $E_{F,s}$, the lower the measured value of κ (with an exception at 10 ML). This can be easily understood as we discussed above: at a negative sample bias, whenever $E_{F,t}$ is below the HOQWS, the tunneling process is dominated by this HOQWS, regardless of the presence of other occupied QWS, thus determining the effective barrier height measurements. Such an anti-phase relationship between κ and HOQWS for Pb (111) thin films indeed was reported previously, but was wrongly understood as direct evidence for the QSE on the work function [13,16].

At the bias between 0 and -0.5 V, κ *vs.* V_s deviates from the above behavior. When the negative sample bias is decreased toward zero, the κ *vs.* L oscillation continues to undergo a profound phase change (lower panel of Fig. 4.7(a)), especially in the cross-over region (shaded region in Fig. 4.7(a)). The question that arises is whether any of these measurements tells us about the work function.

4.4.3 Very low bias regime (-0.03 V $< V_s < 0.03$ V)

Within the one-particle picture, the work function of the metal can be defined as the energy difference between the Fermi level and the vacuum level. This definition suggests that one should use the measurements performed at the bias voltage close to zero since only then are the states near E_F being probed. Moreover, at such very low bias, the results from filled-state and empty-state measurements should be consistent, and this is indeed what we observed (top panel of Fig. 4.7(c)). This result would suggest that the

53

measurements of the effective barrier height at very low bias range reflect the true QSE on the work function in these ultra-thin films.

According to theoretical calculation using a jellium model [17] with thickness varied continuously, the Fermi level with respect to the vacuum level varies as a function of film thickness. This is due to the variation of the depth of the "effective potential," which is in turn determined by the number of subbands occupied by the quantized electrons in the film. As the thickness of the film increases, new subbands get occupied one by one. Whenever a new subband becomes occupied at a particular thickness, the theoretical work function, being a function of a continuous thickness variable, exhibits a cusp right at the thickness where a new subband crosses the Fermi level [17,18]. In reality, the film thickness is not continuous but quantized and the corresponding work function should take the discretized value. So far all theoretical calculations of the L-dependent work function of Pb (111) surface are carried out only for free standing film, and thus cannot be compared directly with our measurements. However, the underlying principle that the QSE on work function is due to the QWS crossing the Fermi level should remain valid. Here the QWS locations as a function of thickness are directly measured. By using these data points, we can interpolate the locations in L (as a continuous variable) where the QWS channels cross the Fermi level (see the crossings of the black dashed curves with the blue dashed horizontal line in Fig. 4.7(b)). Using these crossing points, the period and phase of the oscillating work function as a function of continuous variable L are determined.
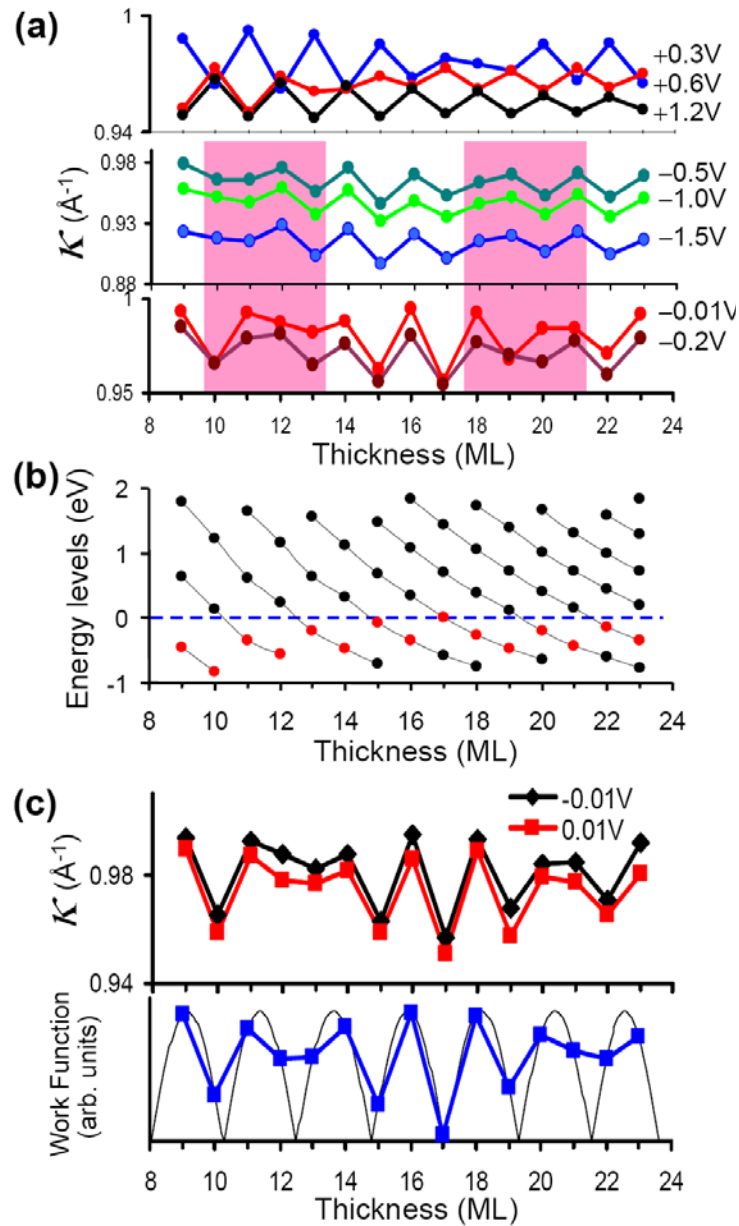
Figure 4.7: (a) Measured κ as a function of Pb thickness with various sample biases for 9-23 ML. (b) The locations of QWS obtained from the peak positions in *dI/dV* spectra. The horizontal dashed line at 0 eV is a guided line for the Fermi level. The red dots represent the highest occupied QWS for each thickness and the black dashed curves indicate a series of energy sub-bands. (c) Comparison between measured κ at ±0.01 V (upper part) and the work function simulation (lower part). The thickness dependence of the work function is well reflected on measurements of κ *vs*. L at ±0.01 V.

55

The calculated continuous curve is shown in the lower panel of Fig. 4.7(c), while blue square points on the calculated curve indicate discrete thickness values. It is evident in Fig. 4.7(c) that the behavior of the measured κ at low biases of ± 0.01 V indeed agrees with theoretical simulation based on the principle of Fermi level crossing of QWS channels. 17ML is expected to show the lowest work function value, because one of its QWS is located exactly at the point where the subband crosses the Fermi energy level, as shown in Fig. 4.7(b).

The consistent result of experimentally measured κ vs. L at $V_s \rightarrow 0$ with the expected work function oscillations predicted based on the Fermi level crossing of QWS (Fig. 4.7(c)) further confirms that such measurements indeed truthfully reflect the QSE of work function in ultra-thin films.

4.5 SUMMARY

It should be emphasized that the underlying physics of the bilayer oscillations in κ at ± 0.01 V and κ at large negative or positive biases are due to totally different origins. The oscillation of κ vs. L measured at a large negative bias and its anti-phase relation to the HOQWS are direct consequences of how QWS influence the tunneling process and do not involve work function oscillation. Similarly the rich behavior of κ measured at a positive bias as a function of L and V_s is also a direct manifestation of QWS in the tunneling process. Only when κ is probed at very low sample bias ($|V_s| < 0.03$ V) does the result truthfully reflect quantum oscillations of work function vs. layer thickness.

Chapter 5: Influence of quantum well states on the formation of AuPb surface alloy in Pb/Si(111)

5.1 INTRODUCTION

The thickness dependence of Au/Pb alloy formation on thin Pb quantum films is studied using *in-situ* low temperature STM/S.   Sub-monolayer Au is deposited onto thin Pb films on Si(111) substrates.   For this Au on Pb system, there are a few interesting issues.   It is known that for the bulk Pb system, Au can easily form a bi-metallic alloy with Pb.   Then, if the sub-monolayer Au can form a surface alloy on top of Pb mesa, how does the QWS of the underlying Pb influence the formation of AuPb surface alloys? Also, how does this system evolve with annealing?   Eventually, these questions are related to the role of QWS on the competition between thermodynamic and kinetic processes.   Our motivation starts from these questions.

When Au deposition is carried out at low temperature (~ 100K), it is found that nano-islands with moiré patterns form on top of Pb mesas.   With annealing up to ~ 150K, these moiré islands are transformed into three different types of Au/Pb surface alloys.   Each type of alloy shows unique electronic properties and can be clearly identified by STS.   Interestingly, the formation of these alloys is directly related to the QWS of underlying Pb films.   For thinner films of underlying Pb (below 12ML), it is also observed that the alloy formation probability has a strong thickness preference.

5.2 EXPERIMENT

The experiments are conducted in a home-built low temperature STM system with an *in-situ* sample preparation chamber.   Pb is deposited onto atomically clean Si(111) 7×7 surfaces at room temperature with a flux rate of 0.5 ML/min by using a

thermal evaporation technique, which results in a flat top mesa structure of Pb on Si(111) (see figure 5.1(a)) [20]. The room temperature growth of Pb leads to the formation of (111)-oriented 2D flat-top mesas on the stepped region, which is ideal for STM to investigate any thickness dependence since one mesa contains regions of different thicknesses. Then, we deposit 0.2ML Au on top of Pb mesa islands at low temperature (~ 100K), and while transferring the sample into the STM stage (takes ~ 3 min), sample temperature goes up to ~ 150K. All STM measurements are done at either 80K or 4.3K.
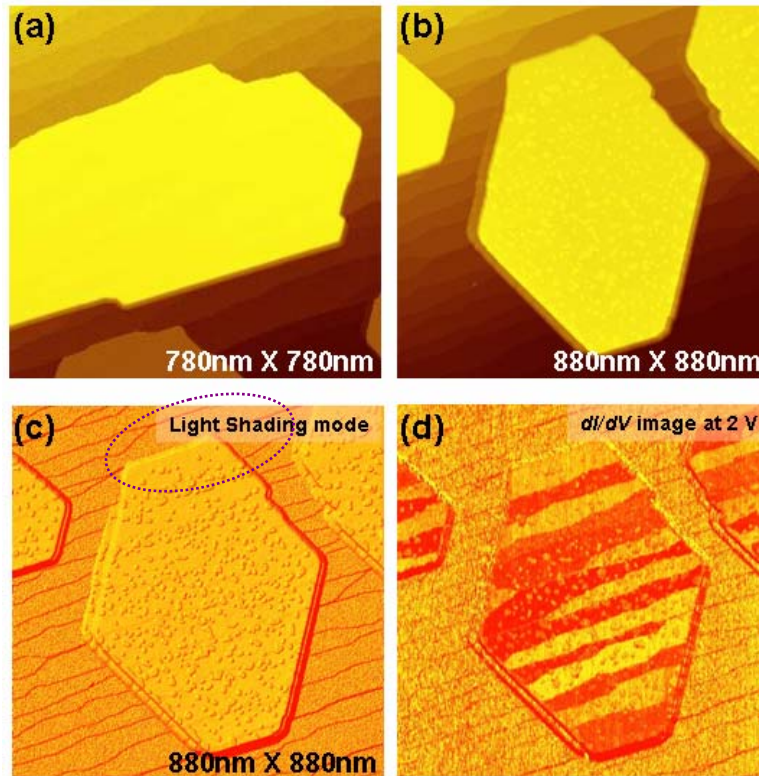
Figure 5.1: (a) Before and (b) after depositing 0.2ML Au on top of Pb mesa. (c) So-called light shading mode of (b). (d) Simultaneously taken differential conductance image at 2 V.

After Au deposition, the surfaces of Pb mesas are covered by small 2D islands, as shown in figure 5.1(b) and (c). In the *dI/dV* image of figure 5.1(d), each layer shows different

contrast due to the bilayer oscillation nature of QWS and the thickness boundary can be easily found from the contrast change. The overall distribution of these tiny islands on the surface looks uniform, except the circled area in figure 5.1(a) which is the thinnest region of the mesa. Zooming into the circled area (figure 5.2(a)), it is found that the 2D islands have a thickness preference on 10ML and 12ML. From the QWS data of figure 5.2(c), 10ML and 12ML are quantum unstable thickness because they have QWS relatively far away from the Fermi energy level (see section 4.1).
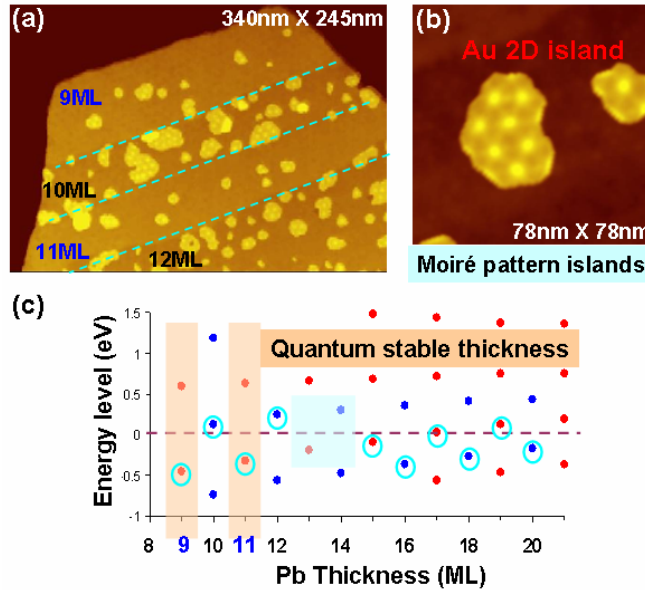
Figure 5.2: (a) Zoom-in STM image of figure 5.1(b). (b) Moiré pattern islands. (c) The energy locations of QWS as a function of Pb thickness.

In addition, all of these 2D islands have identical moiré patterns as shown in figure 5.2(b). Since the sample is kept at low temperature during preparation and all STM measurements are done at either 80K or 4.3K, we believe that the 2D islands are Au 2D islands, and their moiré pattern is due to a small lattice mismatch between Au and Pb. The amplitude of the bilayer oscillation of QWS near the Fermi energy becomes bigger as the Pb film gets thinner. This is why quantum size effects are always more

59

significant on thinner films, and might explain why the thickness preference of moiré islands can be observed only in the thinner layers.

5.3 RESULT AND DISCUSSION

As discussed above, Au deposited at low temperature forms a 2D island structure with moiré patterns on top of Pb mesas. It will be interesting to see how this system evolves with annealing. The result of 10 minutes of annealing (sample temperature will go up to ~ 170K) is presented in figure 5.3. New types of 2D islands without moiré patterns are observed on the surface, while the number of moiré pattern islands is significantly reduced (figure 5.3(c)). It seems that the moiré pattern islands are transformed into other types of larger 2D islands during annealing.

5.3.1 Type A and B islands

Interestingly, these new 2D islands can be classified into two different types based on *dI/dV* spectra taken on top of each 2D islands. First, from the *dI/dV* spectra of figure 5.3(e), the island (1) sitting on 10ML Pb reveals an exactly identical QWS to 11ML Pb, indicating that the island looks just like 1ML Pb in terms of *dI/dV* spectra. We name this island type A, and it can be found on the unstable thickness of 10ML and 12ML. On the other hand, the island (2), named type B, presents a totally different behavior in its *dI/dV* spectrum; i.e. it doesn't show well-defined QWS, as seen in figure 5.3(f), and the damped QWS looks somewhat closer to the underlying Pb. The type B island is observed on 13ML, which is a cross-over thickness.
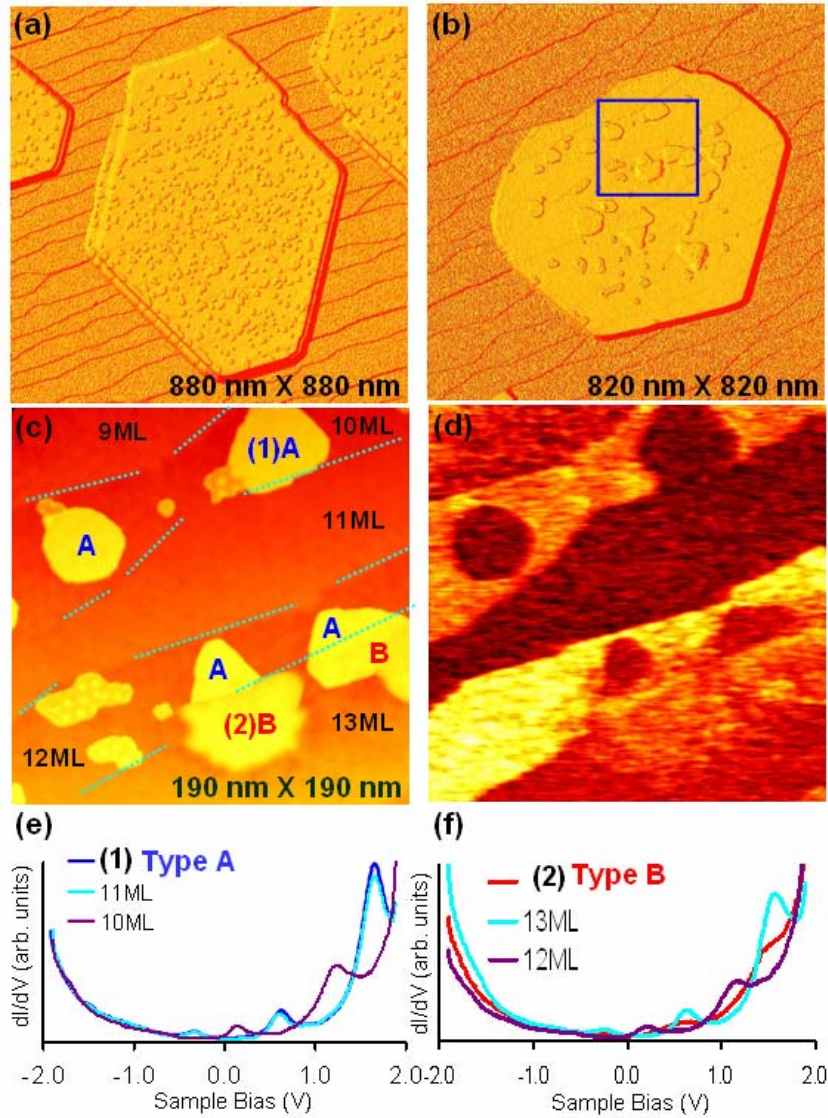
Figure 5.3: Type A and B islands are found after 10 minutes anneals (up to ~ 170K). (a) and (b) are STM light shading images before and after annealing, respectively. (c) Zoom-in image of the square area in (b). (d) *dI/dV* image of (c) taken at 2 V. (e) and (f) are individual *dI/dV* spectrum of the island (1) and (2), respectively.

The difference between type A and B becomes distinctive from the conductance image taken at 2 V (figure 5.3(d)) as only type A island has the contrast reversed against its underlying Pb. Figure 5.4 shows that an island is located at the boundary of 9ML and 10ML. The upper part of the island shows a damped QWS feature (a characteristic

61

of type B), while the QWS of lower part is identical to 11ML (a characteristic of type A). Moreover, it seems that the boundary of type A and B precisely follows the thickness boundary. The QWS of underlying Pb appears to be responsible for the formation of type A and B islands. It is very intriguing that the QWS are strong enough to separate the phase of its over-layer into two different partitions. Type A islands are always found at unstable thickness, and it behaves just like 1ML Pb so that the island itself forms stable QWS. In the case of type B, its vertical confinement seems to be quite disturbed, which gives rise to significantly depressed QWS. In this regard, we speculate that type A is 1ML of a pure Pb island and type B is a AuPb surface alloy. This point will be discussed again with our suggested model.
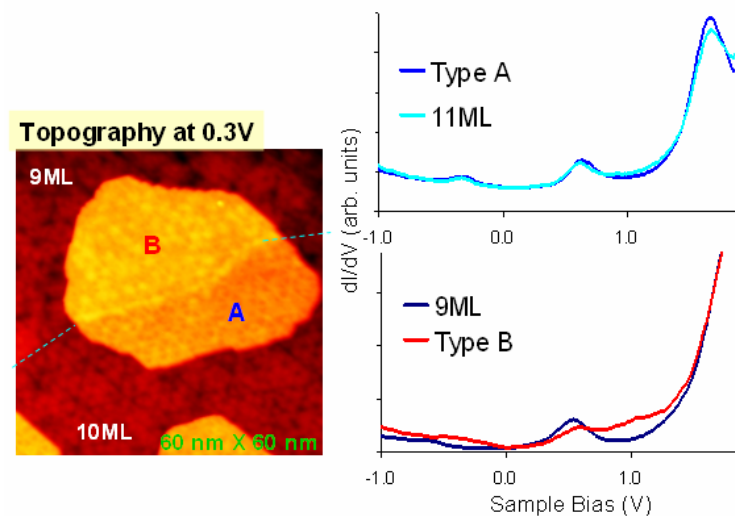
Figure 5.4: 2D island standing on the boundary of 9ML and 10ML Pb films.

5.3.2 Type M island

We have also found another type of island which is a mixture of type A and B shown in figure 5.5, and named it type M. Unlike the island of figure 5.4 whose separation of phase A and B is caused by its underlying QWS, this type M island is located at the same thickness of underlying Pb (13ML). Figure 5.5(c) shows *dI/dV*

spectra taken from the marked locations in figure 5.5(a). Interestingly, two different phases of type A (location (2)) and B (location (1)) coexists in a single island; i.e. position (2) has QWS identical to 14ML, while damped QWS are measured at position (1) and its energy location is measured to be very close to 13ML. The coexistence of type A and B can be observed from contrast changes in the conductance image.
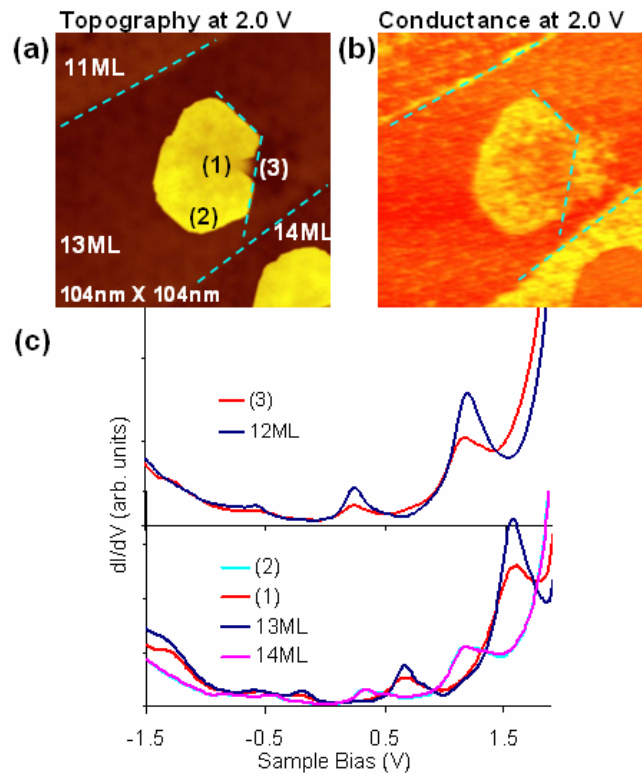
Figure 5.5: (a) STM image and (b) conductance image of type M island. (c) Individual *dI/dV* spectra are taken from the location marked in (a).

It should also be noticed that local DOS at location (3), supposedly 13ML Pb, looks very different from other 13ML surfaces in figure 5.5(b). Actually, the island edge between (1) and (3) is blunt (see figure 5.6), and it seems that something from the type M island diffuses into area (3), resulting in an altered QWS in the area. From the *dI/dV* spectrum

shown in figure 5.5(c), location (3) contains the characteristic type B island; i.e. its damped QWS energy location matches with 12ML QWS. We call it type B* to avoid confusion with the previously defined type B island, and in terms of QWS, its effective thickness is reduced by 1ML, suggesting that the type B* area consumes 1ML Pb on the mesa surface.
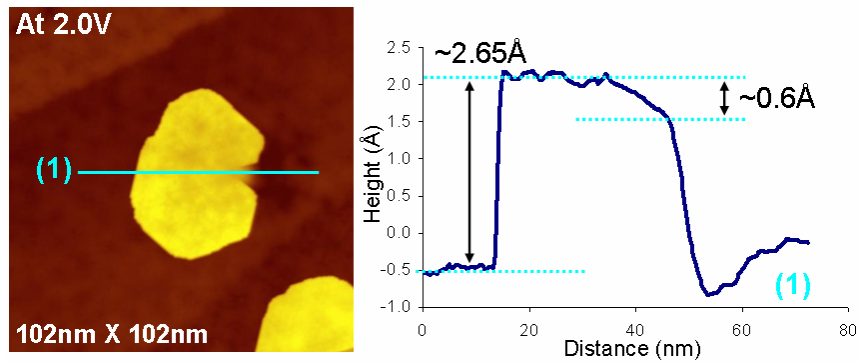
Figure 5.6: A line profile of type M island.

The superconducting gaps are also measured for the locations given in figure 5.5(a). Just like its typical behavior in QWS spectrum, type A can be treated as 1ML Pb in superconducting gap spectrum. However, in the case of type B, a clear gap spectrum is measured in the area of (1) and (3), although its QWS is always significantly depressed. This implies that the lateral superconducting coherence is still robust, while the vertical confinement weakens. This robustness of superconductivity will be discussed in next chapter.
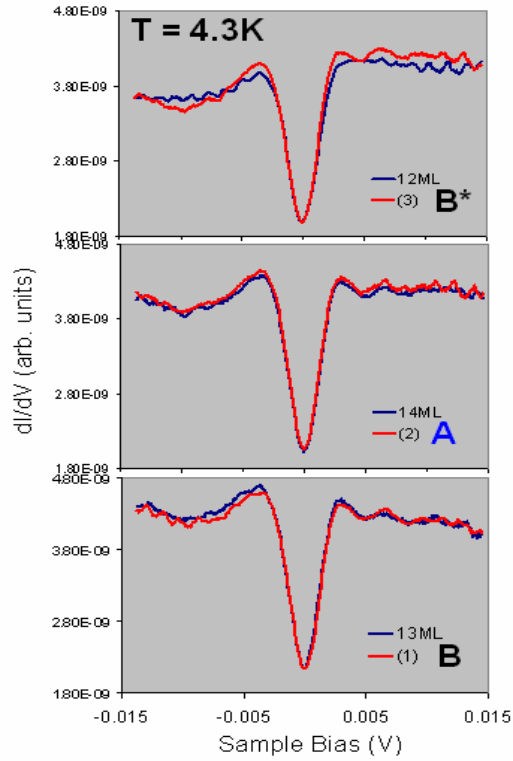
Figure 5.7: The *dI/dV* spectra used to measure the superconducting gap at the given locations in figure 5.5(a).

5.3.3 Model suggestion

So far, we have shown three different islands of type A, B, and M, and these types can be clearly identified by their QWS behavior in *dI/dV* spectra. Based on the type M island shown in figure 5.5, our model suggestion is presented in the illustration of figure 5.8. We suggest that type A is just 1ML Pb, otherwise its *dI/dV* spectrum will not show such a perfect agreement with the QWS of one layer thicker Pb. Since all these types are found only after annealing, it is expected to find AuPb surface alloy, and type B island is the most appropriate candidate for a surface alloy. If the interface between a type B overlayer and underlying Pb mesa is not well defined or is very rough, it may

result in losing the coherence of vertical confinement. Then, it is possible to show depressed QWS of the underlying Pb. In the case of type B*, some Au particles from nearby type B island might diffuse into the Pb mesa surface and form type B alloy by consuming 1ML Pb. Therefore, its QWS should be damped and its effective thickness in forming QWS should be reduced by 1ML.
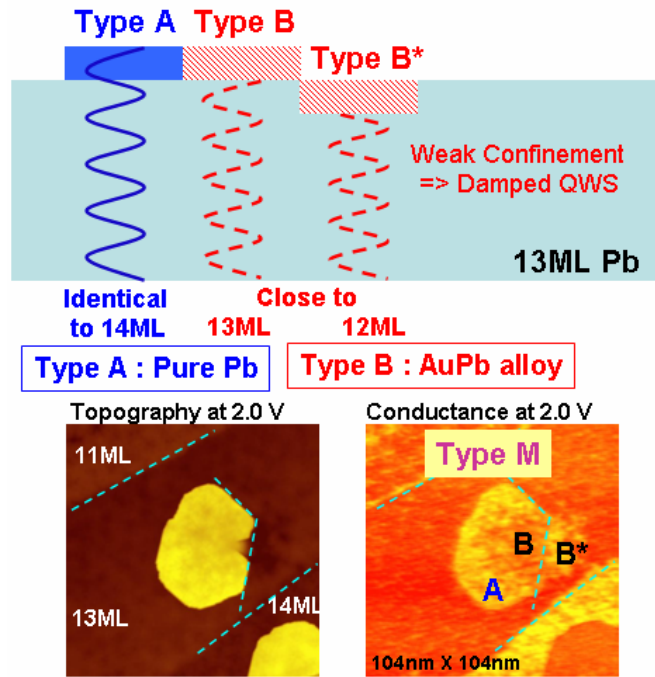
Figure 5.8: A schematic illustration to understand type A, B, and M islands.

5.4 SUMMARY

Immediately following low temperature deposition of sub-monolayer Au on top of Pb mesa, the surface of Pb mesas is covered by 2D Au islands with moiré patterns. It is observed that these Au islands prefer to form on region of quantum unstable thicknesses on the thinner part (below 13ML) of the mesa (figure 5.9(a)). Then, this

system undergoes dramatic change during annealing up to ~ 170K. The number of moiré pattern islands (Au islands) is significantly reduced while other types of islands such as type A, B, and M form, indicating that the Au islands are transformed into other types, including AuPb surface alloy during annealing. From figure 5.9(b), strong thickness preference on island formation is observed in the thinner part of Pb mesa; i.e. the thicknesses of 9ML and 11ML are so energetically stable, that they are making it highly unfavorable to have any overlayer. Based on tunneling spectroscopy results, type A islands are most likely Pb 2D island with 1ML height, and it can be found on unstable thicknesses. Then, type A islands form stable thickness, which makes sense energetically. Type B islands are considered AuPb surface alloys formed on stable (or cross-over) thicknesses. Since the AuPb alloy forms on stable layers, it "tries" to keep QWS of the underlying Pb rather than form a QWS of the unstable thickness. Its damped QWS feature could be due to a very rough interface between the AuPb island and mesa surface. Lastly, type M islands are usually observed in cross-over regions, and they consist of two different phases of type A and B. Since the cross-over region is energetically between stable and unstable points, it makes sense that this mixed phase island can often be found in the cross-over thicknesses of 13ML and 14ML. A clue to Au diffusion into the Pb surface is also observed in the nearby area of type M island. Further annealing up to ~ 250K does not change the overall distribution of type A and B islands in contrast to Au (moiré pattern) and type M islands that almost disappeared in figure 5.9(c). Thus, type A and B islands are reasonably robust under annealing.
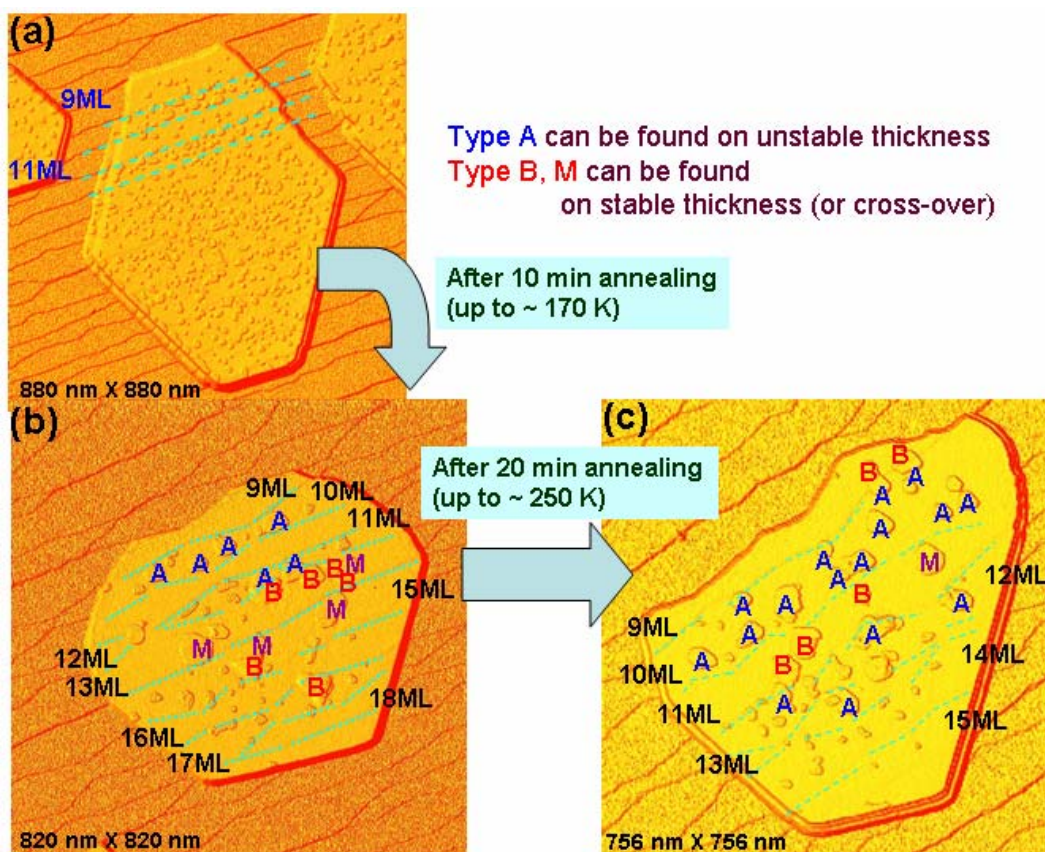
Figure 5.9: Light shading STM images of Au/Pb system before and after annealing.

Chapter 6:   Towards the Zero-dimensional Limit of Superconductivity

6.1 BCS THEORY

Since superconductivity was discovered by Onnes in 1911 [32], great efforts have been devoted to better understand superconductivity.   The first microscopic explanation of it was proposed by Bardeen, Cooper, and Schrieffer in 1957 and is known as the celebrated Bardeen-Cooper-Schrieffer (BCS) theory of superconductors [33].   In this section, the basic concept of this theory will be discussed.

6.1.1 Cooper pairs and the BCS ground state

The term Cooper pair is named after Leon Cooper who first suggested that two electrons can be bound together at low temperatures in a superconductor [34].   The basic idea of Cooper pairs is that even a very small attractive interaction can create a paired state of electrons that have a lower energy than the Fermi energy, implying that the pair is bound.   This must have been a very striking model 50 years ago because electrons have a repulsive Coulomb interaction in free space, as well as in solid state system.   In this section, the details of Cooper pairs will be discussed.

We introduce two electrons to just above a Fermi sea ($k > k_F$) at a temperature T = 0 K and assume they have no interaction with electrons in the sea.   In order to describe two electrons with equal and opposite momentum, the Schrödinger equation can be expressed as

$$-\frac{\hbar^2}{2m}\left(\nabla_1^2 + \nabla_2^2\right)\psi_0 + V(r_1, r_2)\psi_0 = E\psi_0, \text{ and } \psi_0(r_1, r_2) = \sum_k g_k e^{ik\cdot r_1} e^{-ik\cdot r_2} . \qquad (6.1)$$

[gk, r1, r2, grad1, grad2 not defined] By using relative coordinates $r_1 - r_2 = r$ and a two-electron singlet wave function, ψ_0 becomes

$$\psi_0(r_1 - r_2) = \left[\sum_{k>k_F} g_k \cos k \cdot (r_1 - r_2)\right](\alpha_1\beta_2 - \beta_1\alpha_2). \tag{6.2}$$

Using eq. (6.2) and taking $\int \cos k' \cdot r dr$ for both sides of the Schrödinger equation, we can get

$$2\frac{\hbar^2 k'^2}{2m} g_{k'} + \sum_{k'>k_F} g_k V_{kk'} = E g_{k'}, \text{ and } V_{kk'} = \frac{1}{\Omega}\int V(r_1, r_2)\cos(k \cdot r)\cos(k' \cdot r)dr \tag{6.3}$$

$$(E - 2\varepsilon_{k'})g_k = \sum_{k'>k_F} g_k V_{kk'}, \text{ and } \varepsilon_{k'} = \frac{\hbar^2 k'^2}{2m}, \tag{6.4}$$

where ε_k are the unperturbed plane-wave energies, $V_{kk'}$ are the matrix elements of the interaction potential, and Ω is the normalization volume. Solving for $V_{kk'}$ is a very complicated problem. However, thanks to his excellent intuition, Cooper was able to make a very bold assumption in order to avoid calculating for $V_{kk'}$ directly:

$$V_{kk'} = \begin{cases} -V & \varepsilon_F < \varepsilon_k < \varepsilon_F + \hbar\omega_c \\ 0 & \text{otherwise} \end{cases}. \tag{6.5}$$

Eq. (6.4) then becomes

$$\begin{aligned}
\frac{1}{V} &= \sum_{k>k_F} \frac{1}{2\varepsilon_k - E} = \sum_{k>k_F} \frac{1}{2(\varepsilon_k - E_F) + (2E_F - E)} \\
&= N(0)\int_{\varepsilon_F}^{\varepsilon_F + \hbar\omega_c} \frac{d\varepsilon}{2\varepsilon - E} = \frac{N(0)}{2}\ln\frac{2(\varepsilon_F + \hbar\omega_c) - E}{2\varepsilon_F - E},
\end{aligned} \tag{6.6}$$

where $N(0)$ is the density of states at the Fermi level for electrons of one spin orientation. In addition to the assumption (6.5), we can use the so-called weak-coupling

approximation: $N(0)V \ll 1$. This approximation[2] makes sense since $N(0)V < 0.3$ in most classic superconductors. We can determine the energy of two electrons,

$$E \approx 2E_F - 2\hbar\omega_c e^{-2/N(0)V} .$$ (6.7)

This surprising result tells us that as long as V is attractive, no matter how small it is, the energy of two electrons with a kinetic energy in excess of E_F (i.e. $k > k_F$) will fall inside the Fermi surface, implying a bound state. So, we know that even a weak attraction can bind pairs of electrons into a bound state with Cooper's assumption (6.5). However, we do not know where the attractive interaction comes from.

Pine used the Jellium model[3] to calculate the interaction term $V(\mathbf{q}, \omega)$ in momentum space [35];

$$V(q,\omega) = \frac{4\pi e^2}{q^2 + k_s^2} + \frac{4\pi e^2}{q^2 + k_s^2} \frac{\omega_q^2}{\omega^2 - \omega_q^2} .$$ (6.8)

The first term is basically a form of the Yukawa potential expressed in momentum space which implies the Coulomb repulsion under screening effects. The next term is the phonon mediated interaction, which is negative for $\omega < \omega_q$, and indicates that eventually it is physically possible for V to be negative (meaning an attraction). Also, this result provides another important piece information: the attractive interaction is possible only with a phonon contribution[4]. In 1950, Fröhlich suggested an important role of the electron-lattice interaction to explain superconductivity [36]. The idea can be described as a simple picture: a traveling electron will polarize the solid medium by attracting positive ions, and then these locally excess ions will attract another electron, resulting in an

---

[2] There are some materials which are strong coupling superconductors such as Pb and Nb.

[3] The Jellium model approximates the solid as a fluid of electrons and point ions, and completely neglects the crystal structure and Brillouin zone effects as well as of the finite ion-core size.

[4] Although the phonon-mediated attraction is the basis of classic superconductors, some superconductors, such as heavy fermions and high temperature superconductors, may have different pairing interactions involving the exchange of bosons other than phonons.

attractive interaction between the two electrons. If this attraction is strong enough to overcome the repulsive screened Coulomb interaction, it becomes a net attractive interaction, and eventually superconductivity occurs [37]. Since $V_{kk'}$ is responsible for the potential strength of scattering a pair of electrons with momenta (**k′, -k′**) to (**k, -k**), by momentum conservation the relevant phonon should carry momentum **q** = **k** - **k′**. Now, in eq. (6.8), ω_q should be the relevant phonon frequency. Then, it is not surprising that the cutoff energy of $\hbar\omega_c$ in Cooper's assumption (6.5) will be the order of the Debye energy $\hbar\omega_D = k\Theta_D$, which characterizes the cutoff of the phonon spectrum.

Historically, with the idea of Cooper pairs, there was a difficulty in finding the proper form of the ground state for Cooper pairs which should cover the order of Avogardo's number of electrons. For an N electrons system, the most general wavefunction incorporated with the Cooper pairs can be expressed as

$$|\psi_N\rangle = \sum g(k_i,...,k_l)c^+_{k_i\uparrow}c^+_{-k_i\downarrow}\cdots c^+_{k_l\uparrow}c^+_{-k_l\downarrow}|\phi_0\rangle, \tag{6.9}$$

where $|\phi_0\rangle$ is the vacuum state with no electrons and the $c^+_{k\uparrow}$ operator creates an electron of momentum **k** with spin up (so that $c^+_{k\uparrow}c^+_{-k\downarrow}$ creates one Cooper pair). However, there is a problem with this expression. There are $\sim 10^{(10^{20})}$ ways to choose N/2 possible states for pairing and one would need to handle a huge amount of terms in the sum of eq. (6.9) to solve any superconductivity problem. In order to circumvent this problem, we can assume that the occupancy of each state **k** is taken to depend solely on the average occupancy of other states. This is called the *mean-field* approach. BCS theory predicted the ground state to be

$$|\psi_G\rangle = \prod_{k=k_1,...k_M}(u_k + v_k c^+_{k\uparrow}c^+_{-k\downarrow})|\phi_0\rangle, \tag{6.10}$$

where $|u_k|^2 + |v_k|^2 = 1$. The pairing state of $(k\uparrow, -k\downarrow)$ will be occupied with a probability $|v_k|^2$, and unoccupied with a probability $|u_k|^2$. Eq. (6.10) is definitely simpler because it is expressed by only one parameter $\mathbf{k}$. Essentially, this can be treated as a grand canonical ensemble problem because the number of pairs $(\bar{N})$ with the given ground state (6.10) gives

$$\frac{\delta N_{rms}}{\bar{N}} \approx 10^{-13}, \text{ and } \delta N_{rms} \approx 10^9. \tag{6.11}$$

Although the absolute value of the fluctuation in the pairing number is quite big, its fractional fluctuation is small enough to use the grand canonical ensemble method.

6.1.2 Energy gap

To describe the Cooper pairs in superconductivity, the Hamiltonian can be written as

$$H = \sum_{k\sigma} \xi_k n_{k\sigma} - \sum_k (\Delta_k c_{k\uparrow}^+ c_{-k\downarrow}^+ + \Delta_k^* c_{-k\downarrow} c_{k\uparrow} - \Delta_k b_k^*), \quad b_k = <c_{-k\downarrow} c_{k\uparrow}> \tag{6.12}$$

$$\Delta_k = -\sum_l V_{kl} b_l = \sum_l V_{kl} <c_{-l\downarrow} c_{l\uparrow}>. \tag{6.13}$$

where $\xi_k = \varepsilon_k - \mu$ is the single-particle energy measured from the Fermi energy. It is not an easy task to solve eq. (6.12) because of the quartic terms in c_k. By defining new quasi particle Fermi operators γ_k and a new quasi particle energy E_k, the Hamiltonian (6.12) can be diagonalized in terms of γ_k and E_k [38,39]:

$$c_{k\uparrow} = u_k^* \gamma_{k\uparrow} + v_k \gamma_{-k\downarrow}^+, \text{ and } c_{-k\downarrow}^+ = -v_k^* \gamma_{k\uparrow} + u_k \gamma_{-k\downarrow}^+ \tag{6.14}$$

$$E_k = \sqrt{\xi_k^2 + \Delta_k^2} \tag{6.15}$$

$$H = \sum_k (\xi_k - E_k + \Delta_k b_k^*) + \sum_k E_k (\gamma_{k\uparrow}^+ \gamma_{k\downarrow} + \gamma_{-k\downarrow}^+ \gamma_{-k\uparrow}). \tag{6.16}$$

The diagonalized Hamiltonian (6.16) is obtained when u_k and v_k satisfy the following condition:

$$2\xi_k u_k v_k + \Delta_k^* v_k^2 - \Delta_k u_k^2 = 0. \tag{6.17}$$

As shown above, the pairing Hamiltonian (6.12) is transformed to the quasi particle Hamiltonian (6.16) by defining new Fermi operators. The first term in (6.16) indicates the condensation energy will vanish at the normal state as $E_k = \xi_k$ and $\Delta_k = 0$ for the normal state. The second term represents the increase of energy above the ground state in terms of quasi particle number operators $\gamma_k^+ \gamma$, i.e. the excitation energy of quasi particles. It is clear in eq. (6.16) that E_k defined in eq. (6.15) corresponds to the excitation energy of a fermion quasi particle of momentum $\hbar k$ while Δ_k is the minimum excitation energy or energy gap. Similarly, eq. (6.13) can be written in terms of quasi particle operators γ_k as

$$\Delta_k = -\sum_l V_{kl} < c_{-l\downarrow} c_{l\uparrow} > = \sum_l V_{kl} u_l^* u_l < 1 - \gamma_{l\uparrow}^+ \gamma_{l\uparrow} - \gamma_{-l\downarrow}^+ \gamma_{-l\downarrow} > . \tag{6.18}$$

$$|v_k|^2 = \frac{1}{2}\left(1 - \frac{\xi_k}{E_k}\right), \text{ and } |u_k|^2 = \frac{1}{2}\left(1 + \frac{\xi_k}{E_k}\right). \tag{6.19}$$

The coefficients v_k and u_k shown in (6.19) can be calculated from (6.17). Now, we introduce the BCS approximation for V_{kl} and Δ_k:

$$V_{kl} = -V \text{ for } |\xi_k| < \hbar\omega_c (V_{kl} = 0, \text{otherwise})$$
$$\Delta_k = \Delta \text{ for } |\xi_k| < \hbar\omega_c (\Delta_k = 0, \text{otherwise}) . \tag{6.20}$$

By using the Fermi distribution, the BCS approximation, and eq. (6.19), $\Delta(0)$ (Δ at T=0) can be found as shown below:

$$\Delta(0) \cong 2\hbar\omega_c e^{-\frac{1}{N(0)V}} . \tag{6.21}$$

For a more general form, the BCS approximation can be used to express eq. (6.18) as

74

$$\frac{1}{V} = \frac{1}{2}\sum_k \frac{\tanh(\beta E_k / 2)}{E_k} \Rightarrow \frac{1}{N(0)V} = \int_0^{\hbar\omega_c} \frac{\tanh\frac{1}{2}\beta(\xi^2 + \Delta(T)^2)^{1/2}}{(\xi^2 + \Delta(T)^2)^{1/2}} d\xi . \qquad (6.22)$$

As shown in eq. (6.21), Δ(T) can be calculated numerically. For weak-coupling superconductors ($\hbar\omega_c / kT_c \gg 1$), $\Delta(T)/\Delta(0)$ is a universal function of T/T_c as shown in figure 6.1.
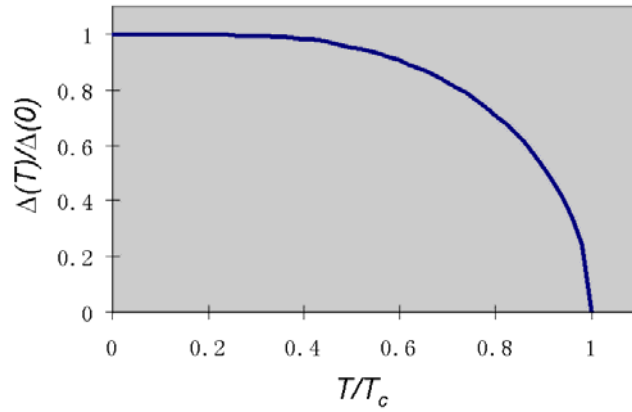
Figure 6.1: Temperature dependence of the energy gap in BCS theory

Since $E_k = |\xi_k|$ at T = T$_c$ (or at normal state), T$_c$ can be found by replacing E_k with $|\xi_k|$ in eq. (6.22):

$$T_c \cong \hbar\omega_c e^{-\frac{1}{N(0)V}} . \qquad (6.23)$$

Both T_c in eq. (6.23) and $\Delta(0)$ in eq. (6.21) show an exponential dependence of $N(0)$, the density of states at the Fermi level for electrons. Then, from eq. (6.21) and (6.23), we have the relation between T_c and $\Delta(0)$:

$$\frac{2\Delta(0)}{kT_c} = 3.54 . \qquad (6.24)$$

75

It should be noted that eq. (6.24) is valid only under the condition of the BCS approximation (6.20). This relation is often used to test if BCS theory works well in a certain superconductor.

6.1.3 The density of states and quasi particle tunneling

As shown in the previous section, the Fermi operator γ_k^+ describes the excitation of a quasi particle and has a one to one correspondence with c_k^+ of the normal state. Based on the one to one relation, the superconducting density of states can be expressed as

$$N_s(E)dE = N_n(\xi)d\xi . \tag{6.25}$$

We can treat $N_n(\xi)$ as a constant value $N(0)$ for a very small energy range of ξ. Then, from eq. (6.15),

$$\frac{N_s(E)}{N(0)} = \frac{d\xi}{dE} = \begin{cases} \dfrac{E}{\sqrt{E^2 - \Delta^2}} & (E > \Delta) \\ 0 & (E < \Delta) \end{cases} . \tag{6.26}$$

Indeed, the superconducting density of states has an energy gap Δ in eq. (6.26).

A typical experimental way to measure the density of states (or the energy gap) is the electron tunneling method. Then, for the superconductor-normal metal tunneling junction of figure 6.2, the proper tunneling Hamiltonian can be written as

$$H_T = \sum_{\sigma kq} (T_{kq} c_{k\sigma}^+ c_{q\sigma} + T_{kq}^* c_{q\sigma}^+ c_{k\sigma}) . \tag{6.27}$$
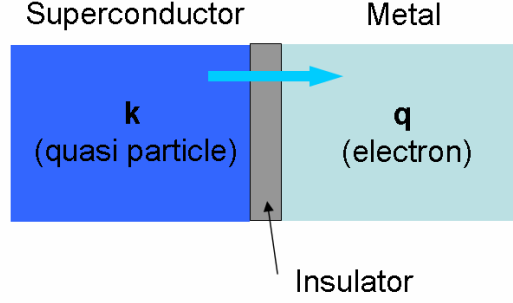
Figure 6.2: A schematic of the superconductor-metal tunneling junction

Then, with an applied bias V, the corresponding tunneling current I_{SN} is given by

$$I_{SN} = \frac{4\pi e}{\hbar}|T|^2 \int_{-\infty}^{\infty} N_s(E)N_q(E+eV)[f(E) - f(E+eV)]dE, \tag{6.28}$$

where the tunneling matrix $|T|^2$ can be calculated by using the tunneling Hamiltonian (6.27) and $|T_{kq}|^2 = |\langle k|H_T|q\rangle|^2$. From the superconducting density of states (6.26), eq. (6.28) reduces to

$$I_{SN} \propto \int_{-\infty}^{\infty} N_s(E)[f(E) - f(E+eV)]dE$$
$$\propto \int_{\Delta}^{\infty} \frac{E}{\sqrt{E^2 - \Delta^2}}[f(E) - f(E+eV)]dE \tag{6.29}.$$

The superconducting density of states can be measured by taking the differential conductance (dI_{SN}/dV) in an electron tunneling experiment:

$$\frac{dI_{SN}}{dV} \propto \int_{\Delta}^{\infty} \frac{E}{\sqrt{E^2 - \Delta^2}}\left[-\frac{df(E+eV)}{dE}\right]dE \xrightarrow{T=0} \frac{E}{\sqrt{E^2 - \Delta^2}} \ (E > \Delta). \tag{6.30}$$

Eq. (6.30) can be numerically integrated to obtain theoretical tunneling conductance spectra (or theoretical superconducting density of states) for different temperatures. An example of experimental differential conductance data is given in figure 6.3.
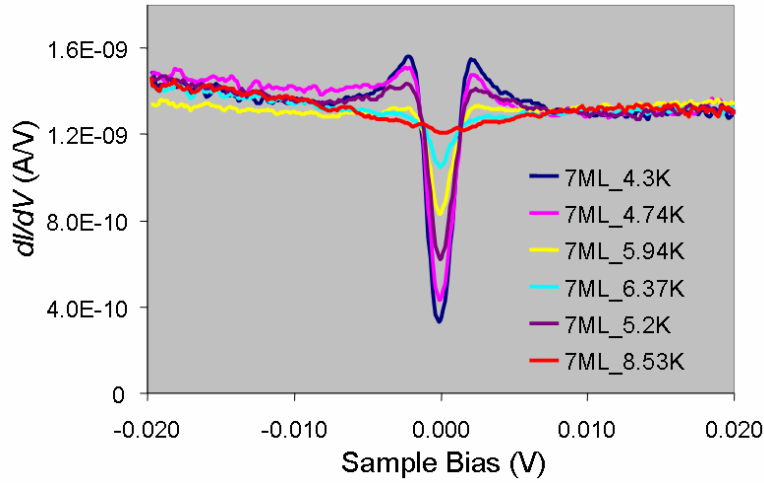
Figure 6.3: *dI/dV* spectra taken from Pb 7ML films for different temperatures.

6.1.4 Determination of T_c

The superconducting transition temperature (T_c) is one of the most important pieces of information in superconductivity studies because it is related to various physical properties of superconductivity such as the superconducting coherence length and the energy gap. However, a precise determination of T_c is not trivial in a tunneling experiment unless one can control the sample temperature continuously until the gap is completely gone. One way to determine a reliable T_c is by fitting experimental data with the results of BCS theory.

Since we know the theoretical density of states (DOS) from BCS theory, experimental *dI/dV* spectra can be fitted to the BCS DOS (from eq. (6.30)) to obtain the energy gap (Δ) for each temperature. Figure 6.4 presents an example of this BCS - experimental *dI/dV* fitting from the data shown in figure 6.3.

78
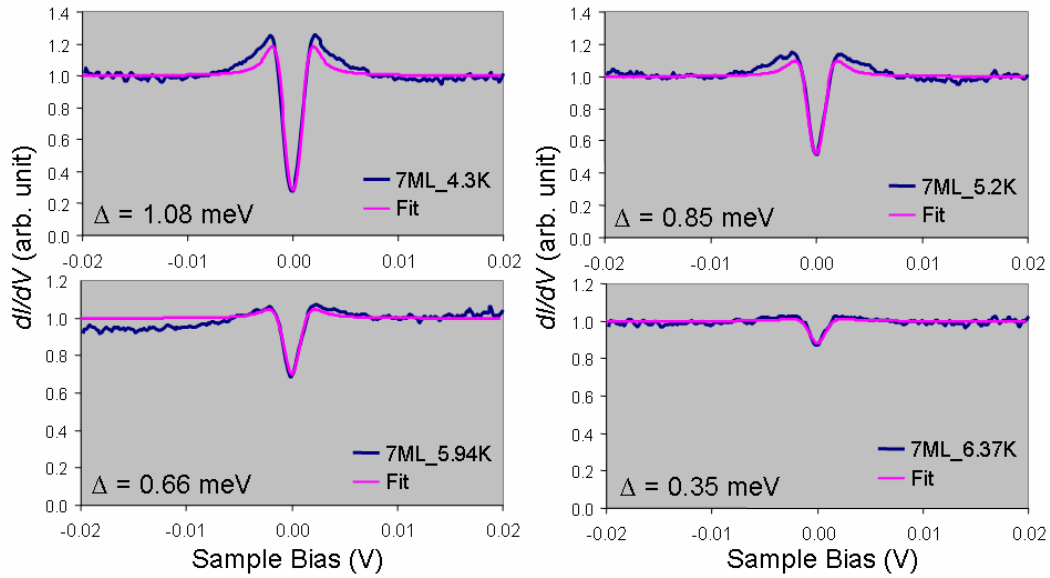
Figure 6.4: The experimental *dI/dV* spectra are fitted with BCS DOS to extract the energy gap (Δ) value for each temperature.

In order to find T_c, the extracted energy gap values (Δ*(T)*) are again fitted with the theoretical Δ*(T)* curve from eq. (6.22) and figure 6.1. The result is shown in figure 6.5. T_c for a 7ML Pb film is determined to be around 6.57 K from $T = T_c$ at Δ = 0[5].
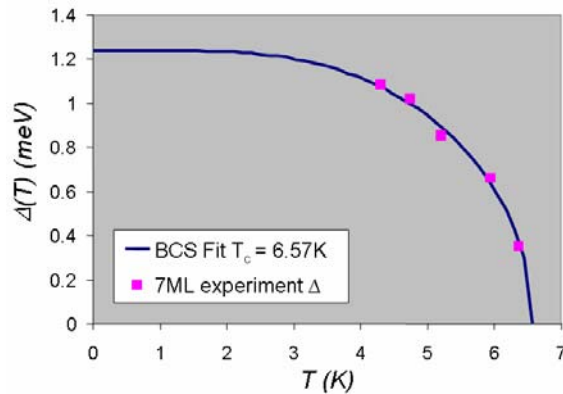
Figure 6.5: The experimental Δ*(T)* is fitted by using the BCS gap equation.

---

[5] The individual *dI/dV* spectrum fitting with BCS DOS and experimental Δ*(T)* fitting with the BCS gap equation are done by using the analysis software made by Dr. Daejin Eom. Detailed information of the software can be found in his Ph.D. dissertation in the library of the University of Texas at Austin.

As already mentioned in the previous section, the BCS gap equation (6.22) gives rise to $\Delta(T)$ as a universal function of T under the assumption of weak-coupling superconductors. Although the fitting in figure 6.5 shows an excellent agreement, strictly speaking, the BCS gap equation used in the fitting is not valid in this case because Pb is the strong-coupling superconductor. Even for strong-coupling superconductors, however, the behavior of $\Delta(T)$ near T_c is well described by the BCS gap equation. Therefore, the T_c value determined by using our fitting method should not be very different from the real T_c because experimental $\Delta(T)$ values near T_c will eventually determine the T_c in the fitting.

6.2 LOW-DIMENSIONAL SUPERCONDUCTIVITY

The fate of superconductivity in systems with spatial dimensions smaller than the coherence length, ξ, has been the subject of intense interest for decades[24,40-57]. Recent studies of superconductivity in ultra-thin epitaxial metal films have revealed that superconductivity remains robust in thin Pb films with thicknesses orders of magnitude smaller than ξ[24,42,46]. What happens if all dimensions are reduced? We systematically address this fundamental question via a detailed scanning tunneling microscopy/spectroscopy (STM/STS) study of thin-film superconducting islands with different thicknesses and lateral sizes. We find that the suppression of the superconducting gap Δ with size depends to a good approximation only on the volume of the island and is largely independent of its shape. We also report data showing superconducting proximity effects between nano-islands with different thicknesses. Our results reveal the systematic breakdown of superconductivity in nanostructures, and have important implications for thin film, heterostructure, and nanoscale superconducting device implementation.

6.2.1 Introduction
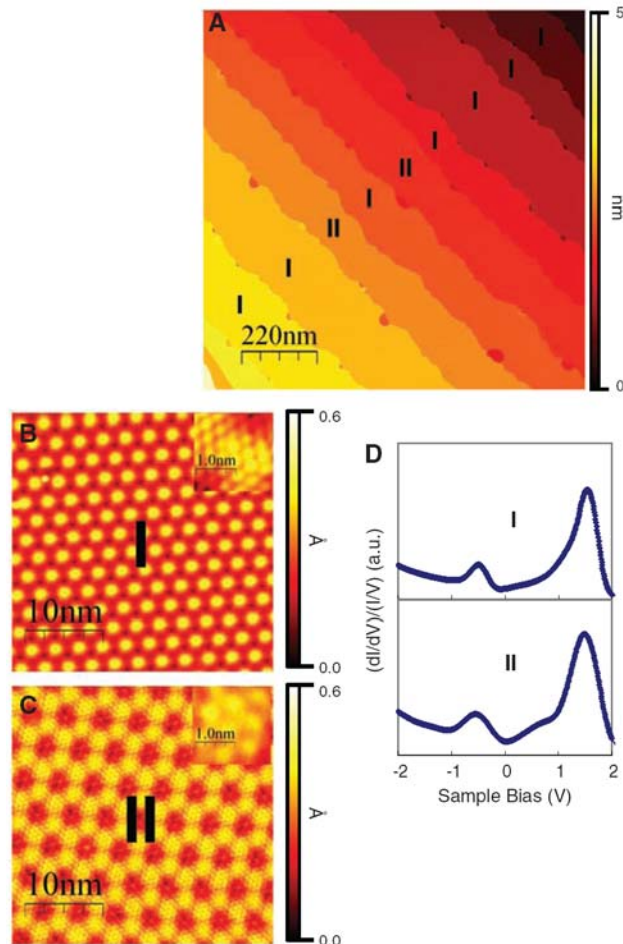
Figure 6.6: STM topography images and *dI/dV* spectra of 2ML Pb films.

For a long time, we have been trying to answer the question, "How thin can superconducting materials be without losing their superconductivity?" In order to maintain superconductivity in the two-dimensional limit, the Cooper pairs should overcome many obstacles, created by low-dimensional geometries such as rigorous scattering at the boundary of superconductor, thermodynamic fluctuations, and proximity

effects. In this sense, to answer the question, we may need a deep understanding about the coherence and robustness of electron pairing in a superconductor. Recently, we have succeeded in preparing two-atom-thick, or two mono-layer (2ML), Pb films on a $\sqrt{3} \times \sqrt{3}$ PbSi template modified from a Si(111) surface (see section 6.2.2)[24]. Figure 6.6(b) and (c) show that in 2ML Pb films, two atomic structures of 1×1 and $\sqrt{3} \times \sqrt{3}$ are found, which are called "type I" and "type II"[6], respectively. It turns out that there is only one allowed QWS in the filled states of 2ML Pb films, indicating that such an extreme 2D geometry creates an ideal 2D electron gas system (see figure 6.6(d)).

As shown in figure 6.7, both types are superconducting with T_c = 4.9K and 3.8K for type I and type II structures, respectively. It is surprising that superconductivity can be established in a single 2D subband channel. This result raises an important question about the origin of the robustness of superconductivity, and we may need better understanding of superconducting coherence to answer this question. There is another intriguing question in this subject: in such an extreme 2D geometry, how does the superconductivity change as the lateral dimension collapses into the zero-dimensional limit?
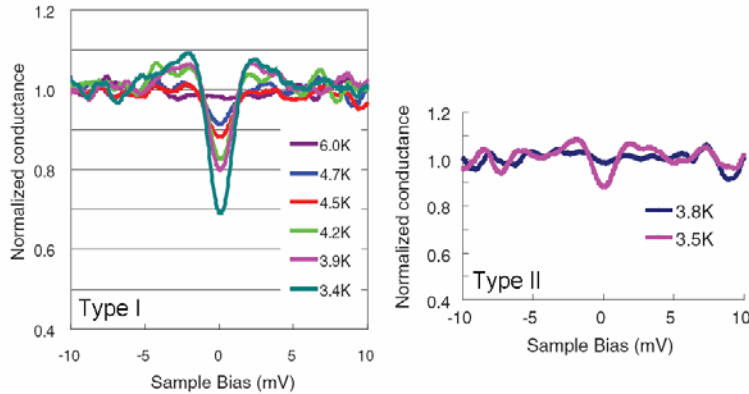
Figure 6.7: *dI/dV* spectra for type I and type II 2ML Pb films.

---

[6] It should be mentioned that they are not meant to be the conventional type I/II superconductor.

6.2.2 Two-dimensional Pb island growth

Depending on the growth conditions, various kinds of Pb samples can be prepared from a globally flat film to a 2D island as small as ~ 15 nm when Pb is deposited on the surface of Si(111) 7×7 reconstruction (Pb/Si(111)). It is known for Pb/Si(111) that Pb always grows along its preferred growth direction [111], regardless of its morphology. There are two critical growth parameters which influence the sample morphology significantly: the growth temperature and interface between Pb and Si(111). Figure 6.8(a) shows a globally flat film of 5ML Pb on Si(111) which is slowly annealed to room temperature after low temperature growth (~ 100K), while the other STM image (b) shows a flat top mesa of Pb prepared at room temperature. In the case of low temperature growth, only those Pb films with quantum stable thicknesses can be prepared (see section 4.1 for details).
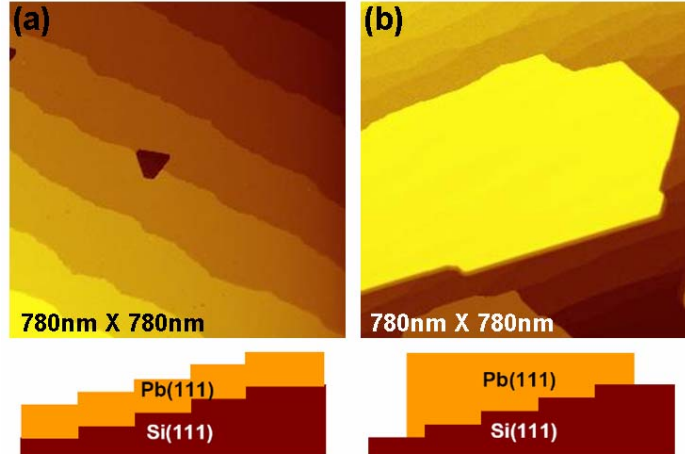
Figure 6.8: STM topography images of Pb/Si(111) for a globally flat film (5ML) and a flat top mesa prepared at (a) low temperature (~100K) and (b) room temperature, respectively.

When ultra-thin Pb films (< 5 ML) are required, cooling down the sample temperature is not enough to have the globally flat morphology due to the structural

mismatch between Pb(111) and Si(111) surfaces. In addition to the growth temperature, the interface energy plays an important role in thin film growth, and is dependent on the strain between the film and substrate. For Pb/Si(111) system, the interface energy can be reduced to be favorable for flat film growth by modifying the surface reconstruction of Si(111) 7×7. In fact, with Pb-Si $\sqrt{3} \times \sqrt{3}$ reconstruction on Si(111) surface, nice flat Pb films can be prepared even down to 2ML thickness under low temperature deposition (~ 100K) [24,58,59]. This $\sqrt{3} \times \sqrt{3}$ surface can be prepared by deposition of over 1ML of Pb onto a Si(111) 7×7 surface at room temperature, followed by annealing the sample to 400 ~ 450 °C for 4 min. On the other hand, interestingly, it is possible to form small 2D Pb islands on the $\sqrt{3} \times \sqrt{3}$ template when the sample temperature is held at ~ 200K. As presented in Figure 6.9, the sample contains 2D Pb islands with various lateral sizes (< 500 nm) and thicknesses (< 6 ML) sitting on the $\sqrt{3} \times \sqrt{3}$ template (see the right bottom inset image of Figure 6.9). In this 2D island growth, it is important to maintain the growth temperature at ~ 200K so that it is low enough to form very thin layers below 6 ML and at the same time, it is high enough for Pb atoms to move around to form 2D islands instead of flat film structures. The effective lateral size (d_{eff}) is calculated by $d_{eff} = 2\sqrt{ab}$, where a and b are one-half of the major and minor axes of islands, respectively[7]. Thanks to its variety of 2D island sizes and thicknesses, this sample system is ideal to study the influence of low-dimensional geometries on superconductivity.

---

[7] By assuming 2D Pb island is oval shape, its area is πab. Then, one can find the radius r of circle which has the same area of πab; i.e. $\pi r^2 = \pi ab \rightarrow d_{eff} = 2r = 2\sqrt{ab}$
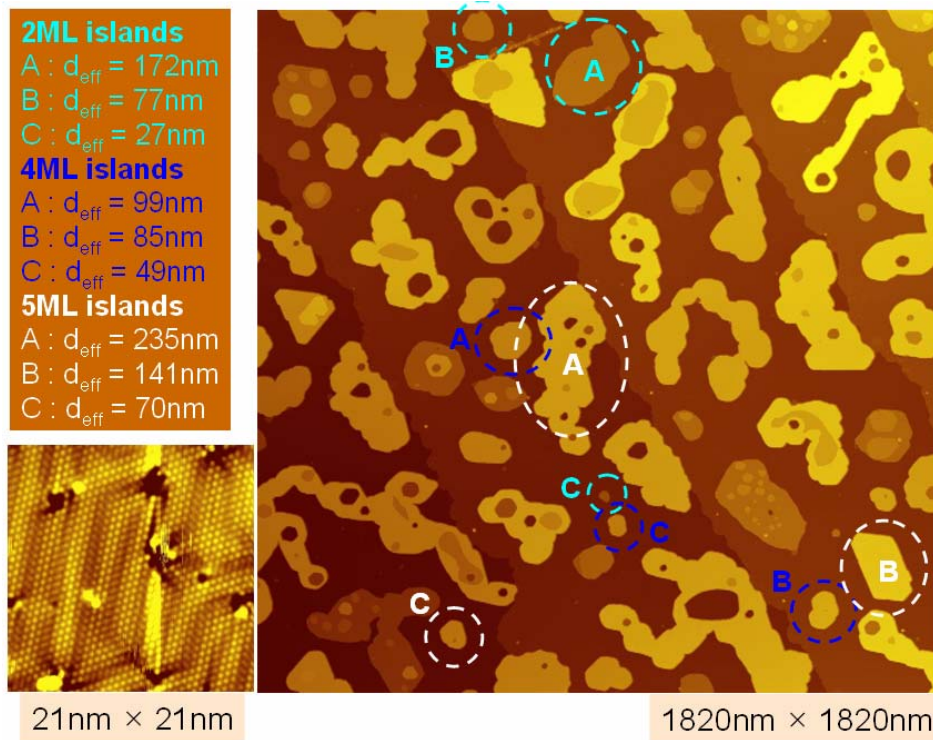
Figure 6.9: STM topography image of Pb 2D islands.

6.2.3 Two-dimensional nano-island superconductivity

The remarkable properties of a superconductor are due to its Cooper pair condensate (formed from a macroscopic number of electrons), which can be described by a single quantum wave function. According to the celebrated Bardeen-Cooper-Schrieffer (BCS) theory of superconductivity[60], there is a minimum length scale (the coherence length, ξ) on which the condensate order parameter can vary. In systems with at least one of the spatial dimensions smaller than ξ, the dimension of the orbital space occupied by the condensate is reduced. Superconductivity in reduced dimensions has stimulated interest because it is dependent on quantum confinement, interaction, and

quantum coherence effects in an intrinsically many-particle context--ingredients that drive much modern research in quantum many-body physics.

In superconductivity attention has often focused on two-dimensional (2-d) systems which can have fragile order because of quantum and thermal fluctuations. In this context, the recent discovery of *robust* superconductivity in epitaxial thin Pb films with thicknesses that are orders of magnitude smaller than ξ seems surprising[24,47,48]. Even at a thickness of only two atomic layers (~ 0.6 nm), the superconducting transition temperature (T_C ~ 5 K) of Pb films is only slightly smaller than the bulk value 7.2 K[24]. Although this observation is already interesting, much more telling information on the fate of superconductivity at small length scales emerges when the lateral dimensions of the ultra-thin films are also reduced.

By controlling the lateral size of ultrathin 2-d islands, we systematically address this regime with a detailed STM/STS study. Our experiments unveil several intriguing results. We discovered that as the lateral dimension is reduced, suppression of the superconducting order occurs. The reduction of the superconducting order parameter starts slowly, but then accelerates dramatically when the level spacing starts to approach the value of the gap. While the values of the superconducting gap of the nano-islands show thickness dependence at all lateral sizes, when normalized to the extended film limit, they collapse to a universal curve that depends only on the volume of the nano-island. Most surprisingly, our results for the size of the gap Δ versus island volume show quantitative agreement with recent STS studies of hemisphere-shaped Pb droplets, despite their dramatic difference in geometry[42,46]. The features of our system allow us to further characterize the nanoscale superconductivity and nano-islands: (i) The transition temperature dependence of large area islands depends on their thickness in

86

monolayer units. We show that an island with a higher transition temperature can induce superconductivity in a nearby island with a lower transition temperature[61].
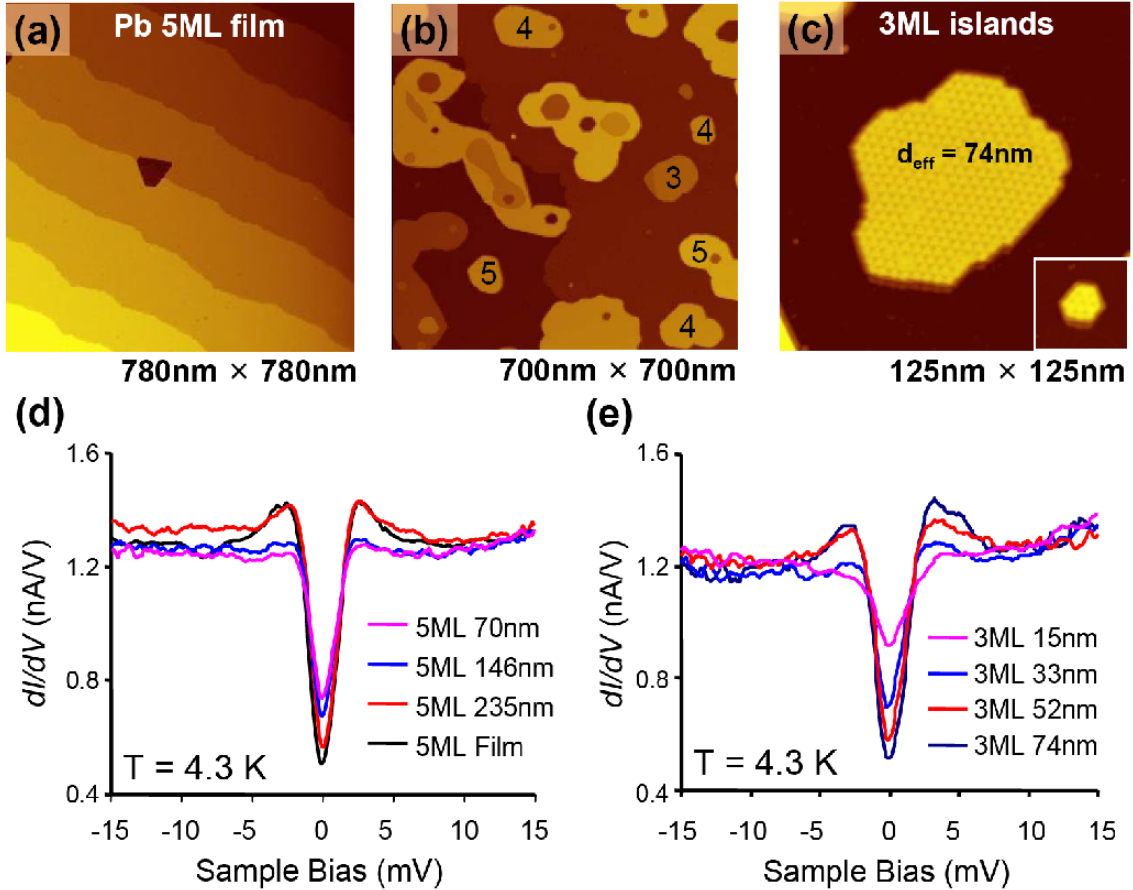
Figure 6.10: STM topography image of (a) a globally uniform 5ML Pb film and (b) 2-d Pb islands with various lateral sizes and thicknesses (sample bias $V_s = 2$ V, tunneling current $I_t = 10$ pA). The numbers labeled on the image (b) indicate thickness of islands in monolayer. (c) Two 3ML Pb islands with effective lateral size (d_{eff}) of 74 nm and 15 nm (inset) are shown in the same length scale (sample bias $V_s = 0.3$ V, tunneling current $I_t = 10$ pA). Lateral size dependence of differential conductance spectra (dI/dV) measured at 4.3 K is shown for (d) 5ML islands and (e) 3ML islands.

(ii) We experimentally determine a lateral "proximity" length of approximately 40 nm, roughly 50% of the bulk coherence length. (iii) We extract a value of the size-dependent nano-island *normal-state conductivity* from the STS spectra, and thus provide

87

a measure of the normal-state electron scattering rate in this system[62-64]. Since Pb is a BCS superconductor, this additional information will help constrain future detailed theoretical work on these systems.

Through control of kinetic processes one can either grow a thin film of uniform thickness or 2-d islands of various thicknesses and areas; for example Fig. 6.10(a) shows a 5 monolayer (ML) film grown on the Pb-on-Si (111) $\sqrt{3} \times \sqrt{7}$ surface[24] while Fig. 6.10(b) shows 2-d islands of different sizes and shape on the same substrate. Some 2-d islands are isolated while some islands contain mixed regions of different thicknesses. Also shown in Fig. 6.10(c) is a close-up view of two 3ML 2-d islands, one with an effective diameter (d_{eff}) of 74 nm and one with an effective diameter of 15 nm. The effective diameter (d_{eff}) of each island is calculated by using $d_{eff} = \sqrt{ab}$, where a and b are lengths along the major and minor axes, respectively.

Fig. 6.10(d) shows *dI/dV* tunneling spectra acquired at 4.3 K for a 5ML film and 5ML 2-d islands of various effective diameters. Interestingly, even at a diameter of 235 nm, which is much larger than the bulk coherence length (~ 80 nm), one already observes a small reduction of the superconducting gap in comparison to that of the extended film. As one can observe directly from the data the trend toward gap reduction continues as the diameter of the 2-d islands decreases further. Fig. 6.10(e) shows *dI/dV* tunneling spectra acquired at 4.3 K for 3ML 2-d islands with diameters ranging from 15 nm to 74 nm. The size dependence of the superconducting gap of 4ML 2-d islands follows a similar trend to that of 3ML islands. From *dI/dV* features at biases above Δ one can extract a measure of the *normal state* island conductivity.
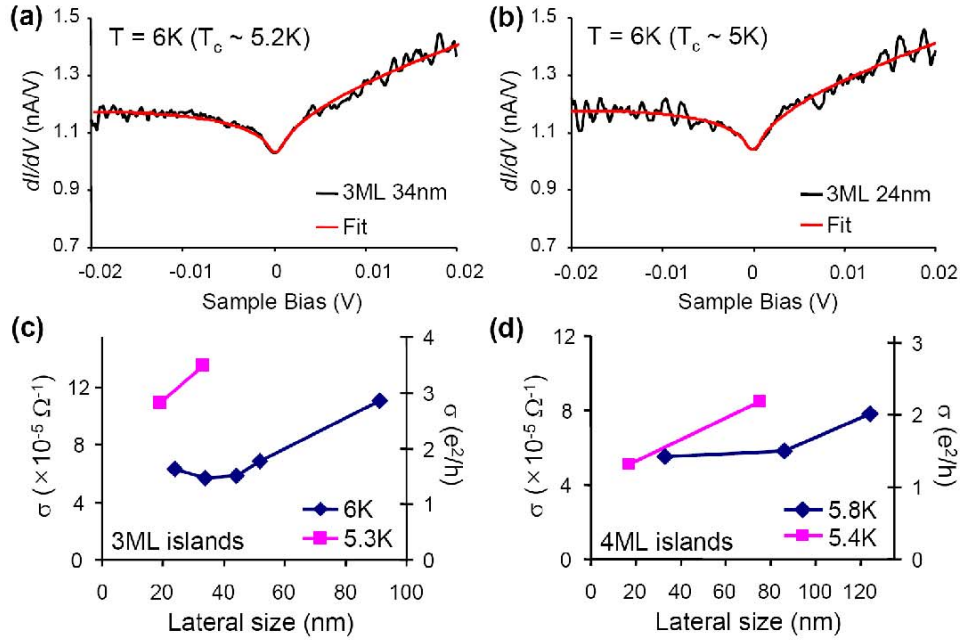
(e) 3ML island fitting result

T (K)	d_{eff} (nm)	c1	c2	α	m	$1/\alpha$	σ (1/Ω)	σ (e²/h)	τ (sec)	$l = \tau V_f$ (nm)
6K	91	0.85	0.94	0.19	5.44	5.15	1.11E-04	2.84	1.13E-16	0.18
6K	52	0.98	1.17	0.32	5.36	3.17	6.82E-05	1.75	6.93E-17	0.11
6K	44	0.96	1.41	0.37	6.35	2.71	5.83E-05	1.49	5.93E-17	0.09
6K	34	0.97	1.42	0.38	5.86	2.66	5.72E-05	1.47	5.81E-17	0.09
6K	24	0.96	1.27	0.34	5.89	2.92	6.28E-05	1.61	6.38E-17	0.10
5.3K	33	0.71	1.07	0.16	5.74	6.27	1.35E-04	3.46	1.37E-16	0.22
5.3K	19	0.80	1.13	0.20	5.45	5.08	1.09E-04	2.80	1.11E-16	0.18

(f) 4ML island fitting result

T (K)	d_{eff} (nm)	c1	c2	α	m	$1/\alpha$	σ (1/Ω)	σ (e²/h)	τ (sec)	$l = \tau V_f$ (nm)
5.8K	124	0.89	1.50	0.28	-3.22	3.63	7.82E-05	2.00	7.95E-17	0.13
5.8K	86	1.02	1.69	0.37	-4.76	2.71	5.83E-05	1.50	5.93E-17	0.09
5.8K	33	0.98	2.12	0.39	-4.30	2.57	5.52E-05	1.42	5.61E-17	0.09
5.4K	75	0.95	1.22	0.25	-1.24	3.95	8.49E-05	2.18	8.63E-17	0.14
5.4K	17	1.01	1.94	0.42	-0.62	2.36	5.07E-05	1.30	5.16E-17	0.08

Figure 6.11: (a,b) Comparison of *dI/dV* spectrum measured at 6 K (above T_C) for 3ML islands and theoretical tunneling density of states based on electron-electron interaction and disorder (Eq. (1)). Since T = 0 K is assumed in equation (1), 1.2 meV broadening effect is applied to the fitting curves to take finite temperature and instrument noise into account. (c,d) 2-d conductivity (σ) values for Pb islands obtained from the fitting result in (a,b). (e,f) Table of all parameters and physical quantities extracted from the fitting including 2-d conductivity σ, electron relaxation time τ, and the relaxation length l.

The majority of this paper is focused on the superconducting properties of nano-islands of different thicknesses and shapes. However, our data also show interesting features at voltage biases above the gap when the temperature is below T_C, and for all voltages we probed when the temperature is above T_C.

As seen in Fig. 6.11 (a) and (b) (where the temperature is above T_C), there is a "pseudo-gap" feature that appears (even for very large islands). The pseudo-gap does not measurably change when the temperature drops below T_C suggesting that it is likely an intrinsic property of the normal state of the Pb islands and not related to superconductivity in any way. It has been suggested in an earlier study[53] on films that such features may be due to phonon effects. We show here that we obtain a very good fit to a theory based on a pseudo-gap feature arising only from the combined influences of electron-electron interactions and disorder[62]. Moreover, we are able to extract a quantitative estimate of the *normal state* conductivity of the Pb nano-islands used in our experiments.

According to Ref 62, the tunneling density of states should follow a form

$$\frac{dI}{dV} = c_1 + c_2|V|^\alpha + mV$$

(6.31)

where c_1, c_2, α and m all depend on details of the system, and V is the voltage. The final term mV accounts for a weakly energy-dependent tunneling matrix element between the STM tip and the Pb substrate rather than intrinsic island properties and does not enter our estimates of island conductivity. For our purposes, we are most interested in α as it is inversely proportional to the 2-d conductance of the nano-island/thin film substrate:

$$\alpha = \frac{e^2}{h\sigma} \frac{\ln(2\pi a e^2 dn/d\mu)}{2\pi}$$

(6.32)

90

where e is the charge of the electron, h is Planck's constant, σ is the 2-d conductivity of the island or film, a is the tip-sample spacing, and $dn/d\mu$ is the compressibility of the island or film. (Here n is the 2-d density and μ the chemical potential.) Since the expression is only logarithmically dependent on the compressibility, we can estimate it by using a free electron approximation. For 2-d electrons, $dn/d\mu = 4\pi m^*/h^2$, where m* $=1.14\ m_e$ is the effective mass of Pb and m_e is the bare mass of the electron[65].

Temperature dependent fits of the conductance are given in Fig. 6.11(e,f) for 3 ML and 4 ML film thicknesses, just below example fits and plots of conductance vs island size in Fig 6.11(c,d). The values are consistent with those measured in early film samples[63,64], *but here we provide the first conductance measurements of islands*. The general trend is for thicker and larger islands to be more conducting, and for the conductance to be higher as the temperature is lowered. These findings are all consistent with expectations.

From the conductance, one can also estimate the electron relaxation time τ and the relaxation length $l=\tau V_F$ from

$$\sigma = \frac{ne^2\tau}{m^*}$$

(6.33)

From the atomic-scale relaxation lengths inferred from the conductance and given in the table, one can conclude that there is appreciable interface scattering. We believe the lateral size dependence of the scattering likely originates in a density of states effect on the scattering states. Fig. 6.12 shows that the pseudo-gap feature at energies above the gap does not change as the temperature drops below the superconducting transition temperature.
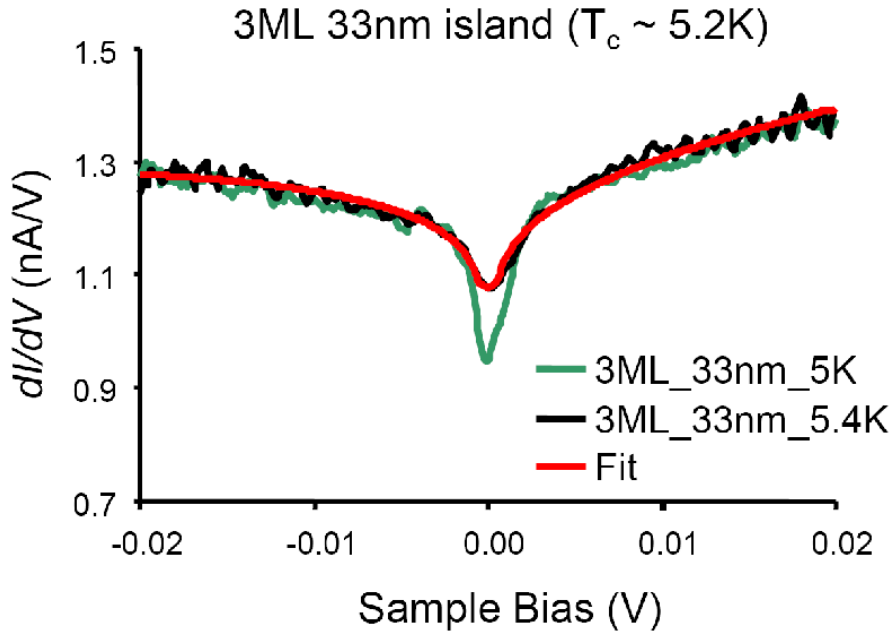
Figure 6.12: Shown is a comparison of the pseudo-gap feature at temperatures below and above the superconducting transition temperature. The lack of any clear temperature dependence for energies above the gap (clear from fit to Eq.(1)) indicates the high-energy part of the pseudo-gap is not related to superconductivity, but is rather a normal state property of the Pb nano-islands.

In order to more quantitatively characterize the suppression of superconductivity, we measured the transition temperature, T_C, for different lateral sizes and thicknesses of 2-d islands.   Figs. 6.13(a,b) shows dI/dV spectra fitted with the BCS tunneling density of states at finite temperature to obtain a temperature-dependent superconducting gap $\Delta(T)$, which allows us to determine T_C.   Fig. 6.13(c) demonstrates that T_C of 3ML, 4ML, and 5ML islands depends on their lateral size d_{eff}.   Interestingly, there is a transition region (somewhere between 40 to 60 nm) below which electrons rapidly lose the strength of superconducting coherence.

92
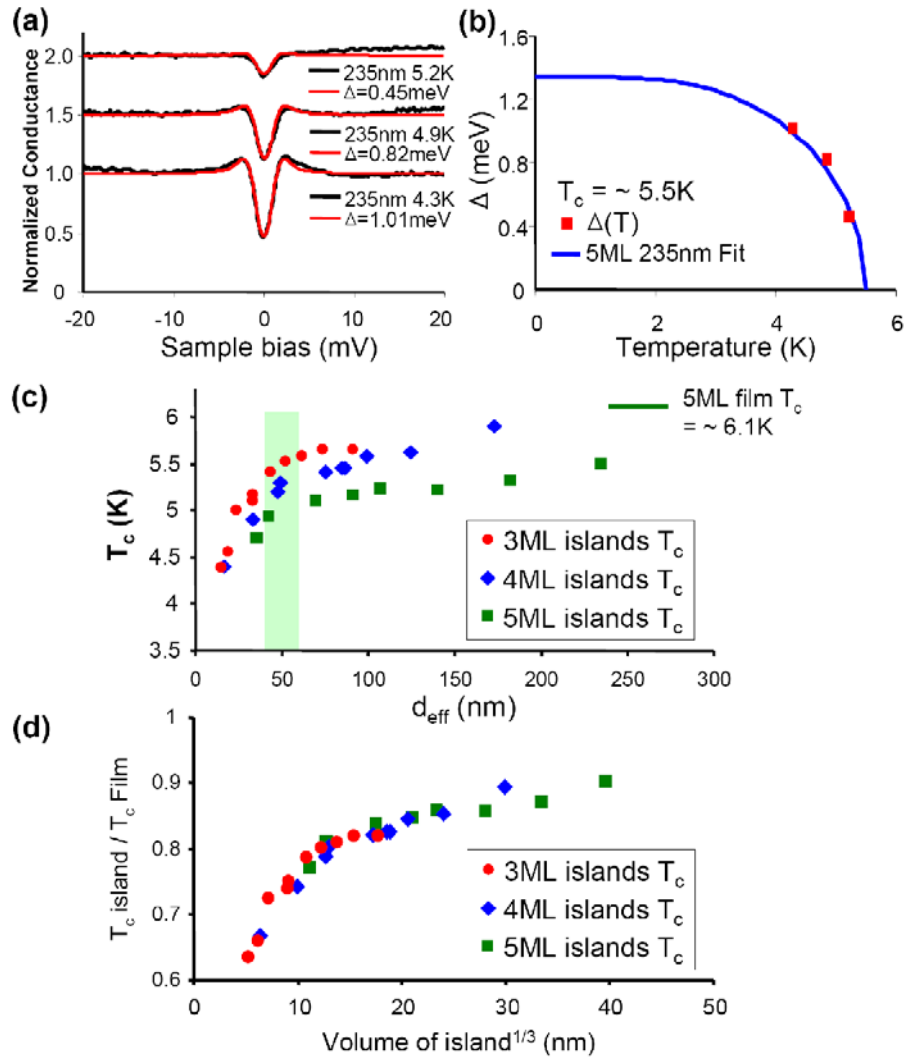
Figure 6.13: (a) Normalized conductance spectra (black) measured as a function of temperature from a 5ML Pb island with a 235nm lateral size were fitted using the BCS density of states for the tunneling conductance (red). Each normalized spectrum is offset successively by 0.5 for clarity.   (b) The superconducting energy gaps (Δ) for each temperature were obtained from (a) and plotted as red squares. The blue curve is a fitting of these energy gap data using a BCS gap equation to obtain a T_C of ~ 5.5 ± 0.1 K for a 5ML island with 235 nm lateral size.   All T_C values determined from such fitting are estimated to have an error bar of ± 0.1 K.   (c) T_C as a function of island lateral size for 3ML, 4ML, and 5ML islands.   A transition region from slow to dramatic reduction of superconductivity is shaded in green.   (d) T_C of islands was normalized to the globally flat film T_C for each thickness and plotted as a function of cube root of island volume.   For the T_C normalization, 5ML film T_C was measured to be 6.1 K, and estimated values of 6.9 K and 6.3 K from the T_C trend in (c) were used for 3ML and 4ML film, respectively.

We also observe a variation of T_C as a function of island thickness for a given d_{eff} : T_C (3ML) > T_C (4ML) > T_C (5ML), due to the quantum oscillations of T_C from the vertical electronic confinement, a topic that has been intensively investigated recently[24,56] (3ML data was previously unavailable due to difficulty in preparing 3ML films). The transition region from slow to rapid T_C reduction also shows thickness dependence: it occurs at ~ 40 nm for 5ML islands, at ~ 50 nm for 4ML islands, and slightly above 50 nm for 3ML islands. On the other hand, if we normalize the T_C of 2-d islands to the thin film value at a given thickness and plot it as a function of island volume, the data collapse onto a single curve, revealing a universal behavior of superconductivity suppression with respect to the island volume (Fig. 6.13(d)). Remarkably, this universal curve is in quantitative agreement with earlier STS studies for Pb droplets, despite the dramatic difference in geometry[42,46]. This collapse demonstrates that superconductivity in regularly-shaped nano-islands is sensitive to a large degree only to the average level spacing of a nano-structure, affirming to a surprisingly degree theories[44,45,66] of finite-size superconductivity suppression in which the mean number of electronic orbitals within the pairing energy window plays the central role.

Superconductivity is suppressed in a small island as the value of the level spacing approaches the value of the bulk superconducting gap[44,45,66]. This result follows directly from the BCS mean-field gap equation:

$$\frac{1}{V} = \sum_{n}^{\varepsilon_n = E_D} \frac{1}{\sqrt{\Delta^2 + \varepsilon_n^2}} \tag{6.34}$$

where V is the electron-phonon coupling, ε_n are the single-particle energy levels on the island, E_D is the Debye (phonon) energy, and Δ is the superconducting gap. The typical scale of the variation in the density of states (number of energy levels on the grain per

94

unit energy) is set by the energy scale of the electronic degrees of freedom, E_F (Fermi energy), which is typically 1-10 electron volts (9.5 eV for Pb). On the other hand, E_D is typically tens or hundreds of Kelvin (88 K in Pb), or roughly 10^{-2} electron volts. Because $E_D << E_F$, the density of states will be constant to a good approximation over the energy range of the sum in (6.34). When mesoscopic fluctuations in level separations are neglected $\varepsilon_n = \delta\, n$, where δ is the level spacing. The corresponding density of states for such an island is $1/\delta$.

From the well-known formula for the bulk gap, $\Delta_0 = 2\, E_D \exp\{-1/\lambda\} = 2\, E_D \exp\{-\delta/V\}$, and the bulk value of the transition temperature, $T_C = \Delta_0/1.77 = 7.2$ K, we find $\delta/V = 2.65$ for Pb under the equal level spacing assumption $\varepsilon_n = \delta\, n$. Thus, for the critical island size where the gap $\Delta = 0$, we have

$$2.65 = \frac{\delta}{V} = \sum_{n=1}^{n_{max,0} = E_D/\delta} \frac{1}{n} \tag{6.35}$$

which implies that $7 < n_{max,0} < 8$ when the island becomes so small that the transition temperature vanishes, or that $\delta = E_D/8 \sim 11$ K is roughly equal to the bulk gap, $\Delta_0 = 12$ K. The key feature of Eq.(6.35) is the "1/n" contribution from the different energy levels: Even for "large" n, there are appreciable contributions to the sum (1/n is logarithmically divergent). This means that any random (not too large) fluctuations from the equal-level spacing approximation due to an irregular shaped island will be effectively averaged out. Moreover, in islands larger than the critical size (with smaller level spacing δ) there will be *even more effective averaging* because the larger small n contributions will carry less weight due to the presence of the gap in the denominator of Eq.(6.34) and Eq.(6.36), and there will be more terms in the sum to be averaged, $n_{max} > n_{max,0}$:

$$2.65 = \frac{\delta}{V} = \sum_{n=1}^{n_{max}=E_D/\delta} \frac{1}{\sqrt{\left(\frac{\Delta}{\delta}\right)^2 + n^2}} \qquad (6.36)$$

From Eq.(6.36), the gap dependence on level spacing, $\Delta(\delta)$, is determined. Similar considerations apply to the level spacing dependence of the critical temperature which is proportional to the gap. For islands of equal volume, but different shape, the value of n_{max} in Eq.(6.36) will be roughly the same, since that only counts the total number of states in the energy window within E_D of the Fermi energy, and that is expected to be a weak function of island shape.

We believe the effective averaging of level spacing fluctuations due to a roughly constant density of states over the relevant energy range, E_D, is the reason we find that the normalized critical temperature curves in Fig. 6.13(d) collapse to a universal form that is to a good approximation independent of island shape.

6.2.4 The lateral proximity effect

An intriguing lateral proximity effect is observed in the local STS of an island containing regions of different heights and different superconducting strength. In our samples, one often finds 2ML islands with a local 3ML region, forming a *lateral heterojunction*, as shown in the inset of Fig. 6.14(b). Fig. 6.14(a) shows an enlarged STM image of the square area marked in the inset of 6.14(b). *dI/dV* spectra taken on the marked locations (A-D in 6.14(a)) are also shown in 6.14(b). As expected, the superconducting gap is deeper in the 3ML region (position A) compared to that in 2ML region (D)[3,18]. However, near the interface, one observes gap suppression (position B) in the 3ML island and gap enhancement (position C) for the 2ML island.
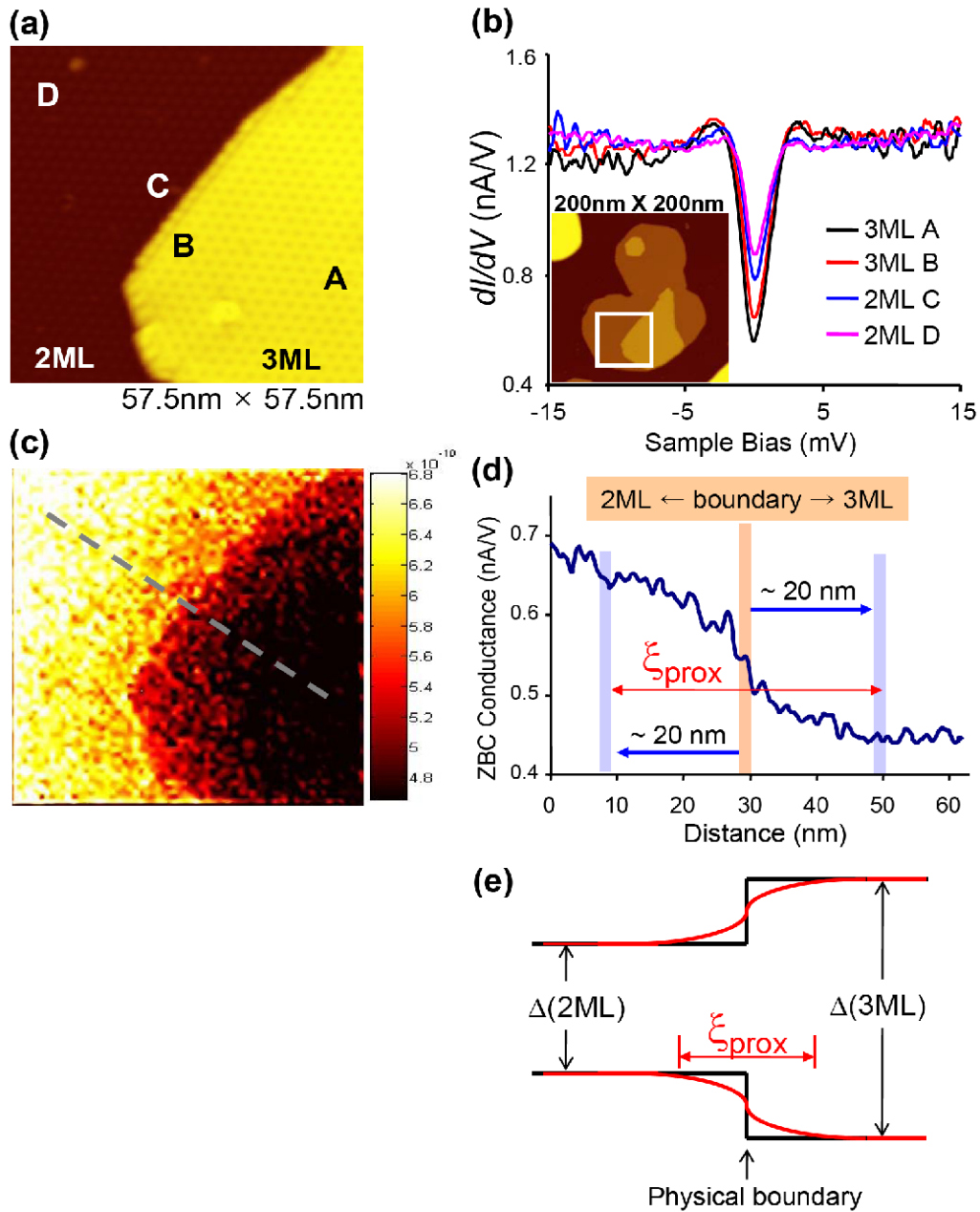
Figure 6.14: (a) Zoom-in STM topography image for the square area of inset in (b), which shows neighboring 2ML and 3ML areas (sample bias $V_s = 0.3$ V, tunneling current $I_t = 10$ pA). (b) Differential conductance spectra at 4.3 K measured from different locations labeled in (a). (c) ZBC image measured at 4.3 K for the same area of (a). The color contrast reflects the variation of local superconductivity. (d) Line profile of the dashed line in (c) which shows the variation of superconducting order across the physical boundary. (e) A schematic of how Cooper-pair "gap bending" occurs across the heterojunction of neighboring Pb islands.

Also shown in Fig. 6.14(c) is the spatial mapping of the local superconducting gap, as reflected by the value of the zero bias conductance (ZBC), of the same area as 6.14(a). In this image, a darker color implies a deeper superconducting gap. Here the boundary in the ZBC image precisely matches with the topographic boundary between the two thicknesses. Moreover, from the color contrast in the image, a gradual but evident change of local superconductivity is observed on both sides of the boundary. This must be due to a lateral proximity effect caused by the tunneling of Cooper pairs with different binding energies across the boundary. Fig. 6.14(d) shows the ZBC profile along the line marked in 6.14(c). One can see that there is a proximity length of roughly 20 nm from the physical boundary (on either side) before the superconducting gap recovers to the respective values for 2ML/3ML islands, corresponding to a proximity length, $\xi_{prox} \approx 40$-50 nm, for such a superconductor "heterojunction". A schematic of Cooper-pair "gap bending" across the heterojunction is seen in Fig. 6.14(e).

With this relatively simple heterojunction picture in mind, we can then understand the spatial imaging of the superconducting gap, $\Delta(x,y)$, in the more complicated heterostructures shown in Fig. 6.15 (a-f). For example, in Fig. 6.15(a) where two 3ML islands are separated by a narrow strip of 2ML region (marked by an arrow), one observes significant enhancement of Δ in the narrow 2ML strip (Fig. 6.15(b)). A similar situation is also seen in Fig. 6.15(e,f) with a slightly wider 2ML strip. Moreover, for a 3ML nano-island with $d_{eff} < \xi_{prox}$, one observes rather uniform Δ within the island, indicating the rigidity of the order parameter on the scale ξ_{prox} (Fig. 6.15(c,d)).
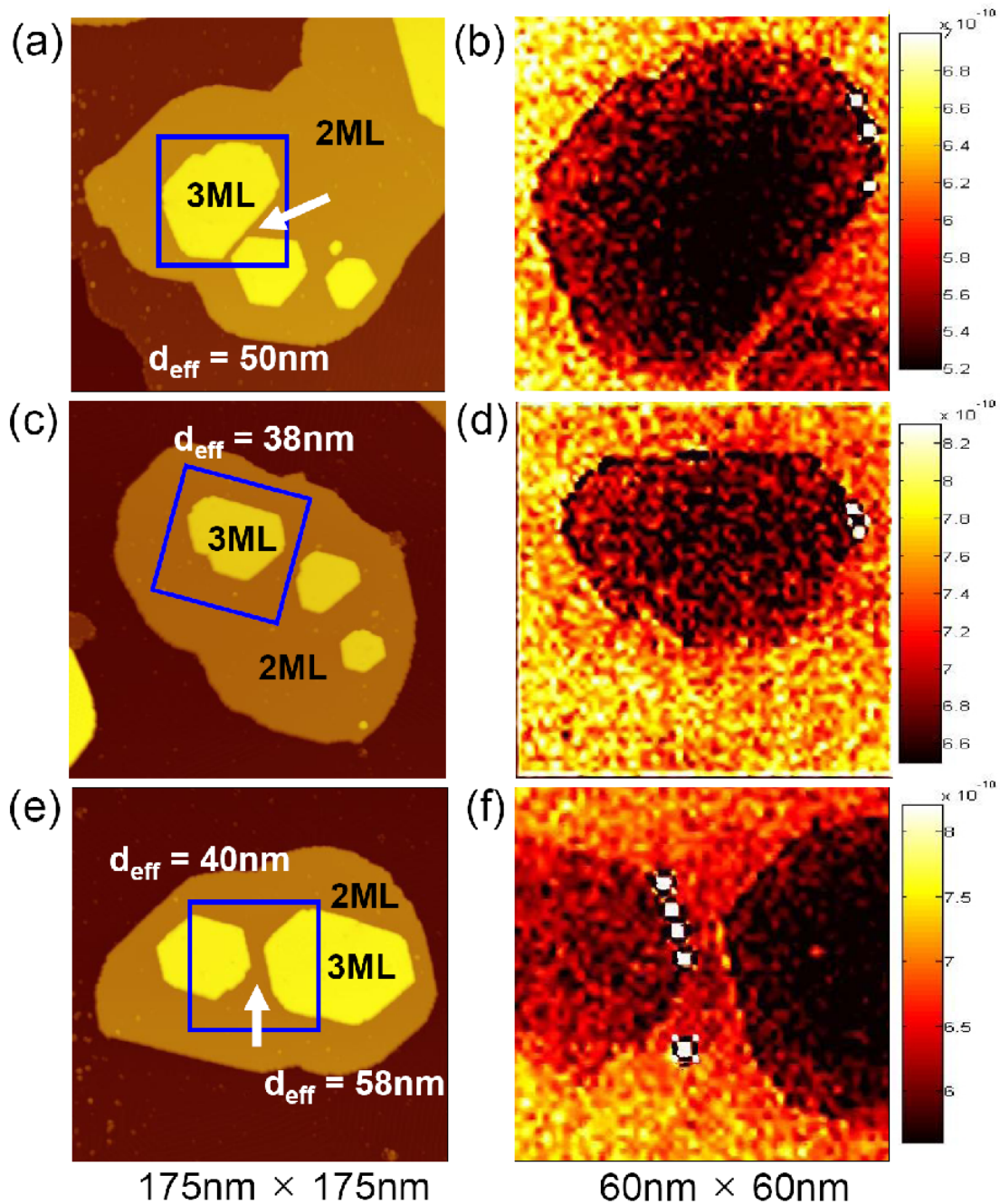
98

Figure 6.15: (a), (c), and (e) are topography images of 2-d islands which have a 3ML area on top of a 2ML island. (b), (d), and (f) are zero bias conductance (ZBC) images measured at 4.3 K for the square area marked on (a), (c), and (e), respectively. The arrow marked on (a) and (e) indicates a narrow strip of 2ML area sandwiched by nearby 3ML islands.

99

As shown in Fig. 6.14 and 6.15, superconductivity gap differences between islands of different thicknesses[24,48] result in intriguing proximity effects. Interestingly, *even within an island of the same thickness,* similar proximity effects are induced in regions with a large aspect ratio, that is, that are narrow and long. Fig. 6.16(a) shows a "finger shaped" island of 9ML Pb which is connected to a much larger film region. To illustrate the spatial variation of the superconducting property along the finger island, we plotted the 2-d mapping of the second derivative of the current voltage (*I-V*) curve near the steepest slope of the gap-opening regions (see Fig. 6.16(b,c))[24]. Clearly, from the contrast change along the island in Fig. 6.16(b,c), the strength of local superconductivity slowly decays as one approaches the tip of the finger region. The narrow region near the tip of the finger supports less robust superconductivity due to lateral confinement (it acts locally like a smaller island), while the "base" of the finger has an enhanced gap due to proximity to the larger film region.
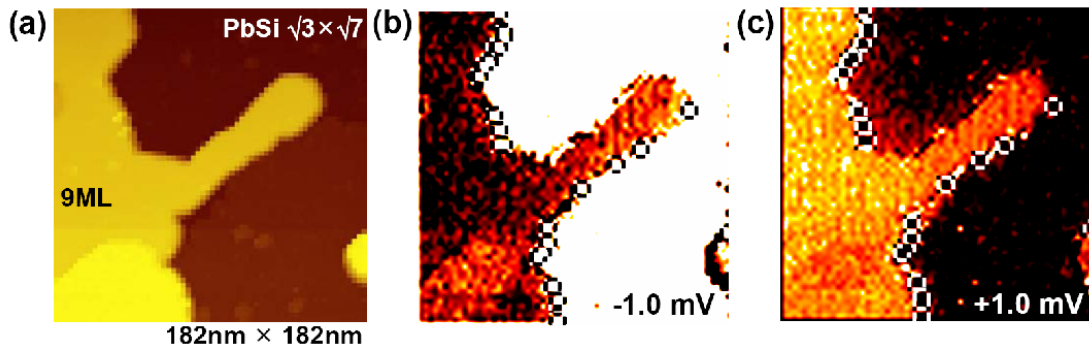
Figure 6.16: (a) An STM topography image showing a Pb 9ML "finger shaped" island connected to a large film. (b,c) d^2I/dV^2 mapping at 4.3 K for sample biases of -1 and +1 mV, respectively. The color contrast directly reveals spatial variation of the superconducting gap.

6.2.5 Summary

We have shown that as the lateral dimension of Pb 2D islands is reduced, the strength of the superconducting order parameter is also reduced, at first slowly for dimensions larger than the bulk coherence length, and then dramatically at a critical length scale of ~ 40nm.   We have performed a STM/STS study of 2-d superconducting islands and their heterojunctions that reveals detailed information about the characteristic length and energy scales that apply to superconductivity at the nanoscale.   We expect this work to have implications for superconducting device implementation and to stimulate further studies.

Bibliography

1.   Binnig, G. and Rohrer, H. SCANNING TUNNELING MICROSCOPY. *Ibm Journal of Research and Development* 30, 355-369 (1986).

2.   Chen, C. J., *Introduction to Scanning Tunneling Microscopy*. (Oxford University Press, 1993).

3.   Bardeen, J. Tunneling from a many particle point of view. *Phys Rev Lett* 6, 57-59 (1961).

4.   Pan, S. H., Hudson, E. W., and Davis, J. C. He-3 refrigerator based very low temperature scanning tunneling microscope. *Review of Scientific Instruments* 70, 1459-1463 (1999).

5.   Pan, S. H.,   Patent No. WO 93/19494 (30 September 1993).

6.   Smith, A. R., Chao, K. J., Niu, Q., and Shih, C. K. Formation of atomically flat silver films on GaAs with a "silver mean" quasi periodicity. *Science* 273, 226-228 (1996).

7.   Gundlach, K. H. ZUR BERECHNUNG DES TUNNELSTROMS DURCH EINE TRAPEZFORMIGE POTENTIALSTUFE. *Solid-State Electronics* 9, 949 (1966).

8.   Pascual, J. I. et al. Role of the electric field in surface electron dynamics above the vacuum level. *Physical Review B* 75,   (2007).

9.   Wahl, P. et al. Quantum coherence of image-potential states. *Physical Review Letters* 91,   (2003).

10.   Wiesendanger, R., *Scanning Probe Microscopy and Spectroscopy*. (Cambridge University Press, 1994).

11.   Liu, H. et al. Confinement effect on scattering states in a thin lead film: Field-induced resonance states in the high-bias regime of scanning tunneling microscopy. *Physical Review B* 76,   (2007).

12.   Liu, X. et al. Wavevector-dependent quantum-size effect in electron decay length at Pb thin film surfaces. *Appl Phys Lett* 93, 093105 (2008).

13.   Ma, X. C. et al. Experimental observation of quantum oscillation of surface chemical reactivities. *Proc Natl Acad Sci USA* 104, 9204-9208 (2007).

14.   Miller, T., Chou, M. Y., and Chiang, T. C. Phase Relations Associated with One-Dimensional Shell Effects in Thin Metal Films. *Phys Rev Lett* 102, 236803 (2009).

15.   Paggel, J. J. et al. Atomic-layer-resolved quantum oscillations in the work function: Theory and experiment for Ag/Fe(100). *Phys Rev B* 66, 233403 (2002).

16.   Qi, Y. et al. Atomic-layer-resolved local work functions of Pb thin films and their dependence on quantum well states. *Appl Phys Lett* 90, 013109 (2007).

17.   Schulte, F. K. Theory of Thin Metal-Films - Electron-density, Potentials and Work Function. *Surface Science* 55, 427-444 (1976).

18.   Wei, C. M. and Chou, M. Y. Theory of quantum size effects in thin Pb(111) films. *Phys Rev B* 66, 233408 (2002).

19.   Czoschke, P., Hong, H. W., Basile, L., and Chiang, T. C. Quantum beating patterns observed in the energetics of Pb film nanostructures. *Phys Rev Lett* 93, 036103 (2004).

20.   Eom, D., Qin, S., Chou, M. Y., and Shih, C. K. Persistent superconductivity in ultrathin Pb films: A scanning tunneling spectroscopy study. *Phys Rev Lett* 96, 027005 (2006).

21.   Jia, Y., Wu, B., Weitering, H. H., and Zhang, Z. Y. Quantum size effects in Pb films from first principles: The role of the substrate. *Phys Rev B* 74, 035433 (2006).

22.   Ozer, M. M. et al. Tuning the quantum stability and superconductivity of ultrathin metal alloys. *Science* 316, 1594-1597 (2007).

23.   Ozer, M. M., Thompson, J. R., and Weitering, H. H. Hard superconductivity of a soft metal in the quantum regime. *Nat Phys* 2, 173-176 (2006).

24.   Qin, S. Y., Kim, J., Niu, Q., and Shih, C. K. Superconductivity at the Two-Dimensional Limit. *Science* 324, 1314-1317 (2009).

25.   Yeh, V. et al. Role of the metal/semiconductor interface in quantum size effects: Pb/Si(111). *Phys Rev Lett* 85, 5158-5161 (2000).

26.   Zhang, Z. Y., Niu, Q., and Shih, C. K. "Electronic growth" of metallic overlayers on semiconductor substrates. *Phys Rev Lett* 80, 5381-5384 (1998).

27. Chang, S. H. et al. Electronic growth of Pb islands on Si(111) at low temperature. *Phys Rev B* 66, 245401 (2002).

28. Hupalo, M. et al. Atomic models, domain-wall arrangement, and electronic structure of the dense Pb/Si(111)-root 3x root 3 phase. *Phys Rev B* 66, 161410 (2002).

29. Luh, D. A. et al. Quantum electronic stability of atomically uniform films. *Science* 292, 1131-1133 (2001).

30. Su, W. B. et al. Correlation between quantized electronic states and oscillatory thickness relaxations of 2D Pb islands on Si(111)-(7 x 7) surfaces. *Phys Rev Lett* 86, 5116-5119 (2001).

31. Stroscio, J. A., Feenstra, R. M., and Fein, A. P. Electronic-structure of the Si(111)2X1 Surface by Scanning-tunneling Microscopy. *Phys Rev Lett* 57, 2579-2582 (1986).

32. Onnes, H. K. The resistance of pure mercury at helium temperatures. *Commun Phys Lab Univ Leiden* 12, 120 (1911).

33. Bardeen, J., Cooper, L. N., and Schrieffer, J. R. Theory of Superconductivity. *Phys Rev* 108, 1175-1205 (1957).

34. Cooper, L. N. *Phys Rev* 104, 1189 (1956).

35. Pines, D. *Phys Rev* 109, 280 (1958).

36. Frohlich, H. *Phys Rev* 79, 845 (1950).

37.   Tinkham, M., *Introduction to superconductivity*. (Dover Publications, 1996).

38.   Bogoliubov, N. N. *Nuovo Cimento* 7, 794 (1958).

39.   Valatin, J. G. *Nuovo Cimento* 7, 843 (1958).

40.   Ralph, D. C., Black, C. T., and Tinkham, M. Spectroscopic measurements of discrete electronic states in single metal particles. *Phys. Rev. Lett.* 74, 3241-3244 (1995).

41.   Zhang, T. et al. Superconductivity in one-atomic-layer metal films grown on Si(111). *Nat. Phys.* 6, 39-43 (2010).

42.   Bose, S. et al. Observation of shell effects in superconducting nanoparticles of Sn. *Nat. Mater.* 9, 550-554 (2010).

43.   Clark, K. et al. Superconductivity in just four pairs of (BETS)(2) GaCl4 molecules. *Nat. Nanotechnol.* 5, 261-265 (2010).

44.   Smith, R. A. and Ambegaokar, V. Effect of level statistics on superconductivity in ultrasmall metallic grains. *Phys. Rev. Lett.* 77, 4962-4965 (1996).

45.   vonDelft, J., Zaikin, A. D., Golubev, D. S., and Tichy, W. Parity-affected superconductivity in ultrasmall metallic grains. *Phys. Rev. Lett.* 77, 3189-3192 (1996).

46.   Brihuega, I. et al. Quantum and critical fluctuations in the superconductivity of single, isolated Pb nanoparticles. *Preprint at http://arxiv.org/0904.0354v1* (2009).

47.   Ozer, M. M., Thompson, J. R., and Weitering, H. H. Hard superconductivity of a soft metal in the quantum regime. *Nat. Phys.* 2, 173-176 (2006).

48.   Eom, D., Qin, S., Chou, M. Y., and Shih, C. K. Persistent superconductivity in ultrathin Pb films: A scanning tunneling spectroscopy study. *Phys. Rev. Lett.* 96, 027005 (2006).

49.   Dolan, G. J. and Silcox, J. Critical thicknesses in superconducting thin-films. *Phys. Rev. Lett.* 30, 603-606 (1973).

50.   Dynes, R. C., White, A. E., Graybeal, J. M., and Garno, J. P. Breakdown of Eliashberg theory for two-dimensional superconductivity in the presence of disorder. *Phys. Rev. Lett.* 57, 2195-2198 (1986).

51.   Guan, Z. L. et al. Sample-size dependence of the superconducting transition of ribbon-shaped Pb nanocrystals studied by scanning tunneling spectroscopy. *Phys. Rev. B* 81,   (2010).

52.   Brun, C. et al. Reduction of the superconducting gap of ultrathin Pb islands grown on Si(111). *Phys. Rev. Lett.* 102,   (2009).

53.   Wang, K. et al. Pseudogap mediated by quantum-size effects in lead islands. *Phys. Rev. Lett.* 102, 076801 (2009).

54.   Guo, Y. et al. Superconductivity modulated by quantum size effects. *Science* 306, 1915-1917 (2004).

55. Hetel, I., Lemberger, T. R., and Randeria, M. Quantum critical behaviour in the superfluid density of strongly underdoped ultrathin copper oxide films. *Nat. Phys.* 3, 700-702 (2007).

56. Noffsinger, J. and Cohen, M. L. First-principles calculation of the electron-phonon coupling in ultrathin Pb superconductors: Suppression of the transition temperature by surface phonons. *Phys. Rev. B* 81, 214519 (2010).

57. Yazdani, A. and Kapitulnik, A. Superconducting-insulating transition in two-dimensional a-MoGe thin films. *Phys. Rev. Lett.* 74, 3037 (1995).

58. Lu, S. M. et al. Strength modulation of quantum-well states in Pb islands with periodic distortions on Si(111). *Phys Rev B* 75, 113402 (2007).

59. Schmidt, T. and Bauer, E. Interfactant-mediated quasi-Frank van der Merwe growth of Pb on Si(111). *Phys Rev B* 62, 15815 (2000).

60. Bardeen, J., Cooper, L. N., and Schrieffer, J. R. Theory of Superconductivity. *Phys. Rev.* 108, 1175 (1957).

61. Parker, C. V. et al. Nanoscale proximity effect in the high-temperature superconductor Bi2Sr2CaCu2O8+delta using a scanning tunneling microscope. *Phys. Rev. Lett.* 104,   (2010).

62. Levitov, L. S. and Shytov, A. V. Coulomb blocking of tunneling: from zero-bias anomaly to coulomb gap. *arXiv:cond-mat\9607136v1* (1996).

63. Pfennigstorf, O., Lang, K., Gunter, H. L., and Henzler, M. Electronic transport in ultrathin epitaxial Pb films on Si(111) surfaces. *Appl. Surf. Sci.* 162, 537-546 (2000).

64. Pfennigstorf, O., Petkova, A., Kallassy, Z., and Henzler, M. Conductivity of ultrathin Pb films during growth on Si(111) at low temperatures. *Eur. Phys. J. B* 30, 111-115 (2002).

65. Hinch, B. J., Koziol, C., Toennies, J. P., and Zhang, G. Evidence for quantum size effects observed by Helium atom scattering during the growth of Pb on Cu(111). *Europhys. Lett.* 10, 341-346 (1989).

66. Anderson, P. W. Theory of dirty superconductors. *J. Phys. Chem. Solids* 11, 26-30 (1959).

Vita

Jungdae Kim was born in Jinhae-si, South Korea on August 16, 1975. He entered Pusan National University in South Korea in 1994. After receiving the degree of Bachelor of Science from Pusan National University in 2001, he entered the graduate school of Seoul National University in South Korea and received the degree of Master of Science in 2003. In September 2004 he started the graduate school program in The University of Texas at Austin.

Permanent address: 2501 Lake Austin Blvd C206, Austin, TX 78703

This dissertation was typed by the author.